Editorial letter:

On the Aims & Scopes of ***Radiation Physics and Engineering***

Radiation Physics and Engineering (RPE) is an international scientific-research journal published biannual by K. N. Toosi University of Technology jointly with Nuclear Society of Iran (NSI).

The purposes of the journal are to provide a high quality medium for the publication of substantial, original and scientific papers on the development and the enhancement of radiation physics and radiation engineering researches at the national as well as international level. In addition, we hope to facilitate communication among physicists, to publish the results of research, develop collaboration between research workers from different research centers and universities and introduce young researchers.

Papers dealing with nuclear radiation and radionuclide techniques, nuclear techniques and radiation processing, nuclear energy science and technology and nuclear physics in both experimental and theoretical fields, applied in physics, chemistry, biophysics, biology, medicine, medical physics, engineering and environmental sciences are welcome.

Relevant topics for RPE include the following:

- Nuclear Reactor Technology: design, calculations, measurements.
- Radiation Sources: design, construction, production, characteristics, activation cross-sections, target design, processing, quality control procedures.
- Particle Accelerators Ion Sources: beam transport systems and target arrangements as well as the use of secondary phenomena such as synchrotron radiation and free electron lasers: design, applications, calculations and measurements.
- Fusion: related technology and equipment, measurements and calculations.
- Measurement of Radiation and Radioactivity: measurement of X-rays, γ-rays, α- and β-particles and other forms of radiation; nuclear instrumentation, including radiation spectrometry, dosimetry, novel counting systems and whole-body counters, novel radiation detector systems.
- Radioanalytical Methods and Radiochemistry: activation analysis, isotope dilution analysis, radioimmunoassay, radionuclide tomography, radiation spectrometry, synthesis of labelled compounds, chemical behavior and speciation of radionuclides.
- Nuclear Physics: nuclear structure, nucleon-nucleon interaction, nuclear reactions, Hadronic physics, few-body problems, effective filed theory.

Types of article:

- Full-length article: unlimited number of pages and figures, following the Full-length articles, which should be definitive and describe a reasonably complete investigation.
- Review article: submitted only by request and with previous agreement of the Editors.
- Technical note: specifically addressing technical issues not qualifying as original research work.
- Discussion: questioning the content of published articles by other authors.

GUIDELINES AND POLICIES

Ethical Responsibilities of Authors

Authors should observe the following codes of conduct when they intend to submit/publish a paper. Maintaining integrity of the research and its presentation can be achieved by following the rules of good scientific practice, which include:

- The manuscript has not been submitted to more than one journal for simultaneous consideration.
- The manuscript has not been published previously (partly or in full), unless the new work concerns an expansion of previous work (please provide transparency on the re-use of material to avoid the hint of text-recycling (self-plagiarism)).
- A single study is not split up into several parts to increase the quantity of submissions and submitted to various journals or to one journal over time.
- No data have been fabricated or manipulated (including images) to support your conclusions.
- No data, text, or theories by others are presented as if they were the authors own (plagiarism). Proper acknowledgements to other works must be given (this includes material that is closely copied (near verbatim), summarized and/or paraphrased), quotation marks are used for verbatim copying of material, and permissions are secured for material that is copyrighted.
- Important note: the journal may use software to screen for plagiarism. The plagiarism is checked through two methods: reviewer check and plagiarism prevention tool (iThenticate). All submissions will be checked by online software before being sent to reviewers.
- Consent to submit has been received explicitly from all co-authors, as well as from the responsible authorities - tacitly or explicitly - at the institute/organization where the work has been carried out, before the work is submitted.
- Authors whose names appear on the submission have contributed sufficiently to the scientific work and therefore share collective responsibility and accountability for the results.
- Changes of authorship or in the order of authors are not accepted after acceptance of a manuscript. Authors are expected to consider carefully the list and order of authors before submitting their manuscript and provide the definitive list of authors at the time of the original submission. Any addition, deletion or rearrangement of author names in the authorship list should be made only before the manuscript has been accepted and only if approved by the journal Editor. To request such a change, the Editor must receive the following from the corresponding author: (a) the reason for the change in author list and (b) written confirmation (e-mail, letter) from all authors that they agree with the addition, removal or rearrangement. In the case of addition or removal of authors, this includes confirmation from the author being added or removed.

For more information about instructions to authors and preparing a manuscript for submission, please visit journal website: **http://rpe.kntu.ac.ir**

Radiation Physics and Engineering

ISSN 2645-6397

An international scientific-research journal published quarterly by K.N. Toosi University of Technology jointly with Nuclear Society of Iran

Vol. 4, Issue 2, Spring 2023

Contents

1 Radiation hazards from granite and bitumen in construction material site in Aniocha South Local Government Area of Delta State, South-South Nigeria
B. Okeoghene Ijabor, A. Daniel Omojola, A. Onyema Nwabuoku, F. Ruth Omojola 1

2 Studying the effect of backgrounds on the determination of radiative thermal neutron capture cross-section in the Neutron Powder Diffraction facility of the Tehran Research Reacto
M. Pazoki, H. Jafari, Z. Gholamzadeh 9

3 Effect of marker material on the dosimetric parameters of I-125 source (model 6711): Monte Carlo simulation
P. Taherparvar, A. Azizi Ganjgah 19

4 Computational study of the effect of sapphire neutron filter on reducing the neutron and secondary-gamma dose rate around the main shield of D channel in TRR
Z. Gholamzadeh 25

5 Design and construction of the experimental plasma water activation
M. Omrani, H. Sadeghi, S. Fazelpour 35

6 Investigation of radiation-matter interaction effects on burn process of nonequilibrium deuterium-tritium plasma in inertial confinement fusion approach
M. Nazirzadeh, B. Khanbabaei, H. Alborznia 39

7 Calculation of the role of Wigner energy in decontamination of Cs-137 from irradiated Graphite pores
M. Nikoosefat, A. Bagheri, H. Shakur, Z. Shahbazi Rad, N. Javadi 45

8 Assignment of a radiological map of the city of Borujerd in Iran
R. Pourimani, M. Bajelan, M. Mohebian 53

RPE | Radiation Physics & Engineering
An International Peer-Reviewed Journal
Published by K.N. Toosi University of Technology
http://rpe.kntu.ac.ir
Research Article

Radiation Physics and Engineering 2023; 4(2):1–8

Radiation hazards from granite and bitumen in construction material site in Aniocha South Local Government Area of Delta State, South-South Nigeria

Blessing Okeoghene Ijabor[a], Akintayo Daniel Omojola[b,*], Augustine Onyema Nwabuoku[c], Funmilayo Ruth Omojola[d]

[a] *Department of Science Laboratory Technology, Delta State Polytechnic, Ogwashi-Uku, Delta State, Nigeria*
[b] *Radiology Department, Medical Physics Unit, Federal Medical Centre Asaba, Asaba, Delta State, Nigeria*
[c] *Department of Physics, Delta State University, Abraka, Delta State, Nigeria*
[d] *Department of Cancer Biology and Therapy, University of Central Lancashire, Preston, United Kingdom*

HIGHLIGHTS

- Granite and bitumen from different geographical location have different radiation levels.
- Most workers in construction/material deposit sites are not aware of the impact of ionizing radiation.
- The ADR was 3 times higher than the world average.
- The effective lifetime cancer risk (ELCR) was above the acceptable risk band (10^{-6} to 10^{-4}).

ABSTRACT

The study is aimed at measuring the background ionizing radiation (BIR), the absorbed dose rate (ADR), the annual effective dose (AED) and excessive lifetime cancer risk (ELCR) at four sites in the Aniocha South local government area (LGA) of Delta State, denoted as A to D. The study was performed using a calibrated Geiger-Muller (GM) detector (Radiation Alert Inspector) as well as a geographic positioning system (GPS) to determine the longitude and latitude of each site. The average (range) outdoor BIR, ADR, and AED were 0.021 ± 0.01 (0.01 to 0.04) mR.hr^{-1}, 181.6 ± 77.7 (60.9 to 322.8) nGy.hr^{-1}, and 0.22 ± 0.10 (0.07 to 0.40) mSv.yr^{-1}, respectively. Among the processing sites, the average AED for granite, bitumen, and staff residential areas were 0.31, 0.12, and 0.17 mSv.yr^{-1}, while surface measurements at the "burnt stone" had the highest AED (0.41 mSv.yr^{-1}). ADR and AED were both considerably higher than the world average of 59 nGy.hr^{-1} and 0.07 mSv.yr^{-1}. The average effective lifetime cancer risk (ELCR) was 7.7×10^{-4} (1 in 1,300), with the highest in the granites. The ELCR risk grade was high ($> 10^{-4}$), suggesting that remedial action be taken to ensure safety in the granite sites based on the environmental protection agency (EPA) United States report.

KEYWORDS

Background ionizing radiation
Global positioning system
Radionuclide
Granite
Bitumen

HISTORY

Received: 19 May 2022
Revised: 26 July 2022
Accepted: 14 August 2022
Published: Spring 2023

1 Introduction

Many radioactive elements are naturally occurring within the earth's crust as deposits (Abed et al., 2022). All soils contain trace levels of terrestrial radionuclides, resulting in radiological exposures outdoors (Ahmad et al., 2019; Doyi et al., 2017). There are specific levels for different types of soil determined by the rock. Granite is an igneous rock with higher radiation levels, while sedimentary rocks have low levels (Roy et al., 2022; Kapanadze et al., 2021). The exception comes from certain rocks, such as shales and phosphates, which contain a lot of radionuclides (Missimer et al., 2019; Boryło et al., 2017).

The primary sources of Potassium 40 (K-40), Uranium 238 (U-238), and Thorium 232 (Th-232) are rock, soil, and groundwater. Radium (Ra-228, Ra-226, and Ra-224) and Radon (Rn) undergo spontaneous disintegration to produce daughter particles with alpha, beta, or gamma-ray emission (Joel et al., 2021; Mathuthu et al., 2021; Degu Belete and Alemu Anteneh, 2021; Napoli et al.,

*Corresponding author: akintayo.omojola@fmcasaba.org

https://doi.org/10.22034/rpe.2022.342868.1090
https://dorl.net/dor/20.1001.1.26456397.2023.4.2.1.7

2021).

Radiation protection in the environment is poorly understood by the public (Hobbs et al., 2018; Slovic, 2012). We also found this to be true in an interview with granite and bitumen workers at various sites. However, they have virtually no awareness of radiation protection. An individual's educational background may also limit their knowledge, although this fact hasn't been explored. Over the years, the numbers of granite and bitumen processing sites for road constructions have increased due to large deposit of granite, limestone, laterite and bitumen in Nigeria (Oyedele et al., 2016; Akpan et al., 2011; Magaji et al., 2020).

Many surveys have been conducted to determine the background levels of radionuclides in granites, which can be related to the absorbed dose rates in the air. Many of which have been found to vary based on geographical location (UNSCEAR, 2000; Shahbazi-Gahrouei et al., 2013).

The average of absorbed dose rate (ADR) and annual effective dose (AER) from terrestrial gamma radiation was 59 nGy.hr^{-1} and 0.07 mSv.yr^{-1}, respectively based on the United Nations Scientific Committee on the Effects of Atomic Radiation (UNSCEAR) report from large surveys (UNSCEAR, 2000). Extremely high values have been recorded in places in Kerala in India with up to 70 mGy.yr^{-1} (Nair et al., 2009), while another study in same area by Sudheer et al. have reported an average AER of $<$ 1 to 45 mGy.yr^{-1} (Sudheer et al., 2022), however, there has been no evidence of cancer-related cases in places where these values are high but chromosome aberration have been identified from samples collected (Gh et al., 2019).

The excessive lifetime cancer risk (ELCR) have been divided into 4 groups of very high ($> 10^{-64}$), high (10^{-4} to 10^{-5}), moderate (10^{-5} to 10^{-6}) and low ($< 10^{-6}$) from the development of a nationwide excessive lifetime cancer risk in Korea (Kang et al., 2021). The United States has adopted the use of the environmental protection agency report, which has graded ELCR as negligible ($< 10^{-6}$), acceptable (10^{-6} to 10^{-4}) and remediation may be desirable ($> 10^{-4}$) (EPA, 2014).

The focus of this study is in the Aniocha South Local Government Area, which lies in the Northern region of Delta State with an area of 868 square kilometers (km^2). The purpose of the study is to estimate the average background ionizing radiation (BIR), annual dose rate (ADR), annual effective dose (AED) and excessive lifetime cancer risk (ELCR) from granite (crushed to different sizes), bitumen and staff residential areas within the processing sites in the above LGA. Similarly, this study compared the results with locally and internationally.

2 Materials and Methods

This research was a prospective and experimental based study, which was carried out for 3 months, in 4 construction dump sites (A and D = Otulu, B and C = Ubulu Okiti) in Aniocha South LGA of Delta state. Convenience sampling method was used in the selection process. A global positioning system (GPS) instrument and an Inspector USB survey meter calibrated in a Secondary Standard Dosimetry Laboratory (SSDL) in the National Institute of Radiation Protection and Research (NIRPR), University of Ibadan, Oyo State, Nigeria.

Radiation measurements were performed with a calibrated inspector USB survey meter. Inspection USB survey meter (S.E. International, Inc.), is health and safety instrument that detects low levels of radiation. Specifically, the instrument measures ionizing radiation, including Alpha and Beta particles, Gamma rays, and X-rays (Fig. 1). There are two different units of measurement for the survey meter: milliroengens per hour (mR.hr^{-1}) and counts per minute (CPM), or microsieverts per hour (Sv.hr^{-1}) and counts per second (CPS) with an operating range of 0.001 (1 μR) to 100 mR.hr^{-1} or 0 to 350,000 CPM (Table 1). The Global Positioning System (GPS) application software was downloaded and used to measure the longitudes, latitudes, and elevations of points in all the studied areas (Fig. 2).

Figure 1: Geiger Muller survey meter (back and front side).

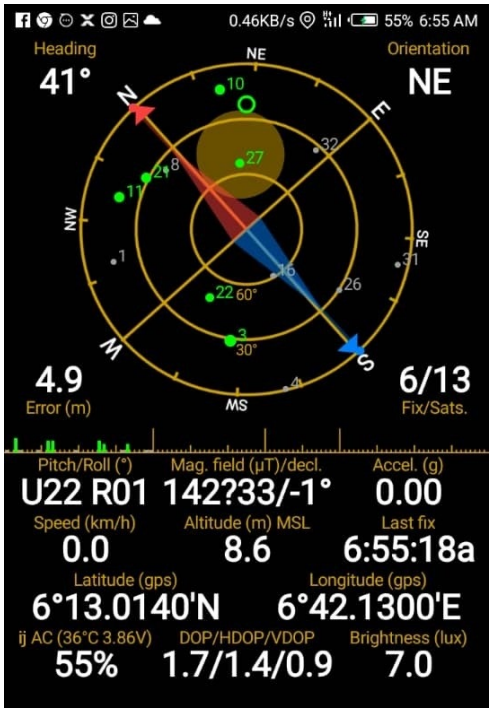

Figure 2: GPS system.

Figure 3: The construction dump sites for bitumen and granite.

2.1 Set-up for measurements

The survey meter was switched to the total timer (CPM or CPS) mode in order for the device to record reading electronically in count per minute (CPM) mode for a minimum time of 60 seconds. The sensitive area of the device was positioned in such a way that it faces the sample and it is about 30 cm (0.3 m) away from it. Simultaneously, the GPS device was activated to record the longitude, latitude and altitude of the point for BIR measurement. A total of 3 measurements were made per point in the sites (Fig. 3) and the average BIR was calculated.

The survey meter was used on the CPM mode and measurement was timed for a total of 180 seconds (3 measurements at 60 s). Conversion to milliroentgen per hour ($\mathrm{mR.hr^{-1}}$) was carried out using the meter's calibration factor (3340 $\mathrm{CPM.mR^{-1}.hr^{-1}}$). The relationship between CPM and $\mathrm{mR.hr^{-1}}$ was given as (Omojola et al., 2020):

$$\mathrm{mR.hr^{-1}} = \frac{x\ \mathrm{CPM}}{3340\ \dfrac{\mathrm{CPM}}{\mathrm{mR.hr^{-1}}}} \tag{1}$$

where x is the count recorded by the survey meter in CPM.

Measurement with both detectors was done simultaneously on the same point and data was entered in a record book for documentation. The BIR measurement was computed in CPM and was converted to $\mathrm{mR.hr^{-1}}$ using Eq. (1).

The annual dose rate (ADR) was estimated based on the Canadian Health and Safety Code 35 for the installation, use, and control of X-ray equipment, which is given as (Health-Canada, 2008):

$$1\ \mathrm{mR.hr^{-1}} = 8700\ \mathrm{nGy.hr^{-1}} \tag{2}$$

The annual effective dose (AED) was given as:

$$\begin{aligned}\mathrm{AED\ (Outdoor)\ (mSv.hr^{-1})} = \\ \mathrm{ADR\ (nGy.hr^{-1})} \times 8760\ \mathrm{(hr^{-1})} \\ \times 0.7\ \mathrm{(Sv.Gy^{-1})} \times 0.2\end{aligned} \tag{3}$$

AED was calculated using the dose conversion factor of 0.7 $\mathrm{Sv.Gy^{-1}}$ as recommended (UNSCEAR, 1993) for the conversion coefficient from the absorbed dose in air to the effective dose received by adults and an occupancy factor of 0.2 for outdoor exposure (UNSCEAR, 1993). The excessive lifetime cancer risk (ELCR) was estimated as:

$$\begin{aligned}\mathrm{ELCR} = \mathrm{ADR\ (nGy.hr^{-1})} \\ \times \text{Average duration of life (DL)} \\ \times \text{Risk factor (RF)}\end{aligned} \tag{4}$$

Where AEDE is the annual effective dose equivalent, DL is duration of life (70 years) and RF is the fatal cancer risk factor ($\mathrm{Sv^{-1}}$). For low-dose background radiation, this is considered to produce stochastic effects, the fatal cancer risk factor value of 0.05 for public exposure (Sievert and Failla, 1959).

2.2 Statistical Analysis

The study used descriptive statistics (average, median and standard deviation), a One-Sample t-test, One-Way ANOVA and Pearson correlation to analyze the results. $P < 0.05$ was considered to be statistically significant and vice versa.

3 Results and Discussion

The map in Fig. 4 indicates the points of measurement from the 4 construction dump sites in Otulu and Ubulu Okiti, denoted as A to D, while Fig. 5 shows the BIR contour map. In site A, four sizes of granite stones were measured. The average (range) altitude was 199 (141 to 222) m and the maximum ADR (322.8 $\mathrm{nGy.hr^{-1}}$) and AED (0.4 $\mathrm{mSv.yr^{-1}}$) were measured on the surface of the burnt stone. The values were approximately 6 times higher than the world average (UNSCEAR, 2000). Measurements around the bitumen area showed the least AED, which was lower than measurements in the staff residential areas. A One-Sample T-test showed that there was a statistically significant difference in BIR, ADR, and AED ($P < 0.001$) (Table 2).

This study measured three sizes of granite stones at site B at altitude of 240 (195 to 256) m. No matter how big or small the granite was, the BIR and AED measurements were identical. Furthermore, the average BIR was twice as high as the world average, while the average ADR and AED were three times as high. It was found that measurements near bitumen tanks had the lowest ADR (60.9 $\mathrm{nGy.hr^{-1}}$) and AED (0.07 $\mathrm{mSv.yr^{-1}}$), which is similar to the UNSCEAR 2000 report (UNSCEAR, 2000), where 59 $\mathrm{nGy.hr^{-1}}$ and 0.07 $\mathrm{mSv.yr^{-1}}$ were reported. One-Sample T-Test results indicated that altitude ($P = 0.001$), BIR ($P = 0.001$), ADR ($P = 0.001$), and AED ($P = 0.001$) were statistically significantly different (Table 3).

Measurements of 4 sizes of granite stones were made at site C at altitude of 253 (248 to 255) m. Of the four sizes of granite stones, the $\frac{3}{4}$ inch stone showed the highest dose rate. AED and BIR measurements were essentially the same regardless of granite size (2 and 1 decimal place, respectively). The lowest dose rate was recorded around the bitumen and staff quarters, which was above the global average (Table 4).

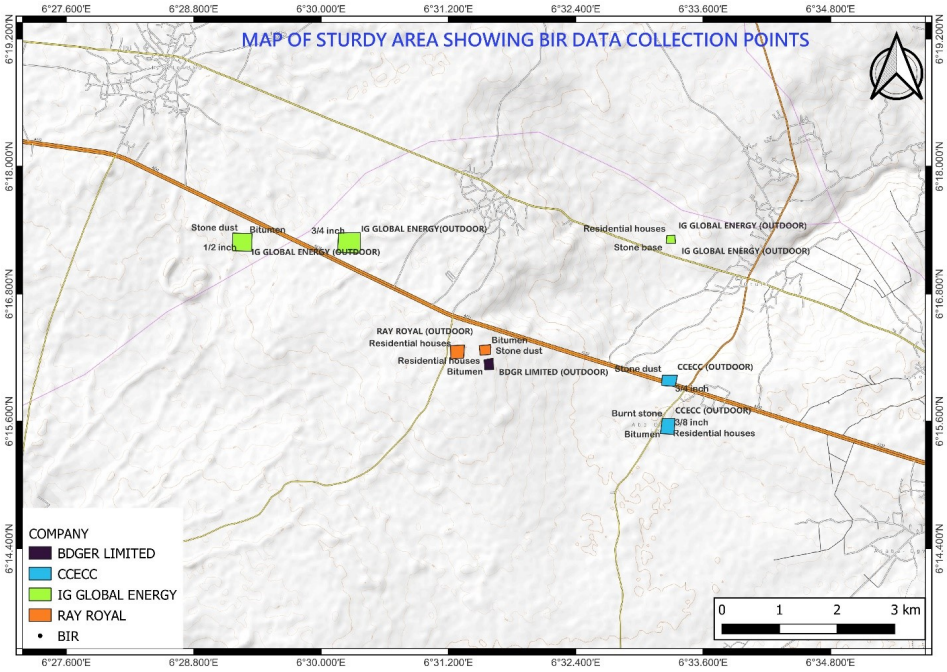

Figure 4: Map showing granite and bitumen construction sites A to D.

Table 1: Technical specifications of survey meter.

Display	Backlit 4 digit liquid crystal display with indicator. Display updates every 3 s
Alert set range	mR.hr^{-1} 0.001-50, CPM 1 to 160,000
Count light	Red LED flashes with each radiation event
Audio indicator	Internally mounted beeper
Detector	Internal Halogen-Quenched uncompensated GM Tube with thin mica window 1.4 to 2.0 mGy.cm^{-2} area density
Operating Range	mR.hr^{-1} = 0.001 to 100 CPM = 0 to 350,000 μSv.hr^{-1} = 0.01 to 1000 CPS = 0 to 5,000
Total/Time	1 to 9,999,000 counts
Energy Sensitivity	Detect alpha down to 2 MeV and Beta down to 0.16 MeV Typical detection efficiency at 1 MeV is $\sim$ 25% Detect gamma down to 10 KeV through the window
Accuracy (Cs-137)	mR.hr^{-1} $\pm$ 10% typical (NIST), 15% Max 0.001 to 100 μSv.hr^{-1} $\pm$ 10% typical (NIST), 15% Max 0.01 to 1000 CPM $\pm$ 10% typical (NIST), 15% Max 0 to 350,000
Power requirement	A 9 V alkaline batteries
Temperature	-10 °C to 50 °C (14 °F to 122 °F)

Table 2: The geographical location and average BIR, ADR, and AED measurements in granite and bitumen construction site (A) in Otulu, Aniocha LGA.

S/N	Gravel area	Geographical location	Altitude (m)	Average BIR (mR.hr^{-1})	ADR (nGy.hr^{-1})	AED (mSv.yr^{-1})
1	3/8 inch	N060 15.59′, E060 33.25′	141	0.023	198.4	0.24
2	3/4 inch	N060 16.00′, E060 33.27′	194	0.033	282.8	0.35
3	Stone-dust	N060 16.00′, E060 33.27′	195	0.032	281.0	0.34
4	Burnt-stone	N060 15.58′, E060 33.28′	193	0.037	322.8	0.40
	Bitumen area					
1	In tanks	N060 15.57′, E060 33.26′	219	0.013	109.6	0.13
2	Around tanks	N060 15.57′, E060 33.25′	222	0.013	113.1	0.14
	Staff residence area					
1	Inside the houses	N060 15.58′, E060 33.25′	212	0.014	118.3	0.15
2	Around the houses	N060 15.58′, E060 33.25′	212	0.016	139.2	0.17

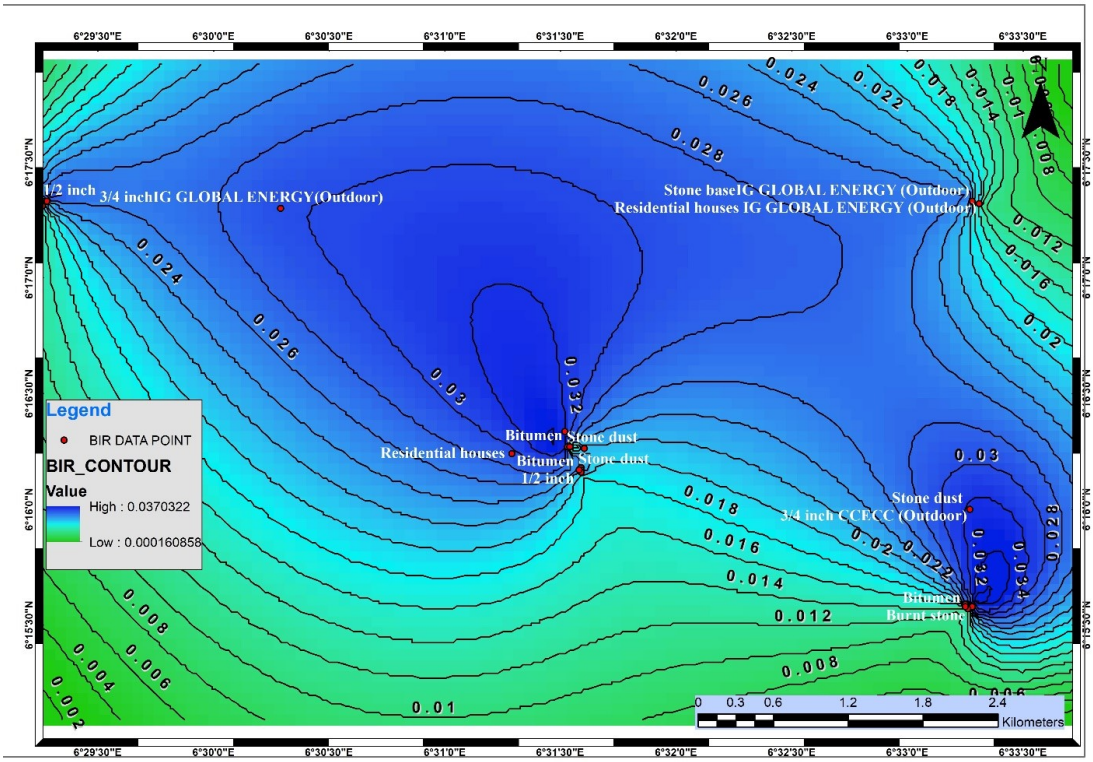

Figure 5: Map showing BIR measurements.

Table 3: The geographical location and average BIR, ADR, and AED measurements in granite and bitumen construction site (B) in Ubulu Okiti, Aniocha LGA.

S/N	Gravel area	Geographical location	Altitude (m)	Average BIR ($mR.hr^{-1}$)	ADR ($nGy.hr^{-1}$)	AED ($mSv.yr^{-1}$)
1	3/8 inch	N060 16.25′, E060 31.53′	253	0.030	260.13	0.32
2	Small-stone	N060 16.27′, E060 31.53′	250	0.028	240.99	0.30
3	Stone-dust	N060 16.28′, E060 31.54′	195	0.029	249.69	0.31
	Bitumen area					
1	In tanks	N060 16.27′, E060 31.54′	256	0.009	76.56	0.09
2	Around tanks	N060 16.27′, E060 31.52′	247	0.007	60.9	0.07
	Staff residence area					
1	Inside the houses	N060 16.24′,E060 31.29′	242	0.029	252.3	0.31
2	Around the houses	N060 16.24′,E060 31.29′	240	0.025	217.5	0.27

Table 4: The geographical location and average BIR, ADR, and AED measurements in granite and bitumen construction site (C) in Ubulu Okiti, Aniocha LGA.

S/N	Gravel area	Geographical location	Altitude (m)	Average BIR ($mR.hr^{-1}$)	ADR ($nGy.hr^{-1}$)	AED ($mSv.yr^{-1}$)
1	3/4 inch	N060 17.30′, E060 30.29′	251	0.0298	259.3	0.32
2	1/2 inch	N060 17.33′, E060 29.27′	255	0.0255	221.9	0.27
3	Stone-dust	N060 17.33′, E060 29.28′	254	0.0293	254.9	0.31
4	Stone-base	N060 17.33′, E060 33.28′	254	0.0265	230.6	0.28
	Bitumen					
1	in tanks	N060 17.31′, E060 29.26′	253	0.0115	100.1	0.12
2	around tank	N060 17.31′, E060 29.25′	254	0.0117	101.8	0.13
	Staff residence					
1	Inside the houses	N060 17.32′, E060 33.31′	251	0.0113	98.3	0.12
2	Around the houses	N060 17.32′, E060 33.32′	248	0.0115	100.1	0.12

Table 5: The geographical location and average BIR, ADR, and AED measurements in granite and bitumen construction site (D) in Otulu, Aniocha LGA.

S/N	Gravel area	Geographical location	Altitude (m)	Average BIR ($mR.hr^{-1}$)	ADR ($nGy.hr^{-1}$)	AED ($mSv.yr^{-1}$)
1	3/4 inch	N060 16.18′, E060 31.59′	231	0.026	226.2	0.28
2	1/2 inch	N060 17.33′, E060 29.27′	255	0.026	221.9	0.27
3	Stone dust	N060 17.33′, E060 29.28′	254	0.029	254.9	0.31
4	Stone base	N060 17.33′, E060 33.28′	254	0.027	230.6	0.28
	Bitumen area					
1	in tanks	N060 17.31′, E060 29.26′	253	0.012	100.1	0.12
2	around tank	N060 17.31′, E060 29.27′	255	0.012	101.8	0.13
	Staff residence area					
1	Inside the houses	N060 17.32′, E060 33.31′	251	0.012	101.8	0.12
2	Around the houses	N060 17.32′, E060 33.33′	253	0.012	103.5	0.13

Table 6: Comparison of the average measurements in this study with other published articles and world average.

Study/Report	BIR ($mR.hr^{-1}$)	ADR ($nGy.hr^{-1}$)	AED ($mSv.yr^{-1}$)
This study	0.02 ± 0.01	181.6 ± 77.7	0.22 ± 0.10
(UNSCEAR, 2000)	0.01	59	0.07
(Ijabor et al., 2022)	0.01 ± 0.002	91.6 ± 19.5	0.11 ± 0.02
(Onwuka and Ononugbo, 2019)	0.026	228.4	0.28
(Akerblom and Mjones, 2000)	-	-	0.1 to 0.4
(Yousef et al., 2019)	-	129.2	-
(Okedeyi et al., 2012)	0.0015	2.3 to 19.4	0.0026 to 0.0024
(Samuel, 2018)	-	18.87	0.25
(Myatt et al., 2010)	-	-	0.005 to 0.18
(Orosun et al., 2019)	-	57.68	0.07

A similar trend is evident in Table 5 for granite, which showed the highest dose rate. Both bitumen and residential areas received the same dose rate. Based on the One-Sample T-test, the dose rate parameters were statistically different among them. The One-Way ANOVA test revealed that there was no significant difference in the average measurements taken at each of the four construction dump sites in Aniocha South LGA ($P > 0.05$). Granite had a dose rate that was 3 times higher than bitumen and 2 times higher than the staff residential areas. Only 3% of the AED matched the global average value. A correlation in AED was also found between sites A and C ($P = 0.008$) and A and D ($P = 0.002$), indicating a close association between the measurements. Comparison of this study with a similar work in Aniocha South Local Government Area by Ijabor et al., who investigated radiation level in 17 petrol stations, shows that the BIR, ADR and AED were doubled. Indicating that the radiation levels in the granites were higher compared to refined petroleum products (Ijabor et al., 2022).

This study is comparable to a work in Ebony State, Nigeria by Onwuka and Ononugbo, who determined dose rate measurement in quarry site. The average dose rate from their study was 0.026 $mR.hr^{-1}$, which was slightly above this study (0.021 $mR.hr^{-1}$). The average ADR (330 $nGy.hr^{-1}$) was twice and AED (2.21 $mSv.yr^{-1}$) was 6 times this study (Table 6). The geographical location and activities of the granite might cause the difference in dose rate (Onwuka and Ononugbo, 2019).

A study in Sweden by Akerblom and Mjones shows that workers in quarry site were exposed to 0.1 to 0.4 $mSv.yr^{-1}$, this value was 10 times in range higher compared to our study (0.01 to 0.04 $mSv.yr^{-1}$) from construction dump sites of granite and bitumen (Akerblom and Mjones, 2000) (Table 6).

The concentration of Radon and average annual effective dose for granite samples collected from Abu Rusheid area, South Eastern Desert, Egypt, were measured using passive technique with CR-39 and was found to be 129.2 $mSv.yr^{-1}$, this value was over 500 times higher compared to our study. The CR-39 is known to be insensitive to X-ray, beta and gamma particles. The result indicated that geographical position and the concentration of radioactive materials could greatly vary from one region to another (Yousef et al., 2019) (Table 6).

Conversely a study on dose rate measurement on bedrocks and soil in quarry sites in Ogun State, South-West Nigeria by Okedeyi et al., show that ADR value ranged from 2.3 to 19.4 $nGy.hr^{-1}$ and AED ranged from 2.6 to 23.81 $mSv.yr^{-1}$ (Okedeyi et al., 2012). Similarly, the maximum ADR and AED from a study by Samuel et al in Benue State, Nigeria from quarry granite site were 18.87 $nGy.hr^{-1}$ and 0.25 $mSv.yr^{-1}$ (Samuel, 2018). In addition, a study by Myatt et al, on granite countertops shows a range of 0.005 to 0.18 $mSv.yr^{-1}$. A possible reason for dose rate reduction may be attributed to the finishing of the granite, which may have interfered with the overall activities (Myatt et al., 2010) (Table 6). The values were lower compared to those obtained in this study. This was also the case in a study by Orosun et al., who determined

dose rate from granite mining fields in Asa, North-Central Nigeria. The results (ADR = 59 nGy.hr^{-1}; AED = 0.07 mSv.yr^{-1}) were below our study and were below the world average values (Orosun et al., 2019).

The excessive lifetime cancer risk (ELCR) for the granite, bitumen and staff residential areas ranged from $(1.0-1.16)\times10^{-3}$, $(0.280.47)\times10^{-3}$ and $(0.421.02)\times10^{-3}$ respectively with the highest in granites. The average value in the granite (with different sizes) was $(1.07)\times10^{-3}$. The average ELCR in this study was lower compared to studies in Korea, Pakistan, Nigeria and India (Kang et al., 2021; Qureshi et al., 2014; Isinkaye and Emelue, 2015; Jeelani et al., 2021) and was higher compared to a study in Egypt (Abdel Gawad et al., 2022) (Table 7). The geographical locations of the samples played a major role in the variation of the data obtained.

The UNSCEAR 2000 report is an average value from country reports which is on the average of 0.29×10^{-3}. The average value from our study was lower compared to the world average but ELCR from the granite was higher. The EPA document has graded risk not according to the world average but according to the hazards it may cause. Our study was found to be graded as "high" and with risk of 0.77×10^{-3} (1 per 1,300), connoting that remedial action is required in the site.

Table 7: Comparison of excessive lifetime cancer risk with other studies.

Study	ELCR ($\times10^{-6}$)
This study	0.77×10^{-3}
(UNSCEAR, 2000)	0.29×10^{-3}
(Kang et al., 2021)	3.21×10^{-3}
(Qureshi et al., 2014)	3.21×10^{-3}
(Isinkaye and Emelue, 2015)	3.21×10^{-3}
(Jeelani et al., 2021)	3.06×10^{-3}
(Abdel Gawad et al., 2022)	3.35×10^{-3}

4 Conclusions

A study to estimate BIR, ADR, AED and ELCR have been carried out in 4 construction processing/dump site in Aniocha South LGA of Delta State. The average ELCR from this study was below the world average but showed a high risk from the environmental protection agency (EPA) report, suggesting that remedial action be taken in terms of safety. This study will create awareness and improve regulatory compliance in the department environment and mineral resources in Delta State through regular radiation monitoring and awareness programme in construction dump sites.

Conflict of Interest

The authors declare no potential conflict of interest regarding the publication of this work.

Copyright

References

Abdel Gawad, A. E., Ali, K. G., Wahed, A. A. A., et al. (2022). Excess Lifetime Cancer Risk Associated with Granite Bearing Radioactive Minerals and Valuable Metals, Monqul Area, North Eastern Desert, Egypt. *Materials*, 15(12):4307.

Abed, N. S., Monsif, M. A., Zakaly, H. M., et al. (2022). Assessing the radiological risks associated with high natural radioactivity of microgranitic rocks: A case study in a northeastern desert of Egypt. *International Journal of Environmental Research and Public Health*, 19(1):473.

Ahmad, A. Y., Al-Ghouti, M. A., AlSadig, I., et al. (2019). Vertical distribution and radiological risk assessment of ^{137}cs and natural radionuclides in soil samples. *Scientific Reports*, 9(1):1–14.

Akerblom, G. and Mjones, L. (2000). Exposure to workers in Swedish quarrying. Swedish Radiation Protection Authority SE-171 16. *Stockholm, Sweden*.

Akpan, I., Amodu, A., Akpan, A., et al. (2011). An assessment of the major elemental composition and concentration in limestones samples from Yandev and Odukpani areas of Nigeria using nuclear techniques. *Journal of Environmental Science and technology*, 4(3):332–339.

Boryło, A., Romańczyk, G., and Skwarzec, B. (2017). Lichens and mosses as polonium and uranium biomonitors on Sobieszewo Island. *Journal of Radioanalytical and Nuclear Chemistry*, 311(1):859–869.

Degu Belete, G. and Alemu Anteneh, Y. (2021). General Overview of Radon Studies in Health Hazard Perspectives. *Journal of Oncology*, 2021.

Doyi, I., Essumang, D., Dampare, S., et al. (2017). Evaluation of radionuclides and decay simulation in a terrestrial environment for health risk assessment. *Scientific Reports*, 7(1):1–11.

EPA, U. (2014). Human Health Risk Assessment Homestake Mining Co. Superfund Site Cibola County, New Mexico: Risk and Site Assessment Section (6SF-TR). Region 6.

Gh, M., Paknahad, M., et al. (2019). Is induction of anomalies in lymphocytes of the residents of high background radiation areas associated with increased cancer risk? *Journal of Biomedical Physics & Engineering*, 9(3):367.

Health-Canada (2008). Safety Code 35: Safety Procedures for the Installation, Use and Control of X-Ray Equipment in Large Medical Radiological Facilities. Cat. No.: H128-1/08-545E. *Ottawa (ON): Minister of Health*.

Hobbs, J. B., Goldstein, N., Lind, K. E., et al. (2018). Physician knowledge of radiation exposure and risk in medical imaging. *Journal of the American College of Radiology*, 15(1):34–43.

Ijabor, B. O., Omojola, A. D., Omojola, F. R., et al. (2022). Radiological assessment of petroleum products in Aniocha South Local Government Area of Delta State, South-South Nigeria. *Radiation Protection and Environment*, 45(1):33.

Isinkaye, M. and Emelue, H. (2015). Natural radioactivity measurements and evaluation of radiological hazards in sediment of Oguta Lake, South East Nigeria. *Journal of Radiation Research and Applied Sciences*, 8(3):459–469.

Jeelani, G., Hassan, W., Saleem, M., et al. (2021). Gamma dose monitoring to assess the excess lifetime cancer risk in western Himalaya. 328(1):245–258.

Joel, E., Omeje, M., Olawole, O., et al. (2021). In-situ assessment of natural terrestrial-radioactivity from Uranium-238 (U-238), Thorium-232 (Th-232) and Potassium-40 (K-40) in coastal urban-environment and its possible health implications. *Scientific Reports*, 11(1):1–14.

Kang, D., Lee, S. H., Kim, Y. J., et al. (2021). Development of Nationwide Excess Lifetime Cancer Risk Evaluation Methods with Comprehensive Past Asbestos Exposure Reconstruction. *International Journal of Environmental Research and Public Health*, 18(6):2819.

Kapanadze, K., Magalashvili, A., and Imnadze, P. (2021). Radiological hazards assessment due to natural radioactivity in soils from Imereti region (Georgia). *Arabian Journal of Geosciences*, 14(12):1–9.

Magaji, B., Zubairu, M., Ladan, M., et al. (2020). Analysis of Limestone Samples from Deposits at Selected Nigeria Areas as a Potential Raw Material for the Production of Portland cement. *International Journal of Modern Analytical and Separation Sciences*, pages 14–27.

Mathuthu, M., Uushona, V., and Indongo, V. (2021). Radiological safety of groundwater around a uranium mine in Namibia. *Physics and Chemistry of the Earth, Parts A/B/C*, 122:102915.

Missimer, T. M., Teaf, C., Maliva, R. G., et al. (2019). Natural radiation in the rocks, soils, and groundwater of Southern Florida with a discussion on potential health impacts. *International Journal of Environmental Research and Public Health*, 16(10):1793.

Myatt, T. A., Allen, J. G., Minegishi, T., et al. (2010). Assessing exposure to granite countertopspart 1: radiation. *Journal of Exposure Science & Environmental Epidemiology*, 20(3):273–280.

Nair, R. R. K., Rajan, B., Akiba, S., et al. (2009). Background radiation and cancer incidence in Kerala, IndiaKaranagappally cohort study. *Health Physics*, 96(1):55–66.

Napoli, E., Bønsdorff, T. B., Jorstad, I. S., et al. (2021). Radon-220 diffusion from ^{224}Ra-labeled calcium carbonate microparticles: Some implications for radiotherapeutic use. *Plos One*, 16(3):e0248133.

Okedeyi, A., Gbadebo, A., Arowolo, T., et al. (2012). Measurement of gamma radioactivity level in bedrocks and soils of quarry sites in ogun state, south-western, nigeria. *Research Journal of Physics*, 6(2):59–65.

Omojola, A. D., Omojola, F. R., Akpochafor, M. O., et al. (2020). Shielding assessment in two computed tomography facilities in South-South Nigeria: How safe are the personnel and general public from ionizing radiation? *The ASEAN Journal of Radiology*, 21(2):5–27.

Onwuka, M. and Ononugbo, C. (2019). Radiometric Survey of Granitic Quarry Site of Ebony State, Nigeria. *AIR*, pages 1–9.

Orosun, M. M., Usikalu, M. R., Oyewumi, K. J., et al. (2019). Natural radionuclides and radiological risk assessment of granite mining field in Asa, North-central Nigeria. *MethodsX*, 6:2504–2514.

Oyedele, K. F., Oladele, S., and Emakpor, C. A. (2016). Exploration for limestone deposit at Onigbedu, South-Western Nigeria. *Mater. Geoenviron*, 63(2):139–150.

Qureshi, A. A., Tariq, S., Din, K. U., et al. (2014). Evaluation of excessive lifetime cancer risk due to natural radioactivity in the rivers sediments of Northern Pakistan. *Journal of Radiation Research and Applied Sciences*, 7(4):438–447.

Roy, D., Siraz, M., Dewan, M., et al. (2022). Assessment of terrestrial radionuclides in the sandy soil from Guliakhali beach area of Chattogram, Bangladesh. *Journal of Radioanalytical and Nuclear Chemistry*, 331(3):1299–1307.

Samuel, O. O. (2018). Radiation exposure level in some granite quarry sites within ohimini and Gwer-East Local Government Areas of Benue State Nigeria. *Insights Med Phys*, 2(3):12.

Shahbazi-Gahrouei, D., Gholami, M., and Setayandeh, S. (2013). A review on natural background radiation. *Advanced Biomedical Research*, 2.

Sievert, R. and Failla, G. (1959). Recommendations of the international commission on radiological protection. *Health Physics (England)*, 2.

Slovic, P. (2012). The perception gap: Radiation and risk. *Bulletin of the Atomic Scientists*, 68(3):67–75.

Sudheer, K., Mohammad Koya, P., Prakash, A. J., et al. (2022). Evaluation of risk due to chronic low dose ionizing radiation exposure on the birth prevalence of congenital heart diseases (CHD) among the newborns from high-level natural radiation areas of Kerala coast, India. *Genes and Environment*, 44(1):1–10.

UNSCEAR (1993). United Nations Scientific Committee on the Effects of Atomic Radiation (UNSCEAR). Sources and Effects of Ionizing Radiation. United Nations sales publication E.94.IX.2. *United Nations, New York*.

UNSCEAR (2000). Effects of ionizing radiation. *United Nations, New York*, pages 453–487.

Yousef, H. A., Korany, K., Mira, H. I., et al. (2019). The annual effective dose of granite rock samples using alpha track detector. *Journal of Radiation Research and Applied Sciences*, 12(1):112–117.

RPE | Radiation Physics & Engineering
An International Peer-Reviewed Journal
Published by K.N. Toosi University of Technology
http://rpe.kntu.ac.ir
Research Article

Radiation Physics and Engineering 2023; 4(2):9–17

Studying the effect of backgrounds on the determination of radiative thermal neutron capture cross-section in the Neutron Powder Diffraction facility of the Tehran Research Reactor

Mahya Pazoki[a], Hamid Jafari[a,*], Zohreh Gholamzadeh[b]

[a] *Department of Radiation Application, Shahid Beheshti University, Tehran, Iran*
[b] *Reactor and Nuclear Safety, Nuclear Science and Technology Research Institute, Atomic Energy Organization of Iran, Tehran, Iran*

HIGHLIGHTS

- Flux distribution and its effect on the numerical value of the cross-section has been investigated.
- Neutron Powder Diffraction facility of Tehran Research Reactor were considered as a neutron source.
- Background effects on the calculated cross-sections were compared to the results of the EXFOR data library.
- Foils of gold, indium, and rhodium have been used as the samples irradiated by monochromatic neutron beam.

ABSTRACT

Neutron data and cross-sections are highly regarded and are essential for developing nuclear equipment such as advanced fission and fusion reactors, accelerators, neutron shielding, physics studies, etc. The neutron cross-section should preferably be measured using a single-energy neutron beam, although the presence of a background in research reactors can affect its accurate determination. The Neutron Powder Diffraction (NPD) facility of Tehran Research Reactor (TRR) has been taken into consideration for measuring the neutron cross-section based on its properties, including neutron monochromator and multiple collimators. In this work, radiative capture cross-sections of Au, In, and Rh materials have been calculated using TRR monochromatic beam. MCNPX is a Monte Carlo particle transport code that has been applied to simulate the measurement system of the neutron cross-section and calculate the reaction rates. The effect of the presence and absence of different sections of the background on the cross-section values was investigated and the results were compared with EXFOR data library for validation. According to the findings, neutron backgrounds can have varying impacts depending on factors such as sample material, the isotope resonance regions, neutron source spatial distribution, and neutron monochromatic energy. However, the presence of fast neutron background contributes to the most uncertainty in the cross section values while its removal produces an average discrepancy from experimental libraries of 7.16%. Also, removing the cold neutron background also causes a relative difference equal to 7.65%.

KEYWORDS

Cross-section
Neutron activation
TRR
MCNPX
Monochromatic beam

HISTORY

Received: 30 June 2022
Revised: 5 August 2022
Accepted: 18 August 2022
Published: Spring 2023

1 Introduction

The importance of neutron reaction cross-section data in the research and development of nuclear technologies is well known. Neutron cross-sections are the key quantities required to calculate neutron reactions taking place in reactors, shielding, transmutation process, detecting, space application, etc. (Huang et al., 1998; Rubbia et al., 1995). In this regard, the thermal neutron cross-section is the most important particularly for neutron absorber materials. These materials reduce exposure to neutron radiation. They are suitable for applications using neutron emitting sources: nuclear industry, cyclotron, medical accelerator, etc. (Lamarsh et al., 2001). Therefore in recent decades, preparing evaluated cross-section sets has become a discipline in itself and has been developing since the early 1960s. Moreover, neutron activation is one of the most frequently used techniques for neutron cross-section mea-

*Corresponding author: h_jafari@sbu.ac.ir

https://doi.org/10.22034/rpe.2022.349750.1094
https://dorl.net/dor/20.1001.1.26456397.2023.4.2.2.8

surements (El Abd et al., 2017). Neutron activation analysis (NAA) is a method based on the conversion of stable nuclei to radioactive ones by neutron capture. The essence of this method is about the measurement of released radiation from product radioactive nuclei. All of the stable elements are suitable for such a method but depending on the employed instrument, the radioactive product's half-lives should be considered.

A mono-energetic neutron source is the most suitable radiation source to measure the accurate value of material cross-sections. However, the total distribution of a neutron beam can be also applied in special circumstances. In neutron diffractometry facilities, single crystals are usually used as monochromators. Nevertheless, the presence of a radiation background in a monochromatic output beam requires the use of neutron filters to minimize higher-order contaminations. Several materials such as quartz (SiO_2) (Harvey et al., 1988), bismuth (Adib and Kilany, 2003), silicon (Brugger, 1976), lead (Adib et al., 2002), MgO (Adib et al., 2011), and sapphire (Al_2O_3) (Adib, 2005) have been suggested as the most successful filter materials. At high neutron energies, greater than about 1eV, the total neutron cross-section of each of the above-mentioned materials is in the range of a few barns. But at lower thermal energies, less than 0.1 eV, where much of the coherent Bragg scattering is forbidden the effective cross-section for single-crystal specimens is much reduced. Furthermore, iron, beryllium, BeO, and graphite are perhaps the most suitable materials when used as a cold neutron filter (Adib et al., 2004). Reserchers in the most of the national laboratories and several the commercial reactor designs have worked on cross-section measurement and many studies have been carried out by NAA procedure which some of them are stated in the following:

Celenk et al. (Celenk et al., 1991) measured the total thermal neutron macroscopic and microscopic cross-sections of V, Co, Cu, In, Dy and Au by using neutron self-absorption properties. 99% pure foils of elements with different thicknesses were utilized. In addition, Pu-Be was applied as a Maxwellian velocity distribution neutron source. The thermal neutron flux was about 10^4 $n.cm^{-2}.s^{-1}$ at the irradiation position. All foils of each element were irradiated with and without cadmium cover to determine the epithermal portion of the neutron spectrum. Areas of interest of gamma-photopeak, which were determined from the spectra from the foils, were plotted as foil thickness function. Then, a non-linear least-squares fitting method was applied and the total thermal neutron macroscopic and microscopic cross-section of the elements were obtained. The results were in good agreement with the compiled results by the libraries (Celenk et al., 1991).

Drozdowicz et al. (Drozdowicz, 1989) measured the macroscopic effective absorption cross-section of thermal neutrons in homogeneous and heterogeneous materials. Czubek's pulsed neutron method which is independent of the scattering properties of the sample was used to measure the absorption cross-section. The silicon samples in a cylindrical shape were surrounded by a moderator as only thermal neutrons were desired and covered with a cadmium cover. It has resulted that generally, the thermal-neutron absorption cross-section of any heterogeneous medium is always lower than a homogeneous one consisting of the same components. Very good agreement was observed between theoretical and experimental results of this work (Drozdowicz, 1989).

A method was developed by Elabd et al. (El Abd et al., 2017) for measuring both thermal neutron macroscopic absorption and scattering cross-sections for any sample in the form of powder or liquid. It is based on a wide beam of a Pu-Be neutron source and He-3 neutron detector assembly. Also, a semi-empirical model was proposed to fit the results. The model successfully fitted the results of both the solid and liquid standard samples (El Abd et al., 2017). Furthermore, Jacobson et al. (Jacobson, 1988) reviewed instrumentations and techniques for measuring thermal neutron capture cross-section in cased wellbores as an important formation evaluation tool for the petroleum industry. They discussed historical development, physical principles, applications, and recent developments in this field, and the importance of neutron macroscopic cross-section in log interpretation (Jacobson, 1988).

The behavior of thermal neutrons of 20 materials consisting of 12 elements, 3 alloys, and 5 chemicals was analyzed by Kobayashi et al. (Kobayashi et al., 1992) by applying the neutron radiography technique with the TRIGA-11 100 kW reactor. Scattering components were estimated and subtracted from the observed neutron intensities measured behind the slabs. A thermal neutron fluence of 2×10^9 $n.cm^{-2}$ was provided at the sample position. Measured values agreed within $\pm 20\%$ with predicted values (Kobayashi et al., 1992).

Due to the need for high accuracy in the cross-section measurement, it is recommended that the situation of the experiment be simulated using Monte Carlo radiation transport calculations before any practical work. Therefore, nuclear models and Monte Carlo based codes are also frequently used to estimate neutron-induced reaction cross-section in those calculations in which no experimental data are available besides neutron cross-section measurement (Cierjacks et al., 1994).

Hancerliogullari et al. (Hançerlioğullari et al., 2017) calculated total neutron macroscopic cross-sections based on transmission by Fluka Monte Carlo code and determining minerals, Sussexite and Vimsite, based on new shielding materials against fast neutron particles. The results of this investigation provided new information about the total macroscopic cross-sections, secondary radiation, neutron flow absorbed doses, and deposited energies by low energy neutron interaction of fast neutrons through materials including different amounts of boron and hydrogen atoms per unit volume. It is reported that all three minerals have been identified as a better neutron shield material than concrete (Hançerlioğullari et al., 2017).

The development of new materials in the nuclear industry and the necessity of their nuclear data sheet preparation motivates any advanced nuclear center to develop itself neutron cross-section laboratory. TRR has been equipped with a monochromatic neutron beam at the D beam tube which is supposed to be used for measuring the thermal neutron cross-section. In this work, radiative cap-

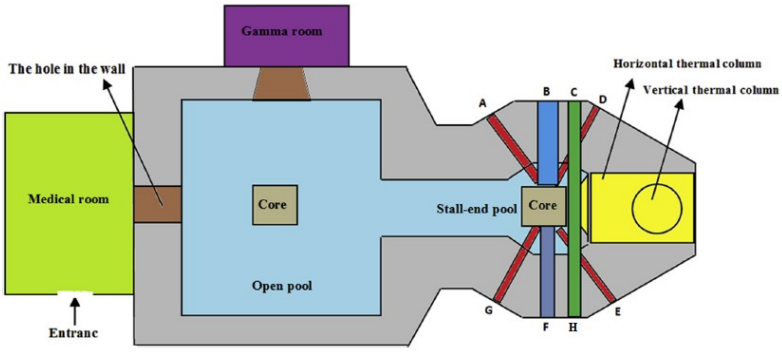

Figure 1: The schematic view of TRR pools and irradiation facilities (Gholamzadeh et al., 2018).

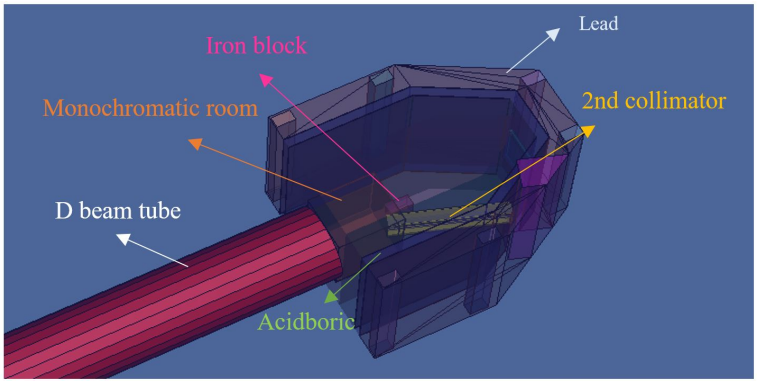

Figure 2: D beam tube arrangement of NPD facility of TRR (Gholamzadeh et al., 2018).

ture cross-sections of Au, In, and Rh materials have been calculated using TRR monochromatic beam. MCNPX is a Monte Carlo particle transport code that has been applied to simulate the measurement system of the neutron cross-section and calculate the reaction rates. Under different conditions, geometries and paricle fluxes, MCNPX will estimate the most possible reaction rate based on its experimental data stored in the ENDF library. Therefore, this code is not capable to calculate a microscopic cross-section of an unknown compound material. The neutron cross-section should preferably be measured using a single-energy neutron beam, but in the TRR NPD facility, the presence of neutron backgrounds in the neutron spectrum is observed. Then, the background effects on the calculated cross-sections have been compared to the experimentally measured data obtained from the IAEA-EXFOR library to evaluate the relative discrepancies and consequently determine the most useful neutron filtering of any background section.

2 Materials and Methods

2.1 Description of TRR

TRR is a pool-type light water nuclear reactor in that water acts as both coolant and moderator. Its fuel assemblies contain low-enriched uranium with a 20% concentration of U-235 in the form of U3O8Al alloy. The TRR pool contains two sections. One section called stall-end contains experimental facilities like beam tubes, rabbit system, and thermal column. The other section is the open end which is designed for bulk irradiation studies. Figure 1 shows a schematic view of the TRR pool and irradiation facilities. As it is shown there are seven beam tubes called A, B, C, D, E, F, and G. These beam tubes are composed of an aluminum chamber and stainless steel housing (Gholamzadeh et al., 2018; Dastjerdi et al., 2016).

2.2 Neutron Powder Diffraction Facility of TRR

D beam tube of TRR provides a monochromatic neutron beam and has been considered a neutron powder diffractometer (NPD) system. This NPD facility includes equipment such as a first collimator, monochromator, neutron and gamma shield, second collimator, sample table, third collimator, and neutron detectors. The first collimator is a rectangular soller-type collimator made of steel with dimensions of $7 \times 11 \times 120$ cm^3. A rectangular high ordered pyrolytic graphite (HOPG) monochromator is located along the beamline at the distance of 15 cm from the first collimator exit. The monochromatic beam enters the second collimator, which has dimensions of $6 \times 10 \times 60$ cm^3. Different thicknesses of the iron box, paraffin, boric acid powder, and lead surrounded the monochromator room to decrease the neutron and gamma doses. A shutter is placed at the end of the second collimator, which is closed when the beam is not required. The neutron wavelength of the beam can be varied in the range of 0.5 to 3 Å by different angles of placement and rotation of the HOPG crystal (65°, 75°, 80°, and 85°). Maximum neutron flux

on the sample table is obtained at 75°. A schematic of the NPD facility is shown in Fig. 2. In addition, neutron flux as a function of energy after the PG monochromator and at the sample position, which is located 120 cm away from the second collimator is shown in Fig. 3 (Gholamzadeh et al., 2018). The characteristics of this channel make it suitable for use in cross-section measurement.

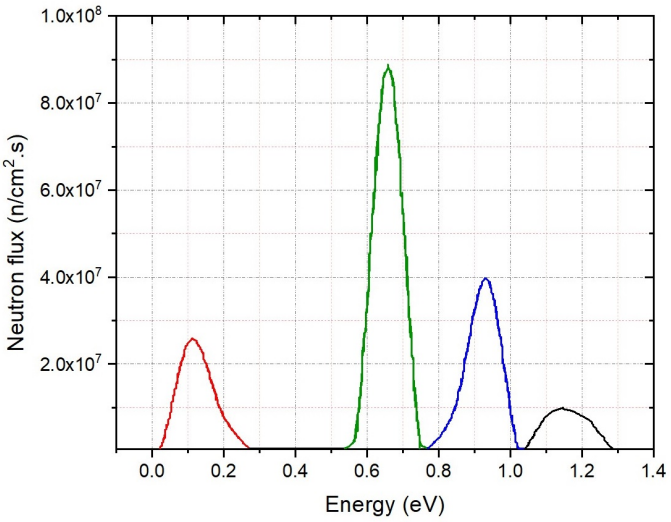

Figure 3: The neutron flux versus energy after the PG monochromator and at the sample position (Gholamzadeh et al., 2018).

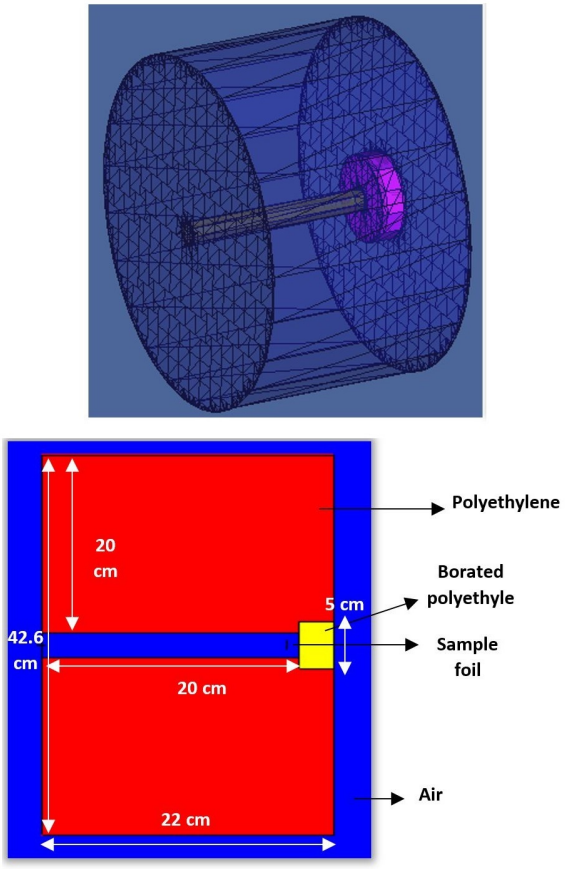

Figure 4: A view of MCNPX simulated geometry and sample position.

2.3 Computational approach

Among all of the capture reactions, (n, γ) reaction is the most important one for activation analysis. It is widely used according to its favorable cross-section, radioactive products with appropriate half-lives, and the ability to be run with any source of thermal neutrons (Steele and Meinke, 1962). To calculate the neutron cross-section by the Monte Carlo method, neutron flux/fluence and the reaction rate/density are required. Radiative capture microscopic cross-section of $\sigma_{(n,\gamma)}$ is obtained by dividing neutron reaction rate $(RR_{n,\gamma})$ by neutron total flux (Φ) and atomic density of the isotope (N) which is given by Eq. (1) (Pelowitz et al., 2011):

$$\sigma_{n,\gamma} = \frac{RR_{n,\gamma}}{\Phi\, N} \tag{1}$$

Partial cross-sections of isotopes have been measured during recent decades by experimental methods in numerous facilities. By using these experimental data stored in ENDF libraries, as well as information about neutron flux, MCNPX is capable to estimate the desired reaction rate. It should be noted that the MCNPX code cannot calculate the microscopic cross-section directly and this method is unusable for unknown isotopes without any data in the MCNPX library. In this study, different states of the neutron flux after the second collimator of TRR is considered as neutron source.

The MCNPX is a general-purpose Monte Carlo particle transport code that began in 1994 as an extension of MCNP4B and LAHET 2.8 in support of the accelerator production of tritium project (APT) (Pelowitz et al., 2011). The work envisioned a formal extension of MCNP to all particles and all energies; improvement of physics simulation models; extension of the neutron, proton, and photonuclear libraries to 150 MeV; and the formulation of new variance-reduction and data-analysis techniques. The program also included crosssection measurements, benchmark experiments, deterministic code development, and improvements in transmutation code and library tools through the CINDER90 project (Pelowitz et al., 2011, 2005).

The simulated geometry including the sample position at 3 cm away from the end of the D beam tube is shown in Fig. 4. This is a hollow cylinder with depicted dimensions and the sample foil ($1 \times 1 \times 0.001$ cm) is just located in front of a 5% borated-polyethylene as a sample holder. Here, indium (In), gold (Au), and rhodium (Rh) have been selected as the sample foils.

The track length estimator tally (F4) has been used to obtain neutron fluence. Due to the limitation in the optical physics of MCNPX, this is not able to consider monochromator crystal properties in the neutron spectra. Therefore, the monochromatic peaks have been added manually. The properties of these monochromatic peaks including their FWHM were calculated before using the Vitess code (Gholamzadeh et al., 2018).

The final obtained spectra were introduced as an input source for the microscopic cross-section calculation. Moreover, the tally multiplier (FM card) has been used to

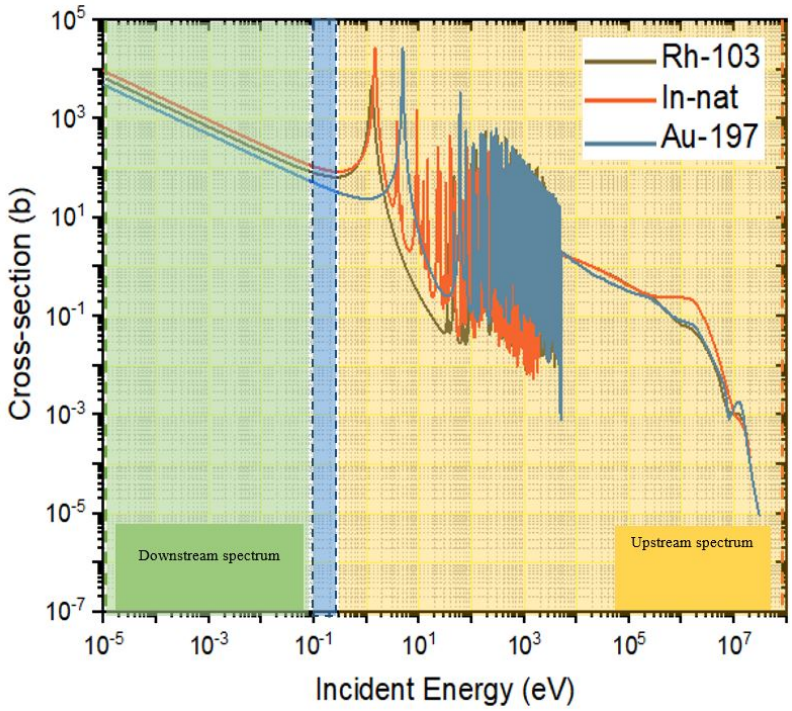

Figure 5: (n, γ) cross-section of three elements of Rh, In, and, Au by specifying monochromatic energy interval of TRR NPD facility and upstream and downstream energy ranges (ENDF, 2021).

compute the different neutron reaction rates as Eq. (2) (Pelowitz et al., 2005):

$$RR_i = C \int \Phi(E)\, \sigma_i(E)\, \mathrm{d}E \tag{2}$$

where $\sigma_i(E)$ is the microscopic cross-section of reaction, $\Phi(E)$ is the neutron flux as a function of energy, and C is the normalized coefficient which may be as atomic density [atoms.b^{-1}.cm^{-1}]. On this occasion, the reaction cross-sections are microscopic with units of barns. Assuming C as constant "1" results in a microscopic cross-section in which the number "-1" specifies a macroscopic scale. The number of histories has been considered so that statistical uncertainty is less than 1%.

As illustrated, the neutron cross-section should preferably be measured using a single-energy neutron beam, but in the TRR NPD facility, the presence of neutron backgrounds in the neutron spectrum is observed. The full spectrum contains a monochromatic peak depending on PG crystal orientation and the energies of 0.331 eV, 0.083 eV, 0.036 eV, 0.020 eV, and 0.013 eV have been considered in this regard. In addition, the effects of removing fast and cold neutron backgrounds on the enhancement of neutron cross-section calculation using the monochromatic beam have been investigated. These two other supposed conditions are the upstream spectrum which removes before the mono-energetic peak and the downstream spectrum which removes after the mono-energetic peak from the full spectrum. Of course, these conditions and the elimination of such species from parts of the spectrum are exaggerated and far from the experimental reality, but in this work, a general estimate has been made to determine the appropriate type of filtration. In this case, a suitable filter can be designed to measure the cross-section more accurately and in detail in the future.

The neutron capture cross-sections of (n, γ), corresponding to the three sample materials (In, Au, Rh), are shown in Fig. 5. The cross-section values have been extracted from the nuclear data library of ENDF/BVIII (ENDF, 2021). As seen, the monochromatic intervals (which are possible using the NPD system of TRR) have been depicted in blue color related to the neutron energy range of 0.020 to 0.331 eV. In addition, the upstream and downstream ranges have been shown by yellow and green color regions.

The results of (n, γ) microscopic cross-section calculation for the Au-197 sample which was irradiated by monochromatic neutron beams with a peak at 0.331, 0.083, 0.036, 0.020, and 0.013 eV are given in Tables 1 to 5, respectively. All the results are compared with the EXFOR -Experimental Nuclear Reaction Data- library, which contains an extensive compilation of experimental nuclear reaction data around the world. According to Table 1, the upstream spectrum with a relative difference of 13.07% in comparing the EXFOR data is the most appropriate spectrum to utilize, for which a cold neutron background should be removed. The result of employing the downstream region of the spectrum yielded 22.16%. Even though this error is higher than that of the upstream part, it is still preferable than employing the entire spectrum with an error of 26.43%. According to Figs. 5 and 6, the presence of a wide peak in the cold region of the spectrum, as well as a high neutron cross-section in this energy region can be a justification for the negative effect of the cold part of the spectrum on values.

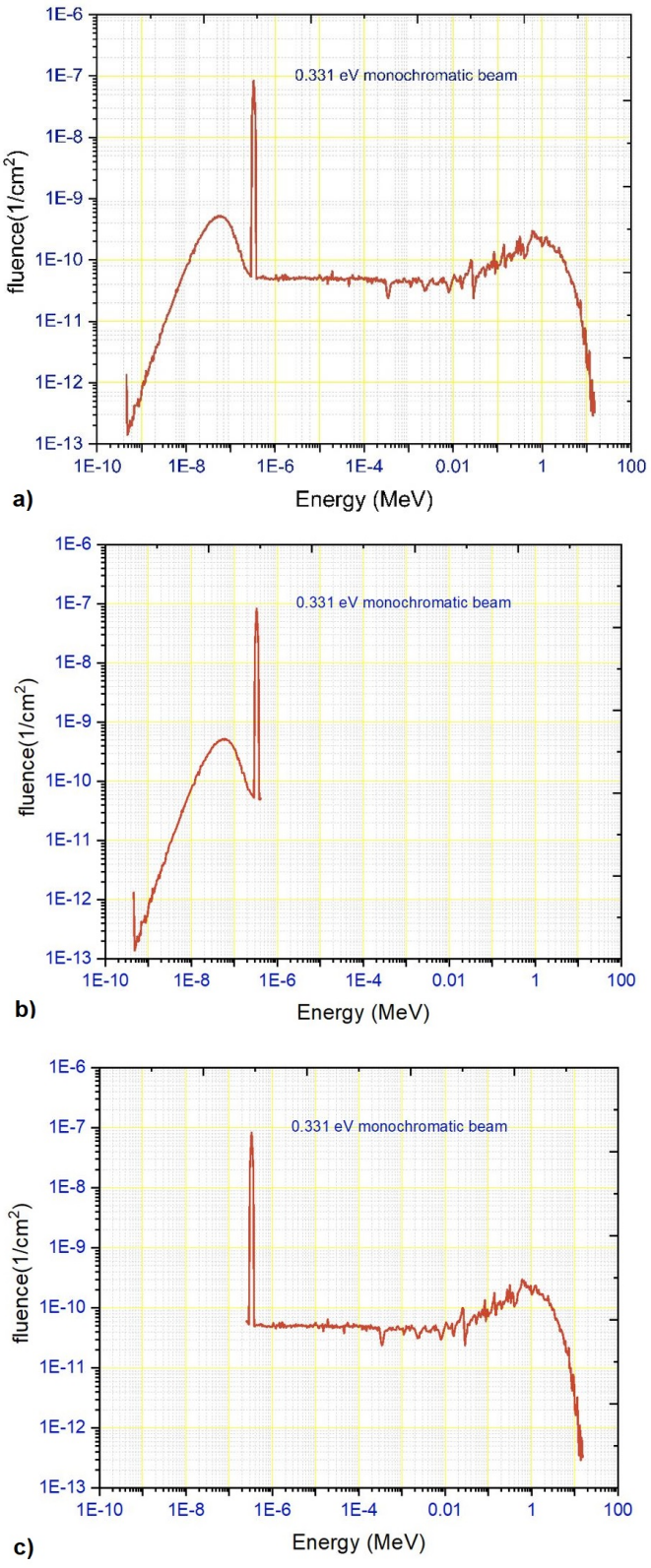

Figure 6: a) full neutron energy spectrum, b) downstream of mono-peak, c) upstream of mono-peak with the energy of 0.331 eV, at end of the D beam tube after the second collimator.

3 Results and Discussion

Figure 6 shows the neutron energy spectrum at the end of the D-beam tube after the second collimator which is obtained from previous studies (Gholamzadeh et al., 2018). The orientation of the PG crystal has been chosen so that its mono-energetic peak is at 0.331 eV. Moreover, the spectra with upstream and downstream sections of mono-peak are depicted. There is a monochromatic peak with a substantially higher flux than the background spectrum at the energy chosen by the crystal. However, there may be disturbances in the monochromatic spectrum's performance due to the existence of the backgrounds in the different range of energies.

Table 2 also reports the removal of cold neutrons useful for measuring neutron cross-section at the energy of 0.083 eV with a relative discrepancy of 1.43%. However, unlike the energy of 0.331 eV, using the downstream section (8.40%) rather than the entire spectrum (6.34%) is not recommended in this energy. These findings suggest that filtering contaminants do not always assist in bringing results closer to libraries.

On the other hand, the results for neutron beams with a monochromatic peak at 0.036, 0.020, and 0.013 eV demonstrate the lowest relative difference in comparing the downstream spectrum and the EXFOR data, which are equal to 3.15%, 0.73%, and 1.37% respectively. However, the use of the full spectrum is more likely for the monochromatic peak at 0.036 which denotes the favorable impact of background presence on the cross section's values. Indeed, it behaves in such a way that the neutron spectrum section before and after the mono-energetic peak neutralizes each other in the reaction rate. Additionally, using the upstream spectrum is not recommended due to the greater relative difference than the full energy spectrum in the mentioned cases.

The calculated neutron radiative capture cross-sections for natural indium including two isotopes of In-115 and In-113 by several spectra with mono-peak at 0.331 eV are summarized in Table 6. Here, the upstream spectrum has the lowest relative difference of 5.69% in comparing the EXFOR data. Therefore, removing of cold neutron background is suggested for this purpose which is the same as the gold sample at the monochromatic peak of 0.331 eV.

Investigation of the appropriate spectrum for calculating the microscopic neutron radiative capture cross-section of rhodium (Rh-103) shows the different results which are given in Table 7. According to the results, the upstream spectrum has a lower relative difference in comparing the EXFOR data which means cold filters are beneficial. also, the full spectrum itself seems to be better than the downstream section.

The calculated cross-sections for $^{197}\mathrm{Au}(n,\gamma)^{198}\mathrm{Au}$ in this study are compared to other experimental data from around the world in Fig. 7. According to this graph, in the case of utilizing the full output neutron spectrum of channel D of the TRR to measure the cross-section, the data will have a significant relative discrepancy in some energies compared to other values throughout the world. Self-absorption, scattering, characteristics of neutron spectrum and its flux, and other factors can account for the differences in this comparison. At energies of 0.013, 0.020, and 0.331 eV the discrepancy in results is more obvious than at

Table 1: The calculation of microscopic cross-section for Au-197 sample by monochromatic neutron beam with the peak at 0.331 eV.

Neutron beam	Fluence at sample (cm^{-2})	(n,γ) reaction density ($atoms.cm^{-3}$)	Microscopic cross-section (b)	EXFOR library (b)	Relative difference with EXFOR (%)
Mono-energetic	8.62×10^{-2}	2.82	32.8	30.7	6.74
Full spectrum	8.66×10^{-2}	3.36	38.8		26.43
Upstream of mono-peak	8.65×10^{-2}	3.00	34.7		13.07
Downstream of mono-peak	8.62×10^{-2}	3.23	37.5		22.16

Table 2: The calculation of microscopic cross-section for Au-197 sample by monochromatic neutron beam with the peak at 0.083 eV.

Neutron beam	Fluence at sample (cm^{-2})	(n,γ) reaction density ($atoms.cm^{-3}$)	Microscopic cross-section (b)	EXFOR library (b)	Relative difference with EXFOR (%)
Mono-energetic	8.66×10^{-2}	4.96	57.26	55.6	2.99
Full spectrum	8.69×10^{-2}	5.14	59.13		6.34
Upstream of mono-peak	8.69×10^{-2}	4.90	56.39		1.43
Downstream of mono-peak	8.66×10^{-2}	5.22	60.27		8.40

Table 3: The calculation of microscopic cross-section for Au-197 sample by monochromatic neutron beam with the peak at 0.036 eV.

Neutron beam	Fluence at sample (cm^{-2})	(n,γ) reaction density ($atoms.cm^{-3}$)	Microscopic cross-section (b)	EXFOR library (b)	Relative difference with EXFOR (%)
Mono-energetic	8.72×10^{-2}	7.27	83.39	82.8	0.72
Full spectrum	8.74×10^{-2}	7.04	80.57		2.69
Upstream of mono-peak	8.74×10^{-2}	6.94	79.44		4.06
Downstream of mono-peak	8.72×10^{-2}	7.45	85.41		3.15

Table 4: The calculation of microscopic cross-section for Au-197 sample by monochromatic neutron beam with the peak at 0.020 eV.

Neutron beam	Fluence at sample (cm^{-2})	(n,γ) reaction density ($atoms.cm^{-3}$)	Microscopic cross-section (b)	EXFOR library (b)	Relative difference with EXFOR (%)
Mono-energetic	8.78×10^{-2}	9.65	109.94	110.9	0.86
Full spectrum	8.80×10^{-2}	9.01	102.43		7.64
Upstream of mono-peak	8.80×10^{-2}	8.96	101.82		8.19
Downstream of mono-peak	8.78×10^{-2}	9.81	111.71		0.73

Table 5: The calculation of microscopic cross-section for Au-197 sample by monochromatic neutron beam with the peak at 0.013 eV.

Neutron beam	Fluence at sample (cm^{-2})	(n,γ) reaction density ($atoms.cm^{-3}$)	Microscopic cross-section (b)	EXFOR library (b)	Relative difference with EXFOR (%)
Mono-energetic	8.82×10^{-2}	11.78	133.45	137.1	2.66
Full spectrum	8.84×10^{-2}	10.74	121.57		11.33
Upstream of mono-peak	8.83×10^{-2}	10.72	121.30		11.53
Downstream of mono-peak	8.83×10^{-2}	11.94	135.22		1.37

Table 6: The calculation of microscopic cross-section for natural In by monochromatic neutron beam with the peak at 0.331 eV.

Neutron beam	Fluence at sample (cm^{-2})	(n,γ) reaction density ($atoms.cm^{-3}$)	Microscopic cross-section (b)	EXFOR library (b)	Relative difference with EXFOR (%)
Mono-energetic	8.61×10^{-2}	7.67	89.19	86.29	3.36
Full spectrum	8.64×10^{-2}	8.34	96.51		11.85
Upstream of mono-peak	8.64×10^{-2}	7.88	91.20		5.69
Downstream of mono-peak	8.61×10^{-2}	8.27	96.02		11.28

Table 7: The calculation of microscopic cross-section for Rh-103 sample by monochromatic neutron beam with the peak at 0.331 eV.

Neutron beam	Fluence at sample (cm^{-2})	(n,γ) reaction density ($atoms.cm^{-3}$)	Microscopic cross-section (b)	EXFOR library (b)	Relative difference with EXFOR (%)
Mono-energetic	8.60×10^{-2}	6.20	72.12	67.85	6.30
Full spectrum	8.64×10^{-2}	6.29	72.81		7.31
Upstream of mono-peak	8.63×10^{-2}	5.91	68.50		0.96
Downstream of mono-peak	8.60×10^{-2}	6.59	76.63		12.95

other energies, and there is a significant gap between data from this work and the experimental library. Therefore, different parts of the full neutron spectrum were used as sources so that it may be possible to measure more accurate cross-section values by determining neutron filtration in the NPD facility.

The cross-sections derived using the downstream spectrum (removing fast neutron background) are given in Fig. 8 compared to EXFOR data. We can notice the good influence of removing fast neutron background on the data findings by comparing this graph to Fig. 8. However, the data will still be far from the desired outcomes at higher energies, which removing sold background in this region is recommended.

4 Conclusions

The neutron cross-section has been constantly studied to advance neutron research and applications. The development of radiation centers is significantly influenced by the precision of a material's neutron cross-section. In addition, the computational procedures provide us to evaluate a nuclear facility as completely safe without high-cost expenses on such systems' manufacturing before their optimization. NPD facility of the TRR is equipped with PG monochromator, suitable for measuring neutron cross-section. The output neutron spectrum of this beam has a variety of neutron backgrounds in addition to the monochromatic peak. In this work, the impact of different region of the neutron background being either present or absent on the (n,γ) cross sections of materials has been examined and also the weight of such backgrounds in the measurement precision has been evaluated. MCNPX, a Monte Carlo-based code has been used to simulate the TRR cross-section measurement system and to calculate the (n,γ) reaction rates of Au, In, and Rh sample materials. This code provides reaction rates using the stored cross-sections of the code libraries and it cannot determine the cross-section on its own. These reaction rates could differ proportionally to the system's circumstances and characteristics, including geometry, neutron flux, etc. According to the results, the impact of neutron background for determining the (n,γ) cross-section of different isotopes might vary. However, removing fast neutron background is often recommended which results in a mean relative difference of 7.16% in comparing EXFOR data for Au sample only. Removing the cold neutron background from the spectrum is also useful in providing differences of less than 15% and is preferable in some cases, while the average difference for Au samples in all energies is 7.65%.

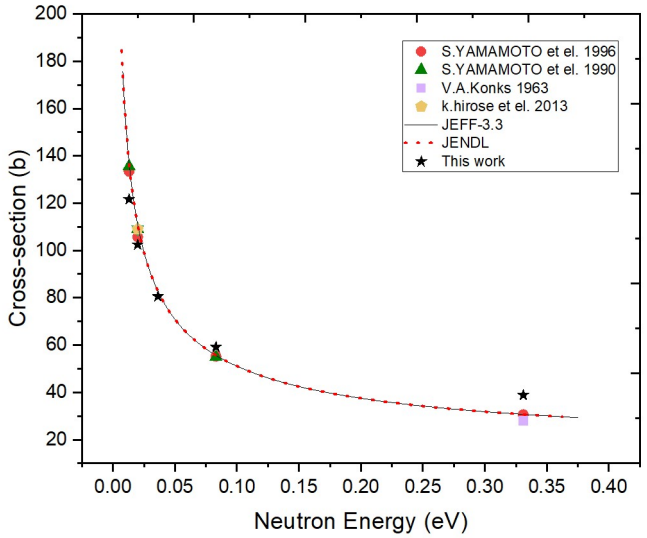

Figure 7: The comparison of $^{197}Au(n,\gamma)^{198}Au$ cross-section calculated by full neutron spectrum of channel D of the TRR with other experimental data in the world.

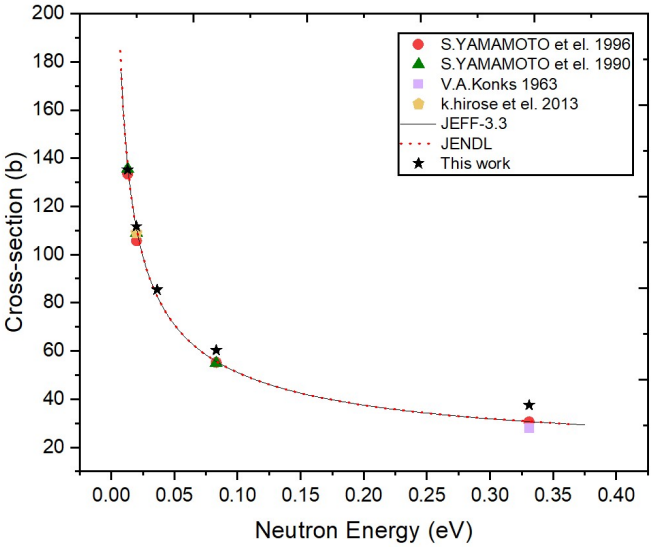

Figure 8: The comparison of $^{197}Au(n,\gamma)^{198}Au$ cross-section calculated downstream of mono-energetic neutron beam from channel D of the TRR with other experimental data in the world.

For this reason, it can be examined in the upcoming works using simulation codes to design and provide an appropriate neutron filter more accurately for the NPD facility to measure the thermal neutron cross-section. Sapphire fast neutron filter due to the references has lots of

the desired characters to be taken under consideration for NPD facility.

Consequently, it is recommended that the neutron cross-section be simulated and compared to single-energy before any measurement for each material. It causes to guide the system operator to determine which neutron filter may be required to enhance the measurement accuracy in the presence of the neutron backgrounds. The results of this study will be employed in the future for both benchmarking experimental data and designing a crystal filter to optimize the neutron spectrum of the TRR NPD facility for the cross-section measurement.

Conflict of Interest

The authors declare no potential conflict of interest regarding the publication of this work.

Copyright

References

Adib, M. (2005). Cross-section of single-crystal materials used as thermal neutron filters.

Adib, M., Habib, N., Bashter, I., et al. (2011). Mgo single-crystal as an efficient thermal neutron filter. *Annals of Nuclear Energy*, 38(12):2673–2679.

Adib, M., Habib, N., Kilany, M., et al. (2004). Neutron transmission through crystalline Fe.

Adib, M. and Kilany, M. (2003). On the use of bismuth as a neutron filter. *Radiation Physics and Chemistry*, 66(2):81–88.

Adib, M., Naguib, K., Ashry, A., et al. (2002). On the use of lead as a neutron filter. *Annals of Nuclear Energy*, 29(9):1119–1130.

Brugger, R. M. (1976). A single crystal silicon thermal neutron filter. *Nuclear Instruments and Methods*, 135(2):289–291.

Celenk, I., Demirel, H., and Özmen, A. (1991). Measurement of macroscopic and microscopic thermal neutron cross sections of V, Co, Cu, In, Dy and Au using neutron self-absorption properties. *Journal of Radioanalytical and Nuclear Chemistry*, 148(2):393–401.

Cierjacks, S., Shibata, K., and Issy-les Moulineaux, F. (1994). *Blind Intercomparison of Nuclear Models for Predicting Charged Particle Emission, NEA/NSC-DOC93-4*. Nuclear Energy Agency, OECD.

Dastjerdi, M. C., Khalafi, H., Kasesaz, Y., et al. (2016). Design, construction and characterization of a new neutron beam for neutron radiography at the Tehran Research Reactor. *Nuclear Instruments and Methods in Physics Research Section A: Accelerators, Spectrometers, Detectors and Associated Equipment*, 818:1–8.

Drozdowicz, K. (1989). Energy-dependent scattering cross section of plexiglass for thermal neutrons. Technical report, Chalmers Univ. of Tech.

El Abd, A., Taha, G., and Ellithi, A. (2017). A method for measuring macroscopic cross-sections for thermal neutrons. *Applied Radiation and Isotopes*, 128:318–327.

ENDF (2021). ENDF: Evaluated Nuclear Data File, https://www-nds.iaea.org/exfor/endf.htm#1. Technical report.

Gholamzadeh, Z., Bavarnegin, E., Rachti, M. L., et al. (2018). Modeling of neutron diffractometry facility of Tehran Research Reactor using Vitess 3.3 a and MCNPX codes. *Nuclear Engineering and Technology*, 50(1):151–158.

Hançerlioğullari, A., KORKUT, T., and MADEE, Y. G. A. (2017). The Neutron Macroscopic Cross Sections Calculation of Some Minerals by Using FLUKA Monte Carlo Method. *The Online Journal of Science and Technology-July*, 7(3).

Harvey, J., MOOK, H., HILL, N., et al. (1988). Nuclear data for science and technology.

Huang, X., Lu, H., Zhao, W., et al. (1998). Neutron activation cross section measurements and evaluations in CIAE. Technical report, International Atomic Energy Agency.

Jacobson, L. A. (1988). Macroscopic thermal neutron capture cross section measurements. *IEEE Transactions on Nuclear Science*, 35(1):817–821.

Kobayashi, H., Wakao, H., Ikeda, Y., et al. (1992). Macroscopic cross section measurements and defect detection in materials using neutron radiography technique. *Journal of Nuclear Science and Technology*, 29(11):1045–1053.

Lamarsh, J. R., Baratta, A. J., et al. (2001). *Introduction to nuclear engineering*, volume 3. Prentice hall Upper Saddle River, NJ.

Pelowitz, D. B. et al. (2005). MCNPX^{TM} user's manual. *Los Alamos National Laboratory, Los Alamos*, 5:369.

Pelowitz, D. B. et al. (2011). MCNPX^{TM} user's manual. *Los Alamos National Laboratory, Los Alamos*, 5:369.

Rubbia, C., Roche, C., Rubio, J. A., et al. (1995). Conceptual design of a fast neutron operated high power energy amplifier. Technical report.

Steele, E. L. and Meinke, W. W. (1962). Determination of rhodium by thermal neutron activation analysis using g-ray spectrometry. *Analytica Chimica Acta*, 26:269–274.

RPE | Radiation Physics & Engineering
An International Peer-Reviewed Journal
Published by K.N. Toosi University of Technology
http://rpe.kntu.ac.ir
Research Article

Radiation Physics and Engineering 2023; 4(2):19–24

Effect of marker material on the dosimetric parameters of I-125 source (model 6711): Monte Carlo simulation

Payvand Taherparvar*, Ali Azizi Ganjgah

Department of Physics, Faculty of Science, University of Guilan, Postal Code 4193833697, Rasht, Iran

HIGHLIGHTS

- Validation of the I-125 (model 6711) seed according to the TG-43U1 recommendation by GEANT4.
- Simulation of new seeds containing Ag+Al_2O_3 markers with different ratio of Ag and Al_2O_3.
- Similarity between calculated dosimetric parameters of the I-125 seed (6711) and the new sources.

ABSTRACT

Low energy I-125- seeds are considered as a common source in different brachytherapy techniques for treatment of different cancers. In this study, at first, we simulated and validated I-125 (model 6711) seed according to the TG-43U1 recommendation, by GEANT4 Monte Carlo toolkit. Moreover, we simulated new seeds containing cylindrical Ag+Al_2O_3 markers with different ratio of Ag and Al_2O_3 in the final composition of the marker and compared the radial dose functions and anisotropy functions of the sources. For validation and evaluation purposes, the radial dose function and anisotropy function were calculated at various distances from the center of the different simulated sources. The source validation results show that GEANT4 Monte Carlo toolkit produces accurate results for dosimetric parameters of the I-125 seed by choosing the appropriate physics list. On the other hand, results show a similarity between calculated dosimetric parameters of the I-125 seed (6711) and other sources, with a percentage difference of about 5%.

KEYWORDS

Brachytherapy
Dosimetric parameters
I-125
GEANT4

HISTORY

Received: 22 April 2022
Revised: 19 August 2022
Accepted: 26 August 2022
Published: Spring 2023

1 Introduction

Brachytherapy is a type of internal radiation therapy, in which an encapsulated radiation source is positioned within or close to a region inside the patient's body to maximize doses to cancer cells while minimizing damage to normal tissues (Russell and Blasko, 1993). Although in some cases beta emitters are used in this method (Rajabi and Taherparvar, 2019), the low-energy photon emitting radioisotopes such as I-125, Pd-103, and Cs-131 are widely used in brachytherapy for treatment of different cancer, such as prostate cancer, eye malignant tumors, cervix cancers, and malignant brain tumors (Rajabi and Taherparvar, 2019; Ghiassi-Nejad et al., 2001; Taherparvar and Fardi, 2022, 2021). I-125 is the most commonly used form of local treatment brachytherapy with a half-life of 59.431 days. It decays by electron capture to the excited state of Te-125 (Ghiassi-Nejad et al., 2001). According to the American Association of Physicists in Medicine (AAPM), determination of dosimetric parameters of brachytherapy sources is essential. These dosimetric parameters consist of dose rate constant (Λ), radial dose function ($g(r)$), anisotropy function ($F(r,\theta)$). Today, different Monte Carlo simulation codes, such as GEANT4, MCNP, GATE, FLUKA, etc., have been used for determination of dosimetric parameters of the brachytherapy sources. In this study, we simulated I-125 seed model 6711 by GEANT4 Monte Carlo toolkit. The sources have been validated by comparing our simulation results with with available data in the literatures, according to TG-43U1 protocol (Meigooni, 1995). In the I-125 seed models, the materials and geometry of the active core varies from company to company. Since Ag+Al_2O_3 rod is a good carrier for an Iodine radioisotope and the distribution of the

*Corresponding author: p.taherparvar@guilan.ac.ir

https://doi.org/10.22034/rpe.2022.338851.1079
https://dorl.net/dor/20.1001.1.26456397.2023.4.2.3.9

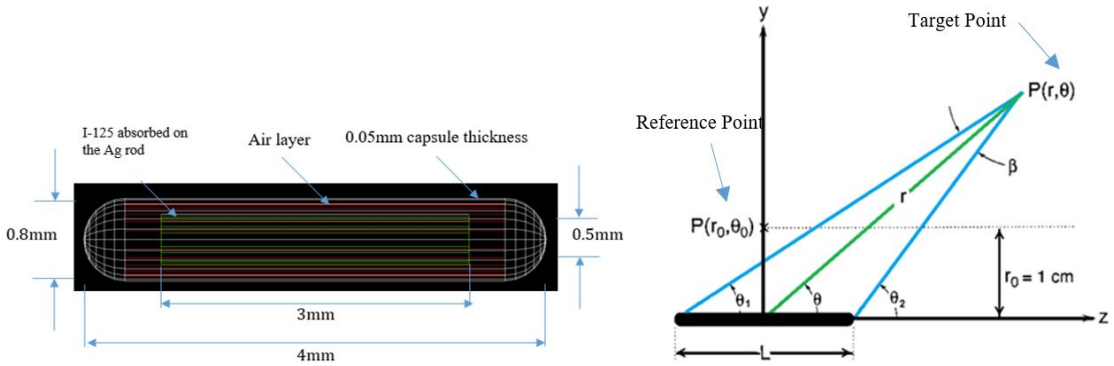

Figure 1: I-125 seed in GEANT4 (a), the geometry conventions for dose rate calculations (b), r: denotes the distance in centimeters from the center of the source, θ_1 (θ_2): denotes the polar angle between the point of interest and the beginning (end) of the source.

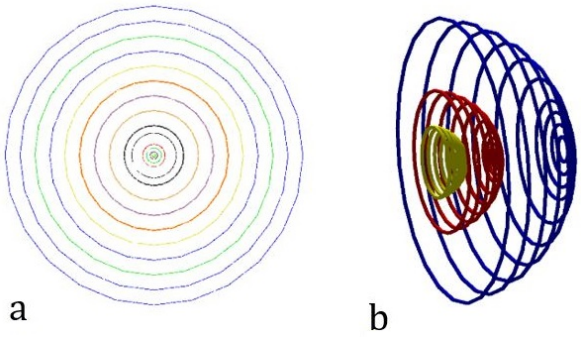

Figure 2: Geometric system used to calculate $g(r)$ (a) and $F(r,\theta)$ (b) in the GEANT4.

source on it is relatively uniform, the Ag+Al_2O_3 has been suggested as a good compound for seed marker (Babaheidari and Shamsaee, 2014). Hereby, in this study by validation of the I-125 (model 6711) seed according to the TG-43U1 recommendation by GEANT4 toolkit, we evaluate the effect of Ag+Al_2O_3 markers on the dosimetric parameters of the new source. Furthermore, effect of different ratio of Ag and Al_2O_3 in the composition of the marker material were evaluated by calculation of the radial dose functions and anisotropy functions of the sources.

2 Materials and Methods

2.1 Source characteristics

At first, we simulated I-125 (model 6711) seed (named Seed 1), as shown in Fig. 1. The seed consists of a silver cylindrical marker with 0.025 cm radius and 3.2 mm length. I-125 radioisotope is uniformly deposited on the silver marker with the 1 m thickness. The marker is encapsulated within a titanium tube of 0.47 cm in length, 0.08 cm diameter, 0.006 cm thickness on top and bottom, and 0.4 mm radius at both semispherical ends. The space between the titanium and marker was filled with air. In separate simulations, Ag was replaced with Ag+ Al_2O_3 markers with different percentages consist of: 15%Ag + 85% Al_2O_3 (Seed 2), 25%Ag + 75% Al_2O_3 (Seed 3), and 35%Ag + 65% Al_2O_3 (Seed 4). All simulations with theses seeds were repeated and results were compared. Simulations were performed by using GEANT4 Monte Carlo toolkit to determine the dosimetric parameters of the seeds in the center of a water phantom. The photon energy spectrum used in the simulations for all seeds are shown in Table 1 (according to TG-43U1 protocol). The radial dose functions and anisotropy functions were calculated by calculation of dose deposition in the specific scoring rings, according to the TG-43U1, as shown in Fig. 2 (Ghiassi-Nejad et al., 2001).

Table 1: Photon spectrum of I-125 (Taherparvar and Fardi, 2021).

Energy (keV)	Intensity
3.77000	0.150
27.2017	0.397
27.4723	0.741
31.0000	0.257
35.4919	0.067

2.2 Dosimetric parameters

According to the AAMP recommendations (Fardi and Taherparvar, 2019), the dose-rate at point (r,θ) (as can be seen in Fig. 1-b) could be acquired as follows:

$$\dot{D}(r,\theta) = S_k.\Lambda.\frac{G_1(r,\theta)}{G_1(r_0,\theta_0)}.G_1(r).F(r,\theta) \qquad (1)$$

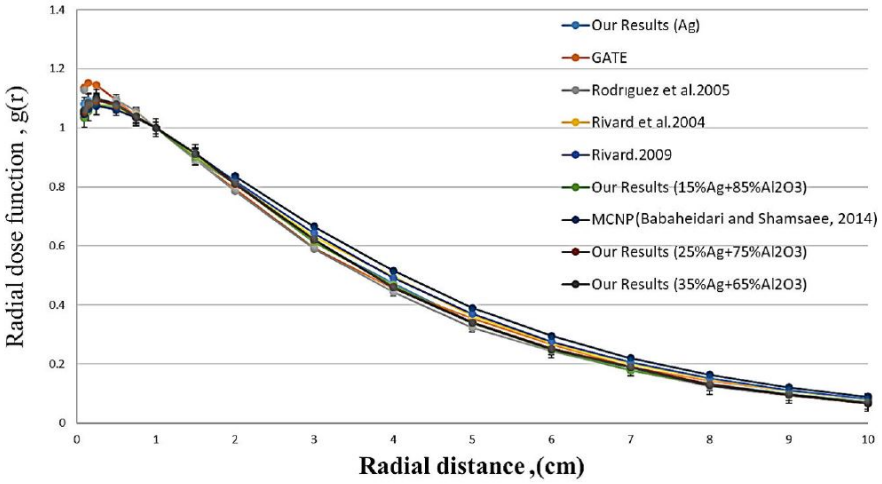

Figure 3: Comparison of the radial dose function obtained by GEANT4 simulation results for I-125 with Ag and different combinations of Ag+Al_2O_3 with different percentages markers and other experimental and theoretical results.

where $\dot{D}(r,\theta)$ is the dose rate at the distance r (cm) from the capsule center, θ is the polar angle defining the P point, S_k is the air-kerma strength, Λ is the dose rate constant, $G(r,\theta)$ and $G(r_0,\theta_0)$ are the geometry factors around the source and reference point, respectively. The dose rate constant (Λ) is equal to the dose rate at the reference point ($r_0 = 1$ cm, $\theta_0 = \frac{\pi}{2}$) divided by source air kerma strength.

$$\Lambda = \frac{\dot{D}(r_0,\theta_0)}{S_k} \tag{2}$$

To calculate the radial dose function, $g(r)$, rings with 0.4 mm thicknesses were located at 0.1 to 10 cm distance from the source along its transverse axis. Then, $g(r)$ was calculated as follows:

$$g(r) = \frac{\dot{D}(r,\theta_0)\, G(r_0,\theta_0)}{\dot{D}(r_0,\theta_0)\, G(r,\theta_0)} \tag{3}$$

The geometric systems used to calculate $g(r)$ are shown in Fig. 2-a. The anisotropy function of I-125 source was calculated (according to Eq. (4)) at distances of 0.5 ,1 and 5 cm from the source center using rings with 0.4 mm thicknesses at different angles. The geometric systems used to calculate $F(r,\theta)$ are shown in Fig. 2-b.

$$F(r,\theta) = \frac{\dot{D}(r,\theta)\, G(r,\theta_0)}{\dot{D}(r,\theta_0)\, G(r,\theta)} \tag{4}$$

2.3 Monte Carlo simulation

Simulations were performed using GEANT4 version 10.5, Monte Carlo toolkit to determine the dosimetric parameters of seeds 1 to 4 in a 20 cm radius spherical water phantom according to the recommendation of the AAPM. GEANT4 (derived from Geometry and Tracking) is written in the C++ programming language with extensive libraries, which contain a differential cross-section of different particles in different areas in the energy range of several eV to PeV.

At first, I-125 (model 6711) seed (Seed 1) was located in the center of the phantom and radial dose function and 2D anisotropy function were calculated. According to TG-43 (U1) recommendations, reference dosimetry media was considered degassed water with a mass density of 0.998 g.cm^{-3}. On the other hand, since Ag+Al_2O_3 rod is a good carrier for an Iodine radioisotope and the distribution of the source on it is relatively uniform, the effects of the marker materials consist of different percentages different combinations of Ag and Al_2O_3 (with different ratio of Ag 15%, 25%, and 35%) on the radial dose function and 2D anisotropy function were investigated in this study.

We used G4PSEnergyDeposit and G4PSDoseDeposit classes, which are the standard classes in GEANT4 to llcluclac energy and dose deposition in the predefined rings. The G4EmStandardPhysics_option3 was used to simulate different physical processes such as elastic scattering, ionization, electronic excitation, and lna vibrational excitation for photons without using any reduction techniques. The number of primary particles included 5×10^8 and the mean statistical uncertainty for the dose calculations were about 2%.

3 Results and Discussion

3.1 Radial dose function

Values of the radial dose function for source in the water phantom for four simulated seeds, which were calculated for distances from 0.1 to 10 cm from the source center, are indicated in Fig. 3 and Table 2. These results. The comparison between the theoretical and experimental radial dose function show that the mean difference between Seed1 and those of Fardi et al. (Taherparvar and Fardi, 2021), Rodrguez (Rodríguez et al., 2005), Rivard et al. (Rivard et al., 2004), Rivard (Rivard, 2009), and Eslami et al. (by MCNP) (Babaheidari and Shamsaee, 2014) were about 4%, 3%, 4.6%, 5.8%, and 5%, respectively, which show a good agreement. On the other hand, the mean difference between Seed2, Seed3, and Seed4 results and

Table 2: Radial dose function of I-125 seed sources obtained from different study.

Radial distance (cm)	Our Results (Seed 1)	GATE (Ag)	(Rodríguez et al., 2005) (Ag)	(Rivard et al., 2004) (Ag)	(Rivard, 2009) (Ag)	Our Results (Seed2)	MCNP ($Ag+Al_2O_3$)	Our Results (Seed3)	Our Results (Seed4)
0.1	1.080	1.136	1.1278	1.055	1.036	1.033	1.046	1.054	1.061
0.15	1.092	1.152	-	1.078	1.057	1.055	1.065	1.078	1.085
0.25	1.095	1.145	-	1.082	1.074	1.076	1.075	1.092	1.1
0.5	1.073	1.092	1.096	1.071	1.066	1.073	1.061	1.076	1.081
0.75	1.036	1.041	1.0575	1.042	-	1.036	1.035	1.038	1.04
1	1	1	1	1	1	1	1	1	1
1.5	0.892	0.892	0.8923	0.908	0.913	0.90	-	0.91	0.912
2	0.813	0.794	0.7862	0.814	0.82	0.810	0.837	0.81	0.813
3	0.613	0.594	0.5899	0.632	0.643	0.614	0.666	0.622	0.623
4	0.473	0.456	0.4443	0.496	0.491	0.467	0.516	0.461	0.458
5	0.340	0.355	0.3224	0.364	0.37	0.337	0.39	0.341	0.338
6	0.250	0.267	0.2443	0.27	0.276	0.248	0.295	0.252	0.25
7	0.179	0.191	0.1792	0.199	0.205	0.178	0.22	0.189	0.19
8	0.134	0.143	0.1244	0.149	0.151	0.129	0.164	0.131	0.128
9	0.097	0.108	0.0937	0.109	0.111	0.097	0.121	0.095	0.097
10	0.071	0.079	0.0702	0.083	0.082	0.071	0.089	0.067	0.069

Table 3: Anisotropy function calculated for the I-125 seed for 0.5 cm, 1 cm, and 5 cm.

Angle (θ)	5	10	15	20	30	40	50	60	70	80
$F(0.5,\theta)$; GATE (Ag)	0.353	0.438	0.557	0.658	0.838	0.945	1.007	1.027	1.039	0.998
$F(0.5,\theta)$; GEANT (Seed1)	0.366	0.448	0.571	0.689	0.846	0.959	1.014	1.026	1.038	0.994
$F(0.5,\theta)$; GEANT (Seed2)	0.352	0.420	0.527	0.633	0.794	0.896	0.958	0.983	1.006	0.992
$F(0.5,\theta)$; GEANT (Seed3)	0.348	0.425	0.538	0.651	0.816	0.919	0.973	0.999	1.02	1.002
$F(0.5,\theta)$; GEANT (Seed4)	0.349	0.427	0.54	0.66	0.828	0.927	0.978	1.003	1.02	1.018
$F(1,\theta)$; GATE (Ag)	0.478	0.502	0.611	0.689	0.825	0.919	0.985	1.004	1.022	1.023
$F(1,\theta)$; GEANT (Seed1)	0.451	0.534	0.632	0.721	0.837	0.931	0.992	1.025	1.040	1.0251
$F(1,\theta)$; GEANT (Seed2)	0.425	0.495	0.582	0.657	0.786	0.885	0.945	0.985	1.012	1.011
$F(1,\theta)$; GEANT (Seed3)	0.449	0.501	0.594	0.679	0.802	0.895	0.957	0.99	1.019	1.035
$F(1,\theta)$; GEANT (Seed4)	0.453	0.501	0.605	0.634	0.814	0.904	0.967	0.997	1.018	1.033
$F(5,\theta)$; GATE (Ag)	0.684	0.720	0.756	0.823	0.841	0.905	0.962	0.948	0.998	0.952
$F(5,\theta)$; GEANT (Seed1)	0.593	0.664	0.761	0.821	0.870	0.953	1.022	1.002	1.027	0.979
$F(5,\theta)$; GEANT (Seed2)	0.535	0.643	0.712	0.760	0.837	0.914	0.981	1.004	1.033	0.986
$F(5,\theta)$; GEANT (Seed3)	0.620	0.626	0.703	0.789	0.827	0.928	0.948	1.014	1.020	0.973
$F(5,\theta)$; GEANT (Seed4)	0.63	0.646	0.706	0.797	0.842	0.934	0.957	1.008	1.005	0.986

I-125 seed (Seed1) were about 1.2%, 1.7%, and 4.9%, respectively.

3.2 Anisotropy function

The anisotropy function of the seeds were calculated at distances of 0.5, 1, and 5 cm from the source center using rings with 0.4 mm thicknesses at different angles relative to the source axis (Fig. 2-b). Table 3 shows the calculated anisotropy function values at different radial distances for angles between 5° and 80°, respectively. Also, a comparison of the anisotropy function of the four simulated sources and Fardi et al. (Taherparvar and Fardi, 2021) results are shown in Fig. 4, at radial distances of 0.5 cm (Fig. 4-a), 1 cm (Fig. 4-b), and 5 cm (Fig. 4-c). The mean difference between GEANT4 results and those of GATE for I-125 seed (6711) is about 1.7%, 2.7%, and 4.8% at radial distances of 0.5 cm, 1 cm, and 5 cm distance, respectively. A comparison of the calculation with the obtained results shows a good agreement between our simulation results and other report.

Furthermore, the average difference between results of the anisotropy function of the I-125 seed with Ag marker and I-125 seed with 15%Ag+85%Al_2O_3 marker (Seed2) in our simulation is about 5.2%, 5.3%, and 3.9% at 0.5 cm, 1 cm, and 5 cm distances, respectively. The mean difference between Seed2 and Seed1 is about 1.8%, 1.9% and 3.5% at radial distances of 0.5 cm, 1cm, and 5 cm distance, respectively. In addition to, the mean difference between Seed3 and Seed1 is about 2.3%, 2.8% and 3.3% at radial distances of 0.5 cm, 1 cm, and 5 cm distance, respectively.

4 Discussion and conclusion

Dosimetric parameters of the I-125 (model 6711) brachytherapy source have been investigated according to the TG-43U1 recommendation by using GEANT4 toolkit. Our results along with a comparison with other commercial source models show good consistency between simulated I-125 source (model 6711) results and other simulation results of seed's dosimetric parameters in the literature. It is noted that a little more differences between our simulation results and reported experimental data could be due to the experimental errors in the measurements, imprecision of dosimeter positioning during the experiment, and uncertainty sources in a measurement proce-

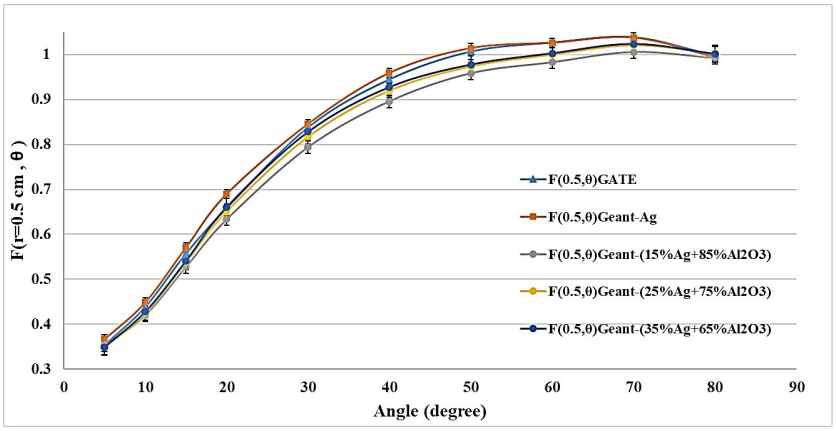

a)

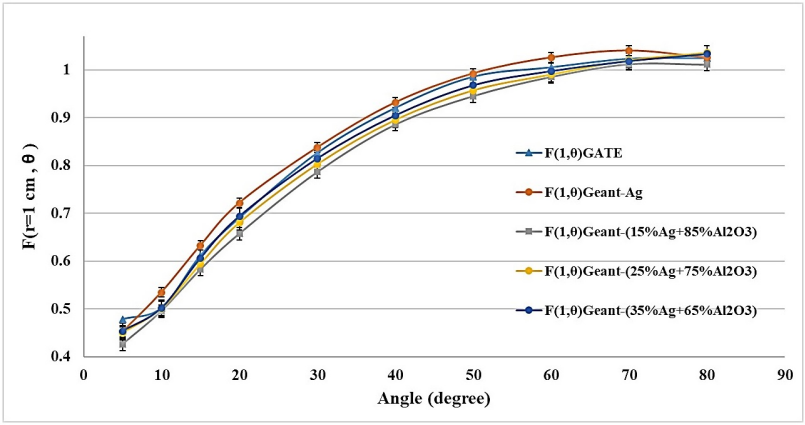

b)

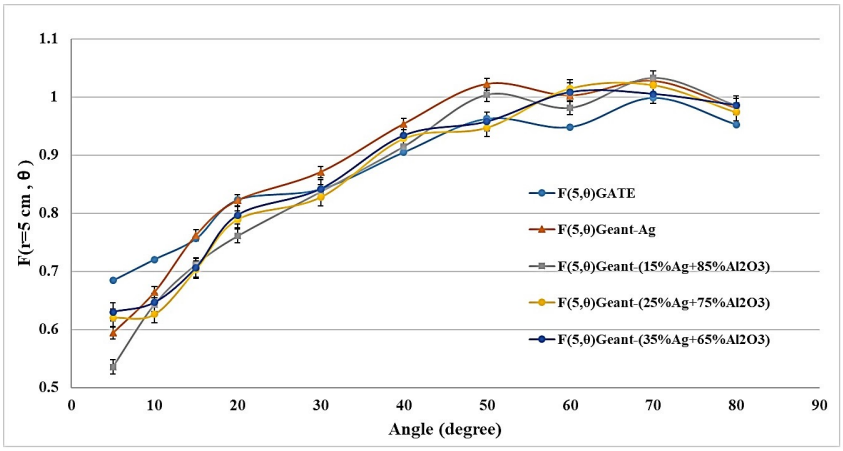

c)

Figure 4: Anisotropy function obtained by GEANT4 results and other results for 0.5 cm (a), 1 cm (b), and 5 cm (c).

dure. Furthermore, since Ag+Al_2O_3 rod has been recently introduced as a good carrier for Iodine radioisotope with relatively uniform distribution, we evaluated effect of the Ag+Al_2O_3 on the dosimetric parameters of new Iodine seed. In addition to, we assess effect of different ratio of Ag and Al_2O_3 in the final composition of the marker on the radial dose functions and anisotropy functions of the seeds. Our results show the similarity between model 6711 and simulated new seeds containing cylindrical Ag+Al_2O_3 markers in the same protocol. So that, results indicate mean difference of less than 5% in calculating the radial dose function and less than 6% in estimating the anisotropy functions.

Conflict of Interest

The authors declare no potential conflict of interest regarding the publication of this work.

Copyright

References

Babaheidari, A. and Shamsaee, M. (2014). Determination of dosimetric characteristics of a new design ^{125}I brachytherapy source with an Ag+ Al_2O_3 marker using the Monte Carlo code MCNPX. *Radiochemistry*, 56(5):550–553.

Fardi, Z. and Taherparvar, P. (2019). A Monte Carlo investigation of the dose distribution for new I-125 low dose rate brachytherapy source in water and in different media. *Polish Journal of Medical Physics and Engineering*, 25(1):15–22.

Ghiassi-Nejad, M., Jafarizadeh, M., Ahmadian-Pour, M., et al. (2001). Dosimetric characteristics of ^{192}Ir sources used in interstitial brachytherapy. *Applied Radiation and Isotopes*, 55(2):189–195.

Meigooni, A. S. (1995). Dosimetry of interstitial brachytherapy sources: recommendations. *Med Phys*, 22(2):2.

Rajabi, R. and Taherparvar, P. (2019). Monte Carlo dosimetry for a new 32P brachytherapy source using FLUKA code. *Journal of Contemporary Brachytherapy*, 11(1):76–90.

Rivard, M. J. (2009). Monte Carlo radiation dose simulations and dosimetric comparison of the model 6711 and 9011 brachytherapy sources. *Medical Physics*, 36(2):486–491.

Rivard, M. J., Coursey, B. M., DeWerd, L. A., et al. (2004). Update of AAPM Task Group No. 43 Report: A revised AAPM protocol for brachytherapy dose calculations. *Medical Physics*, 31(3):633–674.

Rodríguez, E. A., Alcón, E. P., Rodriguez, M. L., et al. (2005). Dosimetric parameters estimation using PENELOPE Monte-Carlo simulation code: Model 6711 a ^{125}I brachytherapy seed. *Applied Radiation and Isotopes*, 63(1):41–48.

Russell, K. and Blasko, J. (1993). Recent advances in interstitial brachytherapy for localized prostate cancer. *Problems in Urology*, 7:260–260.

Taherparvar, P. and Fardi, Z. (2021). Development of GATE Monte Carlo Code for Simulation and Dosimetry of New I-125 Seeds in Eye Plaque Brachytherapy. *Nuclear Medicine and Molecular Imaging*, 55(2):86–95.

Taherparvar, P. and Fardi, Z. (2022). Comparison between dose distribution from ^{103}Pd, ^{131}Cs, and ^{125}I plaques in a real human eye model with different tumor size. *Applied Radiation and Isotopes*, 182:110146.

RPE | Radiation Physics & Engineering
An International Peer-Reviewed Journal
Published by K.N. Toosi University of Technology
http://rpe.kntu.ac.ir
Research Article

Radiation Physics and Engineering 2023; 4(2):25–33

Computational study of the effect of sapphire neutron filter on reducing the neutron and secondary-gamma dose rate around the main shield of D channel in TRR

Zohreh Gholamzadeh

Reactor and Nuclear Safety Research School, Nuclear Science and Technology Research Institute (NSTRI), Tehran, Iran

HIGHLIGHTS

- Sapphire crystal has noticeable impact on the dose rates around a neutron beam line shield.
- Simulation methods are vital to investigate the dose rates behavior without practical high costs.
- Benchmark studies are very important procedures to evaluate the simulation accuracy degree.

ABSTRACT

Simulation work provides valuable information on the behavior of different research reactor neutron analysis facilities. The present study considered neutron and secondary-gamma dose rate variations by applying a sapphire crystal inside the *D* channel in Tehran Research Reactor (TRR). The MCNPX computational code was used to model the channel and its designed shield. Neutron and gamma dose rates distributions were calculated with a sapphire crystal modeling to investigate the neutron diffraction facility hall dose rates. The data from the dose rate simulations were compared with the experimental data available at a power of 4.2 MW from the research reactor. The comparison showed that there is very good conformity between two data series. The simulated neutron dose rate in front of the main shield overestimated the measurement data by 57% in closed-shutter situation and underestimated the measured data by 32% in open-shutter measurement situation. The investigation has shown that adjusting the crystal size to the channel size is considerably effective, especially at high leakage positions.

KEYWORDS

Neutron filter
Neutron and gamma dose rate
Sapphire crystal
Tehran Research Reactor
MCNPX simulation
Benchmark study

HISTORY

Received: 28 July 2022
Revised: 15 September 2022
Accepted: 23 September 2022
Published: Spring 2023

1 Introduction

Newly crystalline materials (mainly single crystals) are effectively used to filter fast neutrons emerging from the neutron beam lines of the research reactors. These crystals decrease noticeably the backgrounds at the sample table of the neutron analysis experiments.

Perfect single crystals can be used as filters to produce a thermal-neutron beam almost free of fast neutron background. The filter material must have a wavelength dependent cross-section in such a way that is low for thermal but strongly increasing at epithermal and high energies. The selection of the filter material and its dimensions are critical parameters affecting the performance of a neutron diffusion instrument (Stamatelatos and Messoloras, 2000).

Several materials such as quartz (SiO_2), bismuth, silicon, germanium, lead and sapphire (Al_2O_3) have been suggested as the most successful neutron filters. Of the crystals mentioned, only one Al_2O_3 sapphire crystal was found to be the most efficient fast neutron filter and was incorporated into many neutron instruments (Stamatelatos and Messoloras, 2000). Until now, no database containing thermal cross sections of the most used crystals, such as sapphire is available (Zahar et al., 2016).

The overall cross section σ_{th} is a superposition of several contributions: (a) absorption, σ_{a}, proportional to neutron wavelength, (b) inelastic, σ_{inel}, and (c) elastic or Bragg scattering, σ_{ela} which depends on neutron wavelength, crystal orientation and crystal perfection. Item (b) depends on crystal temperature (phonon population), where coherent Bragg scattering can be disallowed by using a particular crystal orientation (Zahar et al., 2016):

$$\sigma_{\text{th}} = \sigma_{\text{a}} + \sigma_{\text{inel}} + \sigma_{\text{ela}} \tag{1}$$

*Corresponding author: zgholamzadeh@aeoi.org.ir

https://doi.org/10.22034/rpe.2022.353820.1099
https://dorl.net/dor/20.1001.1.26456397.2023.4.2.4.0

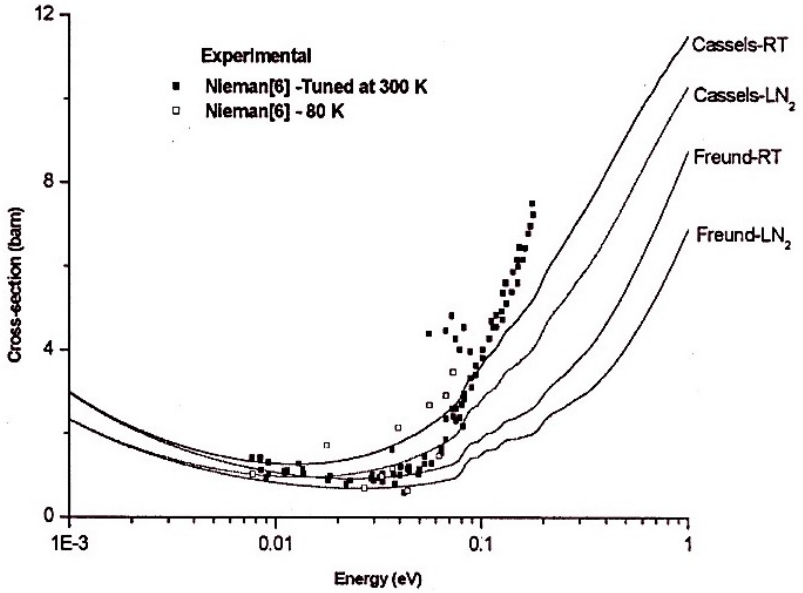

Figure 1: Sapphire total neutron cross-section at room and liquid N_2 temperatures (Adib and Kilany, 2003).

The first contribution, $\sigma_{\rm a}$, for sapphire is simply proportional to the neutron wavelength λ and energy in the range $(10^{-4} < E < 10)$ eV. Thus, $\sigma_{\rm a}$ can be written as (Adib and Kilany, 2003):

$$\sigma_{\rm a} = C_1 E^{-\frac{1}{2}} \tag{2}$$

where C_1 is a constant which can be calculated from values provided by V.F. Sears (Adib and Kilany, 2003).

The second term of Eq. (1) is called thermal diffuse scattering (TLD) or inelastic scattering that is given by (Adib and Kilany, 2003):

$$\sigma_{\rm TLD} = \left(\frac{A}{1+A}\right)^2 \sigma_{\rm bat}\left(1 - {\rm e}^{-WC_2E}\right) + E^{-\frac{1}{2}} \begin{cases} \left(C_1 + \dfrac{\theta_D^{\frac{1}{2}}\,\sigma_{\rm bat}}{36\,A}\,R\right) & \text{for } x \le 6 \\ \left(C_1 + \dfrac{\theta_D^{\frac{1}{2}}\,\sigma_{\rm bat}}{36\,A}\,3.3\,x^{-\frac{7}{2}}\right) & \text{for } x > 6 \end{cases} \tag{3}$$

where ${\rm e}^{-W}$ is the Debye-Waller factor, C_2 is a constant which is dependent on the scattering material and given by $C_2 = 4.27\exp(A/61)$, $X = \theta_D/T$ (T is the sample temperature), $\sigma_{\rm bat}$ is the sum of coherent and incoherent scattering cross-sections of the bound atom), A in case of compounds is the average atomic mass number, and the series R is given by

$$R = \sum_{n=0}^{22} \frac{B_n\,x^{n-1}}{n!\,(n+\frac{5}{2})} \tag{4}$$

with B_n that is the Bernoulli numbers.

The optimum filter thickness, the crystal orientation and the temperature give the maximum efficiency of such filter. One can also use the quality factor R, defined by the ratio of the total cross section at thermal energies, $\sigma_{\rm th}$, to the total cross section at high energies, $\sigma_{\rm free}$ (Zahar et al., 2016):

$$R = \frac{\sigma_{\rm th}}{\sigma_{\rm free}} \tag{5}$$

In the case of mono-crystalline material, the Bragg scattering cross-section is given by (Adib et al., 2005):

$$\sigma_{\rm Bragg} = \frac{1}{Nt_0}\ln\left(\frac{1}{T_{\rm Bragg}}\right) \tag{6}$$

where N is the number of atoms.cm^{-3}, t_0 is the effective thickness of the crystal in cm, and $T_{\rm Bragg}$ is the resulting neutron transmission from different (hkl) planes, given by (Adib et al., 2005):

$$T_{\rm Bragg} = \prod_{hkl}\left(1 - P_{hkl}^{\theta}\right) \tag{7}$$

where P_{hkl}^{θ} is the reflecting power of the (hkl) plane inclined by an angle θ_{hkl} to the incident beam direction (Adib et al., 2005). Based on Fig. 1, the researchers measured the total neutron cross section of the sapphire crystal (001).

According to a published manuscript, the absorption cross section of sapphire crystal is 0.231 b at room temperature and its total is 15.7 b (Adib, 2008). Usually other crystals need to cool to present an expected behavior as a good neutron filter. Adib et al. (Adib and Kilany, 2003) showed agreement between calculations and experimental was obtained for values of Bi-single crystals, at room and liquid nitrogen temperatures. Therefore, in the following, a review on the unique sapphire crystal (Al_2O_3) would be done to reveal its effectiveness for the mentioned purpose.

Adib et al. (Adib et al., 2003) used a simple additive formula that permits the calculation of the nuclear capture, thermal diffuse and Bragg scattering cross-sections

as a function of sapphire temperature and crystal parameters. Their results showed that there is an overall agreement between the theoretical formula and experimental data. They suggested the use of sapphire single-crystal as a fast neutron filter in terms of the optimum crystal thickness, mosaic spread, temperature, cutting plane and tuning for efficient transmission of thermal-reactor neutrons. Their calculation shows that 7.5 cm thick sapphire single crystal, cut along a-axis and with a FWHM on a mosaic spread of 5 min of arc, is a good fast neutron filter. A crystal cut along c-axis with a mosaic spread of about 1° is also an efficient fast neutron filter, when it is fine-tuned to minimize the attenuation for each neutron energy of interest (Adib et al., 2003).

The carried out research by Adib (Adib, 2008) showed a small increase $\approx 5\%$ at neutron energies < 0.02 eV in the neutron transmission through the cooled sapphire crystal at LN_2 temperatures. Therefore, it can be concluded that the crystal can be used at room temperature with no concerns regarding the reduction of the neutron flux transmitted after the crystal.

Born et al. (Born et al., 1987) have examined the intensity transmitted by a single-crystal of Al_2O_3 over a range of orientation angles within $\pm 2°$ and did not see any significant change. They have found that a 90 mm-long sapphire-crystal filter has a transmission of about 0.8 for wavelengths in the range (0.12 to 0.24) nm and 0.07 for epithermal neutrons. These transmission results are in good agreement with those obtained by Nieman et al. (Nieman et al., 1980), who suggest that the effective attenuation coefficient can be minimized by fine-tuning of the crystal orientation. Born et al. have found that there is no need to tune the crystals for every wavelength if the crystal mosaic spread is as enough as small. They found that the intensity of the transmitted beam by their crystals does not depend on the orientation of the crystal (Nieman et al., 1980).

Stamatelatos and Messoloras (Stamatelatos and Messoloras, 2000) indicated, the optimum sapphire filter thickness is that which maximizes the slow neutron transmission and minimizes the fast one, so that there is no severe reduction of the thermal neutron flux. Their calculations carried out by these authors showed using 15 cm c-axis sapphire crystal there is 62% transmission of neutrons with 0.11 nm wavelength and 76% transmission for 0.25 nm neutrons. Fast neutron transmission is 3% (Stamatelatos and Messoloras, 2000).

Adib (Adib, 2005) investigated a-axis and c-axis sapphire crystals and indicated that the neutron transmission through 8 cm sapphire single crystal with mosaic spread of $5'$ along the a-axis is less disturbed by parasitic Bragg reflections than along the c-axis. Since the strong reflections from (119) and (113) planes disturb the neutron transmission along the c-axis $E \cong 0.02$ eV. As can be also observed parasitic Bragg reflections can limit the use of sapphire as a thermal neutron filter for mosaic spreads $> 5'$ (Adib, 2005).

Many research reactors have used the sapphire crystal inside their radial neutron beam lines to decrease the neutron/gamma backgrounds at the sample position of their neutron analysis facility (Mishra et al., 2006; Mach, 2018).

In addition, the main shield and sapphire crystal, some shield walls are used around these neutron installations to reduce staff exposures. For example, HANARO Advanced High Flux Neutron Application Reactor is a 30 MW multifunction research reactor located in Dajon, Republic of Korea that uses some zooning shield walls around its neutron diffraction facilities. The shielding walls around the neutron facilities installed in this reactor are made of heavy concrete (http://www.koreaherald.com/view.php?ud=20140624001075).

The present work aims to investigate the effect of sapphire crystal on the reduction of neutron and secondary gamma dose rates around the main shield of the Tehran Research Reactor (TRR) diffraction facility.

2 Materials and Methods

Tehran research reactor (TRR) is being equipped to a neutron diffraction facility. The reactor core is composed of two types of fuel assembly that are standard fuel elements and control fuel elements. The core consists of 28 standard fuel element (SFE) containing 19-fuel plates and 5 control fuel elements (CFE) containing 14 fuel plates according to the core specifications. The modeled reactor is a 5 MW reactor light water cooled with 500 $m^3.h^{-1}$ flow rate. Two types of control rods are used in the TRR; which one made out of Ag-In-Cd alloy, and the other of stainless steel. Both have a set of two control plates as a fork type shape. The reactor fuel is U_3O_8-Al containing

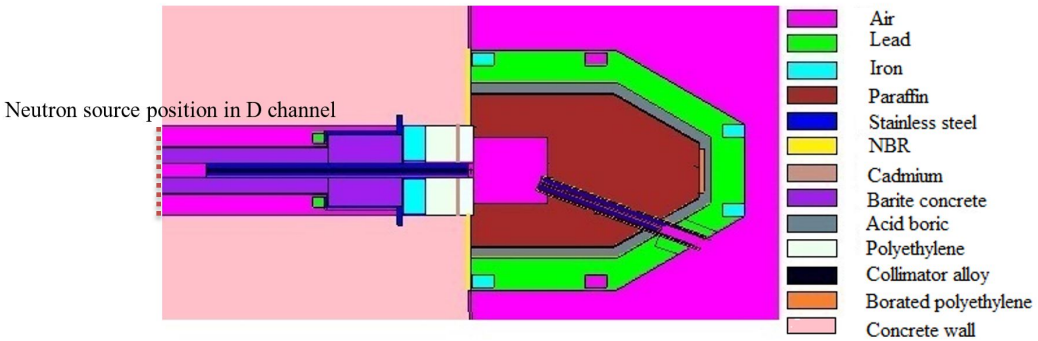

Figure 2: Detail of the used pieces inside D channel and the main shield simulated using MCNPX.

20%-enriched uranium (Mirvakili et al., 2012).

MCNPX code was used to simulate the main shield of TRR diffraction facility (Pelowitz et al., 2005). The simulated main shield details are shown in Fig. 2. The shield has been constructed with the optimized dimensions according to Ref. (Menarebazari et al., 2022). As in the figure is seen, the shield is composed of three layers; 55 cm paraffin, 5 cm boric acid, 15 cm lead respectively of which the final layer is lead. A monochromator room is seen in the figure with dimension of 30×40 cm^2 which a 60 cm-long soller collimator installed on its corner would guide the reflected monochromatic neutrons at 20 angel toward outside the shield. After paraffin layer, 1.5 cm thick borated-polyethylene (7%-borated) and 3 mm cadmium sheets of 20×25 cm^2 were used as thermal neutron beam stop inside the second layer (boric acid).

D channel of TRR is a 6-inch radial beam tube that guides the neutrons emerging from the TRR core towards the reactor hall. A high-density concrete collimator holder was used inside the channel according to Fig. 1, the concrete part length is 120 cm. A soller collimator with 120 cm length consist of a stainless steel fram and three narrow sheets which have divided the empty cubic space of the collimatar is used inside the concrete holder. After the concrete holder, an iron disc-shaped piece 10 cm thick is used. Then 15 cm thick polyethylene disc has been used. As a final piece, a borated-polyethylene (7%) of 5 cm thick has been used. A 2 mm cadmium disc was used between the polyethylene disc and the borated-polyethylene disc. Because the main shield would not stand completely fit with the concrete wall of the TRR research reactor, a 2 cm Nitrile Butadin Rubber (NBR) was used between the wall and main shield as flexible neutron shield material.

As the figure shows, different matrials are used to shield the neutron and gamma rays emerged from the *D* channel of TRR. The main shield materials are presented as the following: Air: invironment material, Lead: final gamma shield, Iron: shield first gamma shield inside *D* channel, Paraffin: neutron shield, Stainless steel: soller colimators' material, NBR: flexible neutron shield for the gap between TRR wall and main shield, cadmium: thermal neutron absorber at the designed beam stop window inside acidboric layer, Barite concrete: first soller colimator holder material, Acid boric: neutron absorber material before lead layer, Polyethylene: heat-resistent neutron moderators inside *D* channel, Collimator alloy: strain-resistent alloy of the soller collimator structure, Borated polyethylen: thermal neutron absorber at the designed beam stop window inside acidboric layer, Concrete wall: the TRR pool wall. The position of the neutron source is shown in the figure with a dash line.

As the figure shows, six iron girders were used at different positions of the main shield structure, which two of them (the middle ones) did not fill with lead during the casting process whereas they were not accessible.

Neutron and gamma sources of TRR were defined in MCNPX input so that their energy spectrum and spatial distribution could give the most precise modeling to the real diffusion of the particles inside the TRR *D* channel (Fig. 3). Then the gamma and neutron dose rates in front of the modeled shield and beside the wall near the NBR layer were calculated. DE/DF card and ANSI/ANS-6.1.1-1977 flux to dose conversion factors were used to calculate the gamma dose rates. Flux to dose conversion factor of NCRP-38, ANSI/ANS-6.1.1-1977 was used to calculate the neutron dose rates. The neutron and gamma dose rates were calculated at different positions around the shield with and without sapphire crystal application inside the *D* channel that is to be installed before the concrete collimator holder. The neutron spectra was defined at the mentioned position according to the Fig. 3 which shows smooth distribution of neutron source without the sapphire crystal, as well as the reduced positional intensity of the neutron source by using the sapphire crystal. Neutron spectra before the sapphire crystal has been shown in Fig. 4.

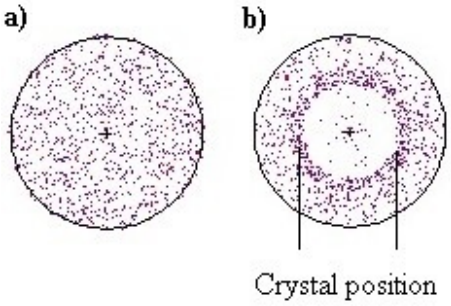

Figure 3: Neutron source definition a) smooth distribution without sapphire crystal b) non-smooth distribution with sapphire crystal.

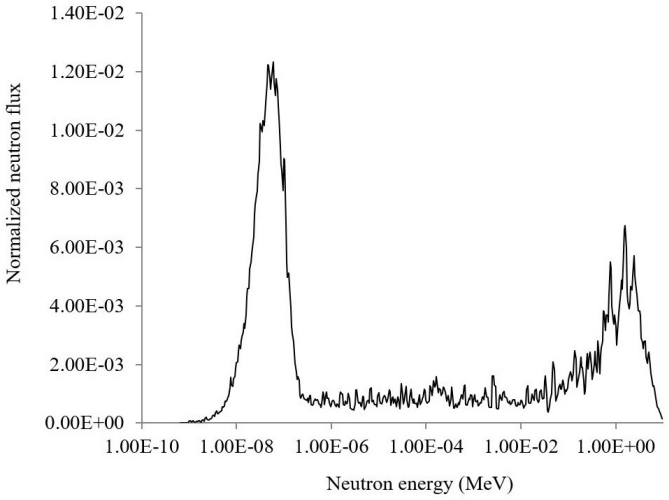

Figure 4: Neutron spectra obtained using MCNPX code before first soller collimator holder.

To define the neutron source when a sapphire crystal is used inside the *D* channel, the reduction factor as mentioned by the different experimental and theoretical works was applied for the radial distribution of the neutron source as well as the neutron energy of the spectra.

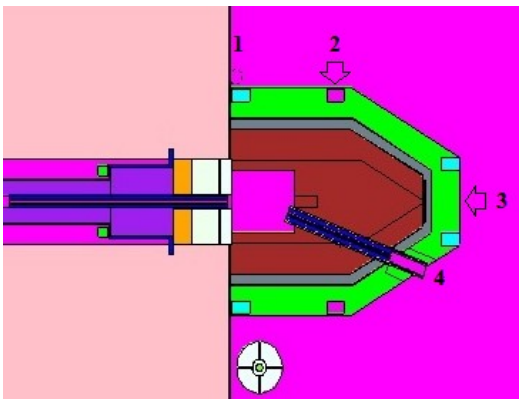

Figure 5: The different positions for neutron and gamma dose rates calculations around the main shield of TRR, dxt sphere is observed at position No. 1.

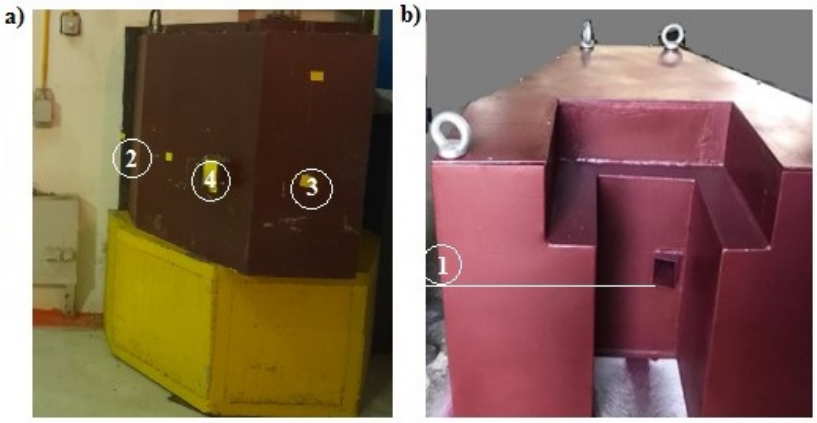

Figure 6: The constructed and installed main shield a) front view, b) back view that the second collimator entrance is clear in this view where the point No. 1 and other ones have been selected co-level with it.

The reduction factor was chosen according to Ref. (Adib, 2008). Hence, the intensity of the neutrons with an energy more than 1 eV was reduced by a 0.9 factor in the spectra shown in Fig. 4. In addition, the radial distribution of neutron spectra was reduced by the same factor, which indicates the crystal position. It should be mentioned any cross section for crystalline materials are not available in the used version of MCNPX code. Therefore, the crystal effects on neutron spectra has been applied for the following simulations and the crystal material was not modeled inside the D channel. The neutron source was defined by SDEF card before the first soller collimator holder. In addition, the crystal size effect on the neutron and gamma dose rates was investigated using enhancement of the crystal diameter in the neutron source definition of the MCNPX SDEF card. Clearly, reduction of the neutrons using the sapphire crystal would decrease the secondary gamma dose rates. Therefore, neutron dose rate and secondary gamma dose rate tallies were used in the MCNPX code input file for any code being performed. Mesh tally card was applied to determine the neutron and gamma dose rate distributions around the modeled shield. In addition, the primary gamma dose rates were calculated using a smooth gamma source definition in the MCNPX code input. Figure 5 shows the positions (No. 1 up to No. 4) that the neutron and gamma dose rates were calculated around the main shield of the TRR D channel. A shutter also is being designed for the shield to avoid any neutron and gamma departure from the second soller collimator towards the TRR hall when the facility is not under operation. In the present work, the gamma and neutron dose rates of the position No. 3 were calculated in open shutter situation.

Figure 6 shows the constructed and installed main shield which has been modeled in detail by MCNPX code.

Dextran card (dxt) was used for the calculations as a variance reduction method to decrease the statistical errors of the calculations. Neutron flux distribution of thermal energy range ($E_n < 0.4$ eV) and fast energy range ($E_n > 1$ keV) were calculated using mesh tally card of the used computational code too.

Finally, a benchmark study was carried out for position No. 3 at 4.2 MW operation of TRR to verify the obtained simulation data accuracy.

3 Results and Discussion

Neutron and gamma dose rates were calculated for position No. 1 (beside the concrete wall gap), position No. 2 (in front of the empty iron girder), position No. 3 (in front

Table 1: Neutron dose rate of different positions around the D channel main shield.

Position number	No. 1 (μSv.h^{-1})	No. 2 (μSv.h^{-1})	No. 3 (μSv.h^{-1})	No. 4 (μSv.h^{-1})
Without sapphire	8930	6520	314	580
With sapphire Dia. 14 cm	2580	966	155	270
With sapphire Dia. 15 cm	1256	853	153	264

Table 2: Secondary gamma dose rate of different positions around the D channel main shield.

Position number	No. 1 (μSv.h^{-1})	No. 2 (μSv.h^{-1})	No. 3 (μSv.h^{-1})	No. 4 (μSv.h^{-1})
Without sapphire	3160	1000	5.4	222
With sapphire Dia. 14 cm	1170	395	4.2	12.3
With sapphire Dia. 15 cm	1162	314	4.1	10.2

of the main shield third layer in direct beam leakage path) and position No. 4 (in front of the second soller collimator exit). The obtained results presented in Table 1 show that in the case of position No. 1, the neutron dose rate could be reduced from about 9 mSv.h^{-1} to 1 mSv.h^{-1} by using sapphire crystal, which the drop is noticeably. It should be mentioned that the D channel diameter is about 16 cm. The calculations showed that in this position, by changing the crystal diameter from 14 cm to 15 cm, the neutron dose rate would be reduced by half (2.580 mSv.h^{-1} to 1.256 mSv.h^{-1}). The obtained results for position No. 2 showed that using the sapphire crystal would result in a high reduction of the neutron dose rate at this position but (about 6.5 times). However, the crystal size enhancement would not have a noticeable effect on the neutron dose rate reduction at this position (only about 11.6%). In the case of position No. 3, application of sapphire crystal inside the D channel would reduce the neutron dose rate by half. The low reduction of the neutron dose rate at this position is resulted as the fact that the crystal is fast neutron shield so the most arrived neutrons to this position are thermal hence thermal flux had not much reduction in direct neutron beam path with and without sapphire crystal. In addition, the crystal size enhancement would not have any effect on the neutron dose rate at position No. 3 (155 ± 7.9 μSv.h^{-1} to 153 ± 8.7 μSv.h^{-1}) so it can be said the difference between the values is in the statistical error range of about 5%. The carried out calculations showed that according to Table 1, the neutron dose rate would be reduced by half at position No. 4 (580 μSv.h^{-1} to 270 μSv.h^{-1}) using a sapphire crystal at D channel of TRR. In addition, the crystal size reduction has not any noticeable effect on neutron dose rate reduction at this position. The same reasons for position No. 3 could be accounted for position No. 4, while the second collimator body is stainless steel (a fast neutron scattering material). In overall, the calculations indicate that the crystal has a high effect on the neutron dose rate for the positions that have high neutron leakage without experiencing many moderator materials.

Clearly, it would be expected that the secondary gamma dose rates are reduced by using sapphire crystal inside the D channel of TRR. Table 2 shows the obtained results of the secondary gamma dose rate calculations. According to Table 2, position No. 1 gamma dose rate would be reduced to one third using sapphire crystal. Position No. 2 shows the same behavior. Position No. 3 gamma dose rate would be reduced slightly (about 22%) by using sapphire crystal as the fact that the highest (n, γ) reaction rates inside paraffin belong to low energy neutrons which are not filtered by the crystal. Application of the sapphire crystal has a noticeable effect on the gamma dose rate of position No. 4, which is the second collimator exit position. In the case of all the positions, the crystal size enhancement has no obvious effect on the gamma dose rate reduction.

In overall, it can be said the most affected positions of the crystal size are No. 1 owing to its high neutron leakage and No. 4 owing to its high gamma leakage.

Mesh tally was used to map the dose rates around the main shield. The calculations were carried out with the expectation of a 15 cm-diameter sapphire crystal presence inside the D channel. The carried out calculations showed that the average neutron dose rate in front of the main shield is about 100 μSv.h^{-1} while the values increase near the concrete wall where the highest neutron leakages are possible. The mesh tally calculations showed that in front of the main shield the average gamma dose rate is about 116 μSv.h^{-1} (Fig. 7).

Neutron flux distribution around the main shield was investigated using mesh tally according to Fig. 8. As the figure shows near the concrete wall, the average total neutron flux changes from 10^4 n.s^{-1}.cm^{-2} up to 10^5 n.s^{-1}.cm^{-2} while in front of the main shield the value decreases to the order of 10^3 n.s^{-1}.cm^{-2}. In addition, the figure shows the fast neutron flux in front of the main shield would be in order of less than 34 n.s^{-1}.cm^{-2}.

Figure 4 shows the primary gamma distribution around the main shield. The carried out investigations showed the average gamma dose rate is about 18 μSv.h^{-1} in front of the main shield while the highest leakage is observed around the empty girders.

The carried out investigations show there needs to be reinforced near the empty iron girders as well as the gap between the concrete wall and the main shield, especially in view of neutron shielding. It should be mentioned construction of a bigger main shield was not possible on account of its weight limitations. In addition, the facility is to be used for diffraction equipment, where the bigger shield would disturb proper installation of the equipment.

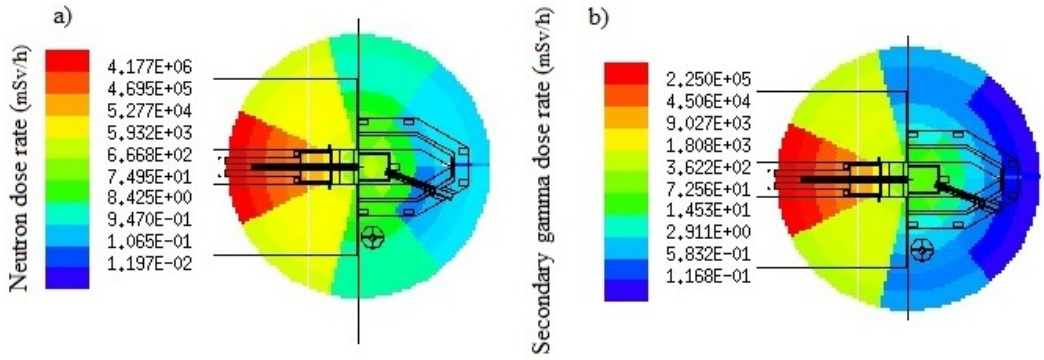

Figure 7: Dose rate distribution around the main shield of the TRR *D* channel a) Neutron b) Secondary gamma.

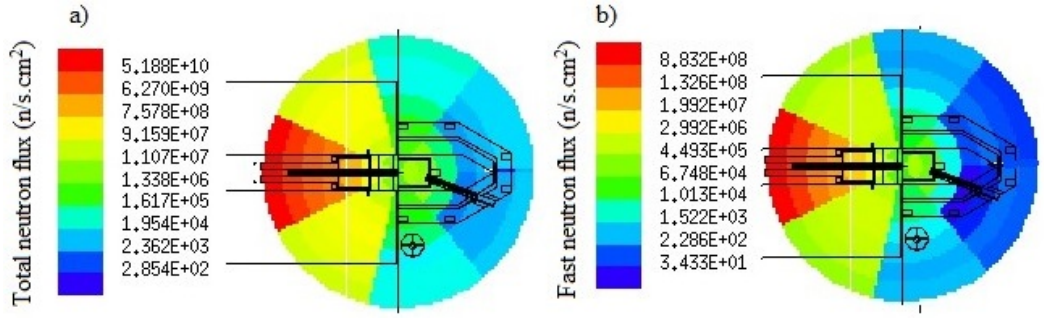

Figure 8: Neutron flux distribution around the main shield of the TRR *D* channel a) Total b) Fast.

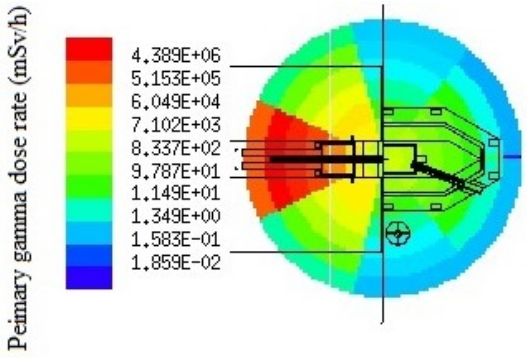

Figure 9: Primary gamma dose rate distribution around the main shield of the TRR *D* channel.

Hence, the local reinforcements would damp the high exposure problems around the main shield.

Neutron and gamma dosimetry was carried out at position No. 3, which has been depicted in Fig. 5, which is a location exactly in the middle of the direct beam leakage after the lead layer of the main shield. The measurement was done at different TRR powers (Fig. 10). According to the figure, the simulated neutron dose rate is 1.57 times (57%) higher than the measured value at 4.2 MW power in the situation of a closed unfit shutter installed on the second soller collimator exit. The simulation value was 32% less than the measured neutron dose rate at 4.2 MW in open shutter situation of the second soller collimator.

The carried out benchmark study showed good agreement between the simulation and experimental data. The observed discrepancy between the two data is arisen from the fact the dose rate calculations could not be done using KCODE mode of the MCNPX code which involves completely the research core geometry with the installed facility on its *D* channel. Complication of the modelled geometry would result in long run times of the computational code, mainly several months. Moreover, the final run statistical errors would not be acceptable. So, the neutron and gamma sources were calculated using KCODE mode at the entrance of the first soller collimator, then the sources were defined in another MCNPX input involving only *D* channel beam line and its shield, not the whole TRR core. Hence, this discretization would result in some calculation errors itself. The facility beam shutter has not been completed yet. The above-mentioned measurement plots have been done using another unfit shutter, so the in front dose rate measured values may be less when a fit

shutter is installed. The TRR core configuration is another reason for the observed discrepancies between simulation and experimental data. It should be mentioned the TRR core configuration might change in every operation run, which would result in variation of the source terms even up to 30%. The used dosimeter uncertainties in experimental measurements would be another reason for the observed discrepancies between the simulation and experimental data.

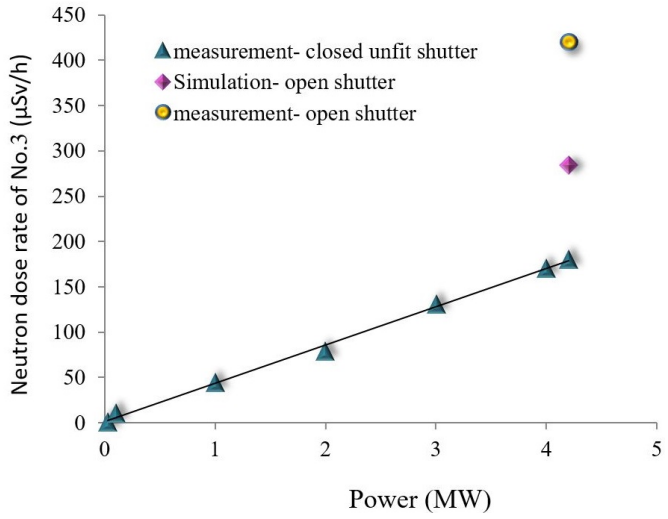

Figure 10: Comparison of neutron dose rate measurement and simulation at position No. 3 (in front of the main shield) .

4 Conclusion

Simulation data before installation of the neutron facilities in the research reactors could effectively guide the researches and the beam line operators to design the suitable required shield material around the facility. The present work using MCNPX code to simulate TRR D channel is to be applied to monochromatic neutron cross section measurement with different materials. The carried out simulation showed that the sapphire crystal application inside the beam channel would drastically decrease the neutron dose rates around the main shield of the D channel especially in high-leaked neutron positions. Fitting the sapphire crystal with the D channel diameter would not have a significant effect on the experienced neutron dose rate of the different investigated positions except the position No. 1 where the dose rate reduction is about half because of the excessive leakage of the neutrons from this position (gap between the concrete wall and the main shield). Whereas the neutron flux reduction by using the sapphire crystal inside the D channel would result in secondary gamma reduction, the secondary gamma dose rates were calculated. The calculations showed that the crystal application reduces the secondary gamma dose rate noticeably (about 3 times) at positions No. 1 and No. 2 which are the high-leaked gamma positions. The crystal size fitting with the D channel diameter has no significant effect on the secondary gamma dose rates (because the variation is in the range of statistical calculation errors of $\sim 5\%$), except position No. 2 which is a high-leaked gamma area. The crystal diameter enhancement from 14 cm to 15 cm would result in 20% reduction of the secondary gamma dose rate at position No. 2. In overall, the calculations indicate the high-leaked positions need reinforcement and the sapphire crystal size should be as possible as fit with the D channel size without considerable gap when it is installed inside the channel. The study also helped to select the proper partitioning that was to be done around the facility to protect the reactor personnel from high radiation exposures.

Conflict of Interest

The authors declare no potential conflict of interest regarding the publication of this work.

Copyright

References

Adib, M. (2005). Cross-section of single-crystal materials used as thermal neutron filters.

Adib, M. (2008). Attenuation of Reactor Gamma Radiation and Fast Neutrons Through Large Single-Crystal Materials. *Proceedings of the 3rd Environmental Physics Conference, 19-23 Feb. 2008, Aswan, Egypt, pp.257-272.*

Adib, M. and Kilany, M. (2003). On the use of bismuth as a neutron filter. *Radiation Physics and Chemistry*, 66(2):81–88.

Adib, M., Kilany, M., Habib, N., et al. (2003). Neutron Transmission of Single-Crystal Sapphire Filters. *4th Conference on Nuclear and Particle Physic; EG0600145 ,11-15 Oct. 2003, Fayouni , Egypt, pp.224-237.*

Adib, M., Kilany, M., Habib, N., et al. (2005). Neutron transmission of single-crystal sapphire filters. *Czechoslovak Journal of Physics*, 55(5):563–578.

Born, R., Hohlwein, D., Schneider, J., et al. (1987). Characterization of a sapphire single crystal for the use as filter in thermal neutron scattering. *Nuclear Instruments and Methods in Physics Research Section A: Accelerators, Spectrometers, Detectors and Associated Equipment*, 262(2-3):359–365.

Mach, W. (2018). *Installation of a neutron beam instrument at the TRIGA reactor in Vienna.* PhD thesis, Wien.

Menarebazari, Z. A., Jafari, H., Gholamzadeh, Z., et al. (2022). The design and optimization of a radiation shield for the Tehran Research Reactor's neutron diffraction facility. *Progress in Nuclear Energy*, 148:104224.

Mirvakili, S., Keyvani, M., Arshi, S. S., et al. (2012). Possibility evaluation of eliminating the saturated control fuel element from Tehran research reactor core. *Nuclear Engineering and Design*, 248:197–205.

Mishra, K. K., Hawari, A. I., and Gillette, V. H. (2006). Design and performance of a thermal neutron imaging facility at the North Carolina State University PULSTAR reactor. *IEEE Transactions on Nuclear Science*, 53(6):3904–3911.

Nieman, H., Tennant, D., and Dolling, G. (1980). Single crystal filters for neutron spectrometry. *Review of Scientific Instruments*, 51(10):1299–1303.

Pelowitz, D. B. et al. (2005). MCNPX users manual. *Los Alamos National Laboratory, Los Alamos*, 5:369.

Stamatelatos, I. and Messoloras, S. (2000). Sapphire filter thickness optimization in neutron scattering instruments. *Review of Scientific Instruments*, 71(1):70–73.

Zahar, N., Benchekroun, D., Belhorma, B., et al. (2016). Study of Sapphire and MgO as Thermal Neutron Filters for The TRIGA Moroccan Reactor Beam ports. *International Journal of Advanced Research*, 4(7):560–567.

RPE | Radiation Physics & Engineering
An International Peer-Reviewed Journal
Published by K.N. Toosi University of Technology
http://rpe.kntu.ac.ir
Research Article

Radiation Physics and Engineering 2023; 4(2):35–37

Design and construction of the experimental plasma water activation system

Malihe Omrani[a,*], Hossein Sadeghi[b], Samaneh Fazelpour[c]

[a] *Department of Biotechnology, Persian Gulf Research Studies Center, Persian Gulf University, 75169, Bushehr, Iran*
[b] *Energy Engineering and Physics Department, Amirkabir University of Technology, P.O. Box 1591634311, Tehran, Iran*
[c] *Plasma Physics and Nuclear Fusion Research School, Nuclear Science and Technology Research Institute, P.O. Box 14155-1339, Tehran, Iran*

HIGHLIGHTS

- The PAW activity is due to the plasma reactive species.
- Discharge time affect the PAW properties.
- PAW play an effective role in different fields, such as food industry, agriculture, and healthcare.
- By increment of the treatment time, Nitrite and nitrate concentrations of PAW are increased and pH is decreased.

ABSTRACT

Design, construction, and experimental investigation of the plasma water activation device have been presented in this article. In this design, one of the electrodes, which is plate ss316, is placed in water. The other electrode which is made from tungsten is placed inside a glass tube and immersed in water. Air is also blown into the water through a constant rate air pump of 5 L.min^{-1}. An AC power supply with voltage and current of 15 kV and 30 mA has been used to create plasma in water. The results of the analysis of nitrite, nitrate, and pH in three water samples that have been irradiated with plasma for 10, 20, and 30 minutes showed a very significant change compared to the control sample. The pH of PAW is drastically decreased with an increase in treatment time due to the formation of strong acids. Nitrite and nitrate concentrations of PAW are increased with an increase in treatment time.

KEYWORDS

Plasma activated water
Nitrite
Nitrate
pH

HISTORY

Received: 5 April 2022
Revised: 29 August 2022
Accepted: 27 September 2022
Published: Spring 2023

1 Introduction

Freshwater is a scarce commodity that makes up only 2.5% of the earth's total water, and less than one percent of that amount can be readily available as terrestrial and surface water resources. At present, this vital commodity of life has been affected by population growth and overdevelopment, which has also led to the destruction of groundwater resources (Foster, 2017). According to available statistics, up to 10.6 billion cubic meters of surface water in Iran, including saline and brackish water. Also, despite the drought in recent decades, which has brought the country's water resources to a critical level, as well as the high need for water in agriculture and green space, much attention has been paid to the use of lower quality water resources. For example, one of these unconventional sources of water is gray water, which is effluent from household uses other than toilets (Pan et al., 2018). It is also important to develop new innovative strategies that are more effective and efficient in combating bacterial infections, with increasing concerns about the emergence of antibiotic-resistant bacteria in the health and food industries (Sakudo et al., 2019; Oh et al., 2017). Using plasma is a very cheap solution to this problem. The use of plasma technology is very effective in eliminating biological contaminants of water (fungi, bacteria, viruses). The method is simple: water is processed with electric plasma before it reaches its target. Plasma activated fluid (PAL), including PAW, is antibacterial against several microorganisms.

Previous studies showed that low-temperature plasmas can be used to generate plasma-activated water (PAW) by treating water under specific conditions, which has the

*Corresponding author: m.omrani@pgu.ac.ir

https://doi.org/10.22034/rpe.2022.336236.1068
https://dorl.net/dor/20.1001.1.26456397.2023.4.2.5.1

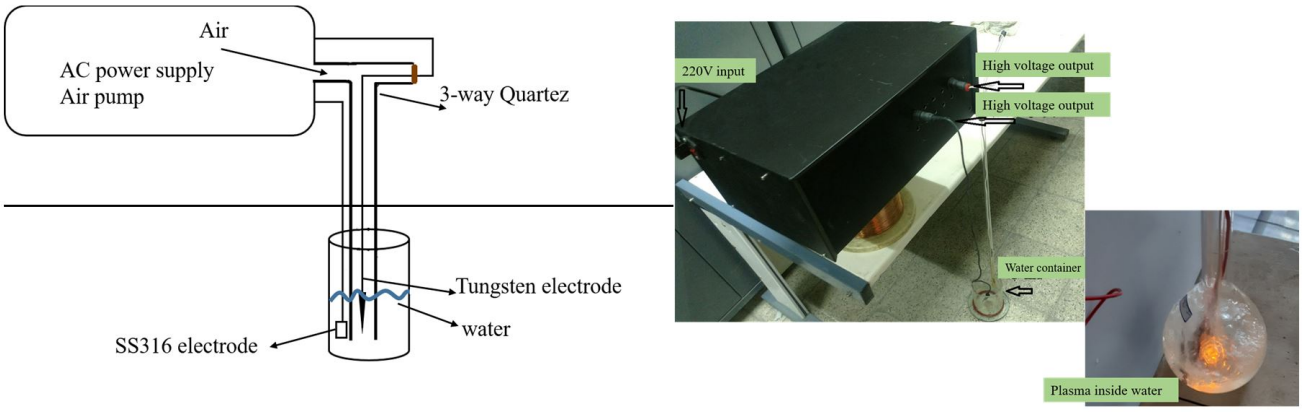

Figure 1: Left: Schematic diagram of PAW device. Right: experimental setup of PAW device.

capability of bacterial and fungi inactivation on contaminated solid surfaces or liquids (Bormashenko et al., 2012; Chen et al., 2018). Also, PAW can be used as fertilizer because it is a rich source of nitrogen oxide.

2 Experimental setup

2.1 Preparation of the materials

The fundamental method of generation of PAW involves operating a plasma generator inside the water to generate the ions, which lead to reactive species for bacterial inactivation (Soni et al., 2021).

The major components of the system included a high-voltage power supply, an air pump, and electrodes. Shematic diagram and the real picture of the experimental setup have been presented in Fig. 1. The device was specifically designed to activate water by inserting an electrode beneath the water's surface. The working gas for the plasma was normal air that was pumped by an air pump. Based on the preliminary study, the water volume, voltage, frequency, and airflow rate were set at 100 mL, 15 kV, 50 kHz, 30 mA, and 5 L.min^{-1}, respectively. Plasma-activated time was (10, 20, and 30 min). When plasma is applied to water-based liquids, it changes their characteristics (pH and electrical conductivity) and the resulting liquids are named as plasma-activated water (PAW) or plasma-activated liquid (PAL). After inactivation, the PAW was stored at room temperature.

3 Results and Discussion

Nitrite, nitrate, and pH levels of plasma-activated water have been measured. The results show that the production of plasma inside water along with aeration could significantly increase nitrite and nitrate and decreases pH as shown in Table 1.

Depending on the nature of the discharge gas, reactive oxygen species (ROS–ozone, O_3, H_2O_2, $^{\cdot}OH$) and reactive nitrogen species (RNS–ONOO–, NO_3–, NO_2–, and the corresponding acids, nitrogen oxides NO_x) are generated in the PAW (Thirumdas et al., 2018). After the treatment pH of the solution was measured using a pH meter.

Nitrite concentration in PAW was determined using standard USEPA diazotization method and absorbance was read by spectrophotometer at 507 nm (Punith et al., 2019). Nitrate concentrations were measured photometrically by using the Spectroquant nitrate assay kit (Merck Chemicals) adapted to a 96-well plate format, as described in (Tsoukou et al., 2020).

Table 1: pH, nitrate, and nitrite levels of plasma-activated water.

Water sample	pH	Nitrate (mg.kg^{-1})	Nitrite (μg.kg^{-1})
Untreated water	7.58	6.16 ± 0.31	10.12 ± 0.21
10 min	7.28	25.2 ± 0.9	30.56 ± 0.72
20 min	3.46	40.6 ± 1.3	45.5 ± 1.2
30 min	3.16	45.92 ± 1.33	52.32 ± 1.3

The pH value of PAW dropped significantly from 7.58 to 3.16 during 30 minutes of treatment as shown in Table 1, implying that the water has undergone acidification. The reactions taking place between the chemical species formed in the plasma and water result in acidification. In addition, it was known that acidic solutions are highly effective in bacterial inactivation (Soni et al., 2021). Several researchers have studied the impact of acidification to reduce bacterial colony formation (Lin et al., 2019; Soni et al., 2021; Chen et al., 2018). The results show that the concentration of nitrate increases with treatment time (Tabel 1). It is known that a solution containing a nitric ion with a pH below 4 to 5 is antimicrobial. Detection of nitrites and nitrates ions in the PAW is the main evidence for the formation of RNS. Besides ROS, reactive nitrogen species (RNS) such as nitrite and nitrate also play important role in bacteria inactivation. This solution would be a good candidate as fertilizer. Reactions between water gas-phase species lead to the formation of aqueous species like nitrite, nitrate, and hydrogen peroxide.

4 Conclusions

Design and construction of the plasma water activation device have been presented in this article. By creating plasma in water along with aeration, the amount of nitrate and nitrite increases significantly, and also the pH decreases. This solution can be used as fertilizer in agriculture and greenhouses and also as a disinfectant solution that can have many applications in agriculture, medicine, and daily life. Nitrate concentration of PAW increased from 6 for control to 25, 40, and 46 for 10, 20, and 30 minutes of treatment, respectively. The acidity of the solution along with generated ROS and RNS is central to its effectiveness in bacterial inactivation. This result suggests that PAW has suitable characteristics for the inactivation of bacteria and as a medium for the sterilization of medical devices.

Conflict of Interest

The authors declare no potential conflict of interest regarding the publication of this work.

Copyright

References

Bormashenko, E., Grynyov, R., Bormashenko, Y., et al. (2012). Cold radiofrequency plasma treatment modifies wettability and germination speed of plant seeds. *Scientific Reports*, 2(1):1–8.

Chen, T.-P., Liang, J., and Su, T.-L. (2018). Plasma-activated water: antibacterial activity and artifacts? *Environmental Science and Pollution Research*, 25(27):26699–26706.

Foster, J. E. (2017). Plasma-based water purification: Challenges and prospects for the future. *Physics of Plasmas*, 24(5):055501.

Lin, C.-M., Chu, Y.-C., Hsiao, C.-P., et al. (2019). The optimization of plasma-activated water treatments to inactivate Salmonella enteritidis (ATCC 13076) on shell eggs. *Foods*, 8(10):520.

Oh, J.-S., Szili, E. J., Ogawa, K., et al. (2017). UV–vis spectroscopy study of plasma-activated water: Dependence of the chemical composition on plasma exposure time and treatment distance. *Japanese Journal of Applied Physics*, 57(1):0102B9.

Pan, S.-Y., Snyder, S. W., Lin, Y. J., et al. (2018). Electrokinetic desalination of brackish water and associated challenges in the water and energy nexus. *Environmental Science: Water Research & Technology*, 4(5):613–638.

Punith, N., Harsha, R., Lakshminarayana, R., et al. (2019). Plasma activated water generation and its application in agriculture. *Advanced Materials Letters*, 10(10):700–704.

Sakudo, A., Yagyu, Y., and Onodera, T. (2019). Disinfection and sterilization using plasma technology: Fundamentals and future perspectives for biological applications. *International Journal of Molecular Sciences*, 20(20):5216.

Soni, A., Choi, J., and Brightwell, G. (2021). Plasma-activated water (PAW) as a disinfection technology for bacterial inactivation with a focus on fruit and vegetables. *Foods*, 10(1):166.

Thirumdas, R., Kothakota, A., Annapure, U., et al. (2018). Plasma activated water (PAW): Chemistry, physico-chemical properties, applications in food and agriculture. *Trends in Food Science & Technology*, 77:21–31.

Tsoukou, E., Bourke, P., and Boehm, D. (2020). Temperature stability and effectiveness of plasma-activated liquids over an 18 months period. *Water*, 12(11):3021.

RPE | Radiation Physics & Engineering
An International Peer-Reviewed Journal
Published by K.N. Toosi University of Technology
http://rpe.kntu.ac.ir
Research Article

Radiation Physics and Engineering 2023; 4(2):39–44

Investigation of radiation-matter interaction effects on burn process of nonequilibrium deuterium-tritium plasma in inertial confinement fusion approach

Mehdi Nazirzadeh[a,*], Babak Khanbabaei[b], Hamidreza Alborznia[a]

[a] *Department of Physics, Center of Basic Science, Khatam olAnbia-PBU-University, Tehran, Iran*
[b] *School of Physics, Damghan University, P.O. Box 36716-41167, Damghan, Iran*

HIGHLIGHTS

- The burning process of deuterium-tritium fuel and the effect of all the dominant phenomena has been investigated.
- Minimum conditions that are required for starting the thermonuclear reactions in a self-sustaining mode were obtained.
- The effect of the Compton scattering energy from a relativistic point of view is studied.

ABSTRACT

A numerical model was developed and a system of the nonlinear equations of deuterium-tritium burn-up in inertial confinement fusion have been solved to find the minimum conditions which are required for the formation of hot spot and starting the thermonuclear reactions in a self-sustaining mode. The effect of all the dominant phenomena in the nonequilibrium plasma, including the alpha particle energy deposition in the hot spot and transferring to ions and electrons, ions-electron coupling energy, and the main photons-matter interactions, which includes the bremsstrahlung radiation and the Compton scattering, were investigated. By using the Klein-Nishina equation for scattering cross-section of high energy photons, the effects of the photon-matter interactions from a relativistic point of view have also been studied. It was shown that the change of photon distribution shape can have a significant effect on the photon temperature, the photon-electron coupling energy and as a result on the electrons and the ions temperature in a diluted plasma.

KEYWORDS

Compton Scattering Effect
Bremsstrahlung loss
Diluted plasma
Klein-Nishina equation

HISTORY

Received: 29 April 2022
Revised: 27 June 2022
Accepted: 29 July 2022
Published: Spring 2023

1 Introduction

Precise calculation of a physical phenomenon that accrues in fusion medium, plays an essential role in the correct simulation of burn-up process of thermonuclear fuel. The main goal of this paper is to calculate the effect of all the phenomena associated with the absorption and emission of energy, after the nuclear reactions start to happen and the resulting energy releases in the hot spot of inertial confinement fusion (Atzeni and Meyer-ter Vehn, 2004; Lindl, 1998).

According to the Lawson criterion (Lawson, 1957; Zhou and Betti, 2008), when the minimum requirements for initiation of nuclear fusion for an equimolar mixture of deuterium and tritium were prepared, the ignition in the hot spot starts, and the burning wave propagates in the surrounding dense fuel (Christopherson et al., 2020). After deposition of alpha particle energy in the hot spot, it is instantaneously transferred to ions and electrons in certain proportions (Fraley et al., 1974). It was assumed that the ignition model is volume like, the burning medium is infinite and the electrons and ion distribution function is Maxwellian throughout the burn and the interactions between them are in the form of classic Coulomb scattering (Spitzer, 2006). Electron-photons coupling can vary depending on the plasma regime. If the plasma regime is optically thick throughout the burn, the photon distribution is blackbody or Planckian, and the plasma can be described by three temperature model, while if plasma is optically thick and at a certain energy, the photon distribution changed to Bose-Einstein, and plasma regime is also changed to optically thin. In this case, a new pho-

*Corresponding author: m.nazirzadeh@khadu.ac.ir

https://doi.org/10.22034/rpe.2022.339578.1083
https://dorl.net/dor/20.1001.1.26456397.2023.4.2.6.2

ton temperature is defined, which differs from Planckian radiation temperature (Molvig et al., 2009). In the Bose-Einstein distribution, the Compton scattering can boost the photons to high energy without changing the photons numbers. If the scattering calculation is done with nonrelativistic approximation, the energy exchange rate between electrons and photons is not completely precise. So we should consider the Compton scattering from a relativistic point of view which its results have well compatible with Monte Carlo calculations (Cooper, 1971; Corman, 1970).

In this paper, the photon-electron coupling and their effects on the burning process of deuterium-tritium in both relativistic and nonrelativistic cases have been studied.

2 Radiation field calculation

In order to explain the photon-matter interaction in plasma, the equation of the time evolution of photon number density which is called the photon kinetic equation, is used as (Cooper, 1971; Corman, 1970; Rose, 2013, 1996; ZelDovich and Levich, 1969):

$$\rho_\varepsilon \frac{\partial n_E}{\partial t} = \nu_C N_{\gamma 0}(T_e) \frac{T_e}{m_e c^2} \frac{\partial}{\partial \varepsilon} \Big[\varepsilon^4 \big(n_\varepsilon (1+n_\varepsilon) \big) + \frac{\partial}{\partial \varepsilon} n_\varepsilon \Big] + \Big\{ \nu_\beta n_e \sqrt{\frac{m_e c^2}{2T_e}} \frac{\mathrm{e}^{-\varepsilon/2} K_0(\varepsilon/2)}{\varepsilon} - \nu_\beta \rho_\varepsilon \frac{n_e}{N_{\gamma 0}(T_e)} \sqrt{\frac{m_e c^2}{2T_e}} \frac{\mathrm{e}^{-\varepsilon/2} K_0(\varepsilon/2)(\mathrm{e}^\varepsilon - 1)}{\varepsilon^3} n_E \Big\} \tag{1}$$

In Eq. (1), ε is the photon energy, c is the speed of light, $\rho_\varepsilon = \dfrac{8\pi\, T_e^3 \varepsilon^2}{h^3 c^3}$ is the density of states, $\nu_C = c\,\sigma_T n_e$ is the basic Compton rate, $\sigma_T = \dfrac{8\pi\, r_e^2}{3}$ is the Thomson cross-section, $N_{\gamma 0}(T_e) \equiv \dfrac{8\pi\, T_e^3}{h^3 c^3}$, and $\nu_\beta = \dfrac{4}{\pi^{3/2}} Z_{\text{eff}} \dfrac{e^2}{\hbar c} \nu_C$. The relation between photon Bose-Einstein distribution and photon particle and energy density can be expressed as (Molvig et al., 2009):

$$\begin{aligned} E_R &= \frac{8\pi T_e^4}{h^3 c^3} \int_0^\infty \mathrm{d}\varepsilon\, \varepsilon^3 \frac{1}{\mathrm{e}^{\alpha+\varepsilon/\gamma} - 1} \\ &= \frac{8\pi T_p^4}{h^3 c^3} \int_0^\infty \mathrm{d}y\, y^3 \frac{1}{\mathrm{e}^{\alpha+y} - 1} \\ &= \frac{8\pi T_p^4}{h^3 c^3} F(\alpha) \end{aligned} \tag{2}$$

$$N_\gamma = \frac{8\pi T_e^3}{h^3 c^3} \int_0^\infty \mathrm{d}\varepsilon\, \varepsilon^3 \frac{1}{\mathrm{e}^{\alpha+\varepsilon/\gamma} - 1} \tag{3}$$

The Bose-Einstein form of photon distribution in zero-order can be expressed as (Pathria, 2016):

$$n_E^0 = \frac{1}{\mathrm{e}^{(\mu+E)/T_p} - 1} = \frac{1}{\mathrm{e}^{\alpha+\varepsilon/\gamma} - 1} \tag{4}$$

where μ is chemical potential, α is dilution factor, T_p is the photon temperature, $\gamma = \dfrac{T_p}{T_e}$ is the ratio of photon temperature to electron temperature and $\varepsilon \equiv \dfrac{E}{T_e}$ is the energy variable.

The first term of the right-hand side of Eq. (1) represents the Compton operator, and the second term shows the bremsstrahlung operators. The power radiated power from electrons to photons can be extracted from these operators when they are calculated for the zero-order photon distribution as (Molvig et al., 2009):

$$\begin{aligned} P_{rad} =& P_B + P_C = \nu_C n_e \frac{4}{\pi^{3/2}} Z_{\text{eff}} \frac{e^2}{\hbar c} \sqrt{\frac{T_e m_e c^2}{2}} \\ &\times \Big[\int_0^\infty \mathrm{d}\varepsilon\, \mathrm{e}^{-\varepsilon/2} K_0\big(\frac{\varepsilon}{2}\big) \frac{(\mathrm{e}^{\alpha+\varepsilon/\gamma} - \mathrm{e}^{\varepsilon})}{\mathrm{e}^{\alpha+\varepsilon/\gamma} - 1} \Big] \\ &+ \nu_C N_{\gamma 0}(T_e) \big(1 - \frac{1}{\gamma}\big) \frac{T_e^2}{m_e c^2} \\ &\times \int_0^\infty \mathrm{d}\varepsilon\, \varepsilon \frac{\partial}{\partial \varepsilon} \Big(\varepsilon^4 \frac{\mathrm{e}^{\alpha+\varepsilon/\gamma}}{\big(\mathrm{e}^{\alpha+\varepsilon/\gamma} - 1\big)^2} \Big) \end{aligned} \tag{5}$$

where K_0 is the modified Bessel function of the second kind. In Eq. (5), the first term of right-side is the bremsstrahlung power, and the second term is the Compton power that can be replaced by

$$P_c = \nu_C\, 4\, E_R \frac{(T_e - T_p)}{m_e c^2} \tag{6}$$

where E_R is the radiation energy density was defined in Eq. (2).

3 Klein-Nishina scattering cross-section

When the energy of photons is comparable or greater than the rest mass of energy of the electron ($m_{0e}c^2$), a quantum treatment is necessary, and the Klein-Nishina formula must be used to calculate of photons cross-section, while for photons energy much smaller than the rest mass of energy of the electron, $h\nu << m_{0e}c^2$, the scattering of photons is described by Thomson formula. According to the Klein-Nishina equation, when the photon energy increases, its cross-section or its collision probability with electrons is decreased. The Klein-Nishina scattering cross section per steradian of solid angle Ω can be written as (Nishina, 1929)

$$\begin{aligned} \frac{\mathrm{d}\sigma}{\mathrm{d}\Omega} =& r_0^2 \big(\frac{1+\cos^2\theta}{2}\big) \frac{1}{\big(1 + h\nu(1-\cos\theta)\big)^2} \\ &\times \Big[\frac{(h\nu)^2 \big(1-\cos\theta\big)^2}{\big(1+\cos^2\theta\big)\big[1 + h\nu(1-\cos\theta)\big]} + 1 \Big] \\ =& \frac{1}{2} r_0^2 \Big(\frac{k}{k_0}\Big)^2 \Big(\frac{k}{k_0} + \frac{k_0}{k} - \sin^2\theta\Big) \end{aligned} \tag{7}$$

where $k_0 = \dfrac{h\nu_0}{m_e c^2}$, $k = \dfrac{h\nu}{m_e c^2}$, and $r_0 = \dfrac{e^2}{4\pi\,\varepsilon_0\, m_{0e}\, c^2}$ is classical electron radius, $h\nu_0$ is the energy of the incident photon, $h\nu$ is the energy of the scattered photon, m_e is the rest mass of the electron, and c is the speed of light. When a high-energy photon collides with an electron, for accuracy of calculations, it is necessary to use a relativistic approximation for describing the Compton scattering phenomenon. According to The Fokker-Planck equation (Cooper, 1971), a correction factor $\varphi_R(\varepsilon)$ applies on the

Compton scattering operator in plasma in a relativistic case

$$C_C(T_e,n_\varepsilon)=\nu_C N_{\gamma 0}(T_e)\frac{T_e}{m_e c^2}\frac{\partial}{\partial\varepsilon}\times\Big[\varphi_R\big(\frac{\varepsilon}{\gamma}\big)\varepsilon^4\Big(n_\varepsilon\big(1+n_\varepsilon\big)+\frac{\partial}{\partial\varepsilon}n_\varepsilon\Big)\Big] \tag{8}$$

Threfore, the Compton scattering power relation in Eq. (6) is changed as (Molvig et al., 2009; Cooper, 1971):

$$\begin{aligned}P_C&=\nu_C\,4\,E_R\,\frac{(T_e-T_p)}{m_e c^2}\,\alpha_R\\&=\frac{1}{4F(\alpha)}\nu_C\,E_R\,\frac{(T_e-T_p)}{m_e c^2}\\&\times\int_0^\infty \mathrm{d}y\;y^4\;\varphi_R(y)\;\mathrm{csc}\,h^2\big(\frac{a+y}{2}\big)\end{aligned} \tag{9}$$

$$\varphi_R(y)=\frac{1+\dfrac{a}{1+by}}{1+gy+\sigma y^2} \tag{10}$$

where

$$a=\frac{5}{2}\Big(\frac{T_e}{m_e c^2}\Big)+\frac{15}{8}\Big(\frac{T_e}{m_e c^2}\Big)^2\Big(1-\frac{T_e}{m_e c^2}\Big) \tag{11}$$

$$\begin{aligned}b&=0.02\;T_p\,,\\g&=0.009\;T_p\,,\\\sigma&=0.0000042\;T_p^2\end{aligned} \tag{12}$$

Equation (6) is the relativistic form of the Compton scattering energy, and in the following section, we use this relation in DT burn-up equations.

4 Nuclear Ignition and Burn-up Equation

In the four temperature model, the areal density- dependent calculations of the fusion process of DT fuel in an infinite medium such as ion-electron collisions, alpha particle energy deposition, radiation-matter interaction including, the Compton scattering and the bremsstrahlung radiation, were performed. The nuclear reactions are considered in the calculation as follows:

$$\begin{aligned}&{}_1D^2+{}_1T^3\longrightarrow{}_2He^4+{}_0n^1+17.6\text{ MeV}\\&{}_1D^2+{}_1D^2\longrightarrow{}_2He^3+{}_0n^1+3.27\text{ MeV}\\&{}_1D^2+{}_1D^2\longrightarrow{}_1T^3+{}_1p^1+4.03\text{ MeV}\end{aligned} \tag{13}$$

We consider the 4-T model (Molvig et al., 2009) for the description of the plasma, in which its components have different temperatures in a nonequilibrium situations. In the 4T model, the radiation temperature is distinguished from photon temperature when the plasma regime undergoes a transition from optically thick to optically thin. The equation of electrons revolution with time are shown as (Molvig et al., 2009):

$$\begin{aligned}\frac{3}{2}n_e\frac{\partial T_e}{\partial t}&=E_\alpha\big(1-f_{\alpha i}\big)\,n_i^2\langle\sigma\nu\rangle+P_{ie}-P_C-P_B\\P_{ie}&=\frac{6}{\sqrt{\pi}}\,\nu_C\,n_i\Big[\frac{m_e}{m_D}+\frac{m_e}{m_T}+4\Big(\frac{n_{io}-n_i}{n_i}\Big)\frac{m_e}{m_\alpha}\Big]\\&\times\Big(\frac{m_e c^2}{2T_e}\Big)^{3/2}\ln(\Lambda)\,(T_i-T_e)\\\ln(\Lambda)&=25.127-\ln\Big(\frac{\sqrt{n_e}}{1000\,T_e}\Big)\\f_{\alpha i}&=\frac{T_e}{T_e+32}\end{aligned} \tag{14}$$

where $f_{\alpha i}$ is the fraction of alpha particle energy, E_α, deposited in the hot spot which transferred to ions, $\langle\sigma\nu\rangle$ is the reaction rate and $\ln(\Lambda)$ is the Coulomb logarithm which is defined as the ratio of Debye screening length to the minimum value of the impact parameter in Coulomb collision processes (Mulser et al., 2014).

The equation of ions revolution with time are shown as (Molvig et al., 2009):

$$\frac{3}{2}\big[n_{io}+n_i\big]\frac{\partial T_i}{\partial t}=\big(E_\alpha f_{\alpha i}+\frac{3}{2}T_i\big)\,n_i^2\,\langle\sigma\nu\rangle-P_{ei} \tag{15}$$

where $n_{io}=\dfrac{n_e}{2}$ is the constant initial ion density.

According to Lawsons criterion in inertial confinement fusion, we need to compute the minimum value for the product of initial mass density and initial hot spot radius ($\rho_0 r_0$). So it is required to change the variable from time to areal density ($\rho_0 r_0$), and use Frolovs approach (Frolov et al., 2002), which have been shown in our earlier work (Nazirzadeh et al., 2015, 2017) thus the Eqs. (14) and (15) are changed as

$$\frac{\mathrm{d}T_e}{\mathrm{d}x}=-\frac{3}{x}T_e+\frac{q_e(x,T_i,T_e,T_p,T_R)}{C_{Ve}\,V_{max}} \tag{16}$$

$$\frac{\mathrm{d}T_i}{\mathrm{d}x}=-\frac{3}{x}T_i+\frac{q_i(x,T_i,T_e)}{C_{Vi}\,V_{max}} \tag{17}$$

where $x=\rho_0 r$ is areal density, C_{Ve} and C_{Vi} are specific heat capacity of electrons and ions respectively, $V_{max}=\dfrac{\mathrm{d}r}{\mathrm{d}t}$ is the speed of hot spot expansion, q_e and q_i are the net energy release rate for electrons and ions, which are represented respectively in Eq. (16) and Eq. (17) as

$$q_e=E_\alpha\big(1-f_{\alpha i}\big)\,n_i^2\,\langle\sigma\nu\rangle+P_{ie}-P_C-P_B \tag{18}$$

$$q_i=\big(E_\alpha f_{\alpha i}+\frac{3}{2}T_i\big)\,n_i^2\,\langle\sigma\nu\rangle-P_{ie} \tag{19}$$

where n_i is the ions number density which its variation with areal density for both the deuterium and tritium can be expressed as

$$\frac{\partial n_i}{\partial x}=-\frac{n_i^2\,\langle\sigma\nu\rangle}{\rho_0 V_{max}} \tag{20}$$

The time evolution of radiation energy in Eq. (2) can be shown as (Molvig et al., 2009):

$$\frac{\partial E_R}{\partial t}=\frac{32\pi}{h^3c^3}T_P^3\,F(\alpha)\frac{\partial T_P}{\partial t}+\frac{8\pi}{h^3c^3}T_P^4\frac{\mathrm{d}F}{\mathrm{d}\alpha}\frac{\partial\alpha}{\partial t} \tag{21}$$

When the dilution factor does not change with time, $\frac{\partial \alpha}{\partial t} = 0$, photons retain their Planckian distribution shape, and time variation of radiation temperature is expressed as

$$\frac{\mathrm{d}T_R}{\mathrm{d}t} = \frac{h^3 c^3}{32\,\pi\,T_P^3\,F(0)}\frac{\partial E_R}{\partial t} \tag{22}$$

otherwise, the time variation of photon temperature can be written as (Molvig et al., 2009):

$$\frac{\partial T_P}{\partial t} = \frac{h^3 c^3}{32\pi\,T_P^3\,F}\frac{\partial E_R}{\partial t} - \frac{T_P}{4}\frac{\mathrm{d}\,\ln F}{\mathrm{d}\alpha}\frac{\partial \alpha}{\partial t} \tag{23}$$

By changing the variable from time to areal density and use Frolovs approach, Eq. (22) and Eq. (23) are represented as (Nazirzadeh et al., 2015, 2017):

$$\frac{\mathrm{d}T_R}{\mathrm{d}x} = -\frac{3}{4x}T_r + \frac{q_r(x,T_e,T_R)}{C_{Vr}\,V_{max}} \tag{24}$$

$$\frac{\partial T_P}{\partial x} = -\frac{3}{4x}T_P - \frac{1}{4}T_P\frac{\partial F}{\partial \alpha}\frac{\partial \alpha}{\partial x} + \frac{q_P(x,T_e,T_P)}{\frac{32\pi}{h^3c^3}\,T_P^3\,F(\alpha)\,\rho_0\,V_{max}} \tag{25}$$

where $\frac{\partial \alpha}{\partial x}$ is the variation of dilution factor with respect to areal density that can be expressed as (Molvig et al., 2009; Nazirzadeh et al., 2015):

$$\frac{\partial \alpha}{\partial x} = \Big(-\dot{N}_B + \frac{I_1(\alpha)}{4F(\alpha)}\frac{P_{rad}}{T_P}\Big) \times \frac{1}{\rho_0\,V_{max}\,N_{\gamma 0}\Big(I_0(\alpha) - \frac{I_1^2(\alpha)}{4F(\alpha)}\Big)} \tag{26}$$

In the following section, the rules of influential phenomena that participate in the fusion such as ion-electron coupling power, P_{ie}, the Compton scattering power, P_c, in two cases: relativistic and nonrelativistic, the division of alpha particle energy transferred to ions and electrons that were each expressed by known formulas and the bremsstrahlung power were explicitly investigated.

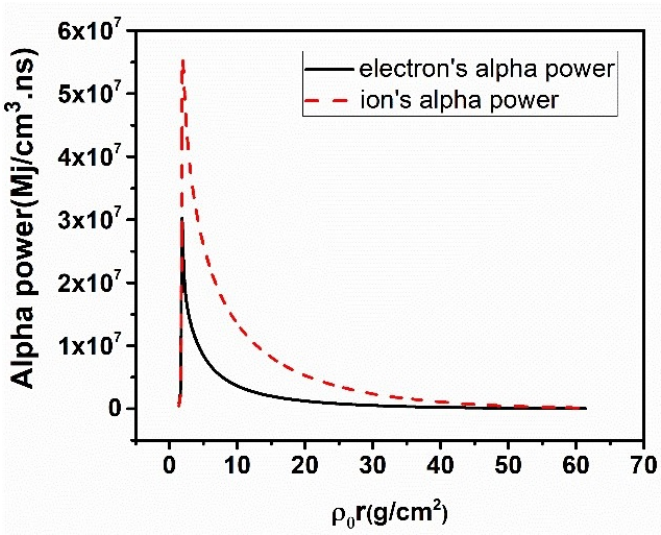

Figure 1: The amount of alpha energy transferred to ions and electrons.

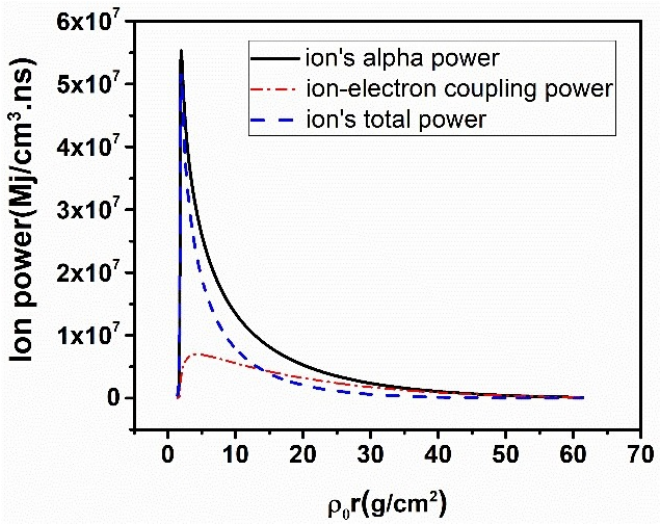

Figure 2: The total ion energy is consists of ion alpha energy and ion-electron coupling energy.

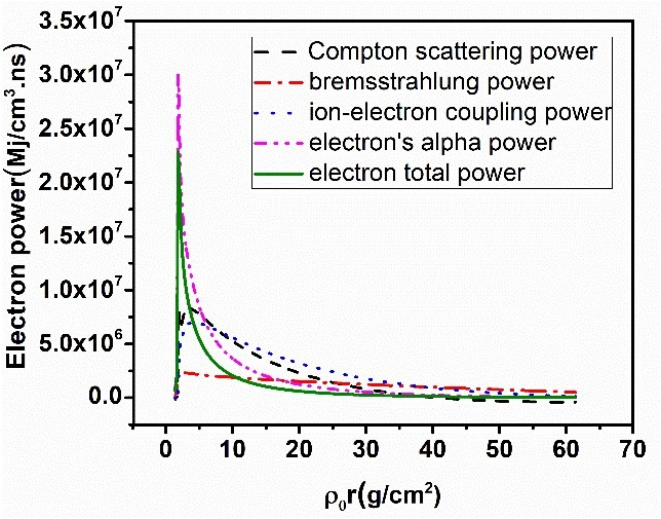

Figure 3: The total electron energy is consists of electron alpha energy and ion-electron coupling energy, the Compton scattering energy, and the bremsstrahlung radiation energy.

5 Results and discussion

In this paper, a Fortran program was used to solve a set of six coupled nonlinear differential equations of deuterium-tritium burn in a four-temperature model. These differential equations include four plasma components (ions, electrons, radiation, and photons), ions number density, and dilution factor revolutions with respect to areal density.

The initial mass density for both deuterium and tritium were chosen to $\rho_0 = 100$ g.cm^{-3}, so the initial ions density is $n_i = 1.2044 \times 10^{25}$ cm^{-3}. The starting ion and electron temperature is set to 5 keV , and the initial photon and radiation temperature were assumed to 2.5 keV.

In Fig. 1, the division of alpha energy which transferred to ions and electrons, was shown. It was assumed that all the neutron energy produced in the fusion reactions is wasted from the system. In Fig. 2, the factors that

effects the energy of the ions are depicted. A portion of alpha energy which is transferred to ions and ion-electron coupling energy, are the sources of ions energy, in which the former plays a positive rule, and the latter has a negative effect on ions energy. In Fig. 3, the total energy of electrons is represented, which is consisted of electron alpha energy, ion-electron coupling energy, which both have the positive effect on electron energy, and the Compton scattering energy, and the bremsstrahlung radiation energy, which have negative effects on the electron energy.

It was assumed that the burning process is uniformly in an infinite medium and plasma is in an optically thick regime; in other words, photons distribution is initially Planckian with no dilution factor ($\alpha = 0$), then at certain photon energy when $\alpha > 0$, the plasma undergoes a transition to the optically thin regime, and photons distribution is changed to Bose-Einstein. In an optically thin regime with fixed radiation energy, the dominated photon-matter interaction is the Compton scattering which increases the photon temperature, so for high energy photons, it is necessary to consider the Compton scattering relativistically. In this case, the Compton scattering probability of high energy photons with electrons is smaller than that of the nonrelativistic case.

In Fig. 4, the domination of photon temperature in the relativistic case in comparison to the nonrelativistic case is represented. It was clear that with a low scattering cross-section, the photon temperature decreases less, and as a result, the Compton scattering energy for high energy photons is smaller than that of low energy photons, which is represented in Fig. 5. The bremsstrahlung radiation is almost the same in both models. In Fig. 6, the total radiation power, which is consisted of the Compton scattering and the bremsstrahlung radiation, was shown. As is clear if the burning calculation was done from a relativistic point of view, the total radiation from the hot spot is decreased in comparison to the nonrelativistic case.

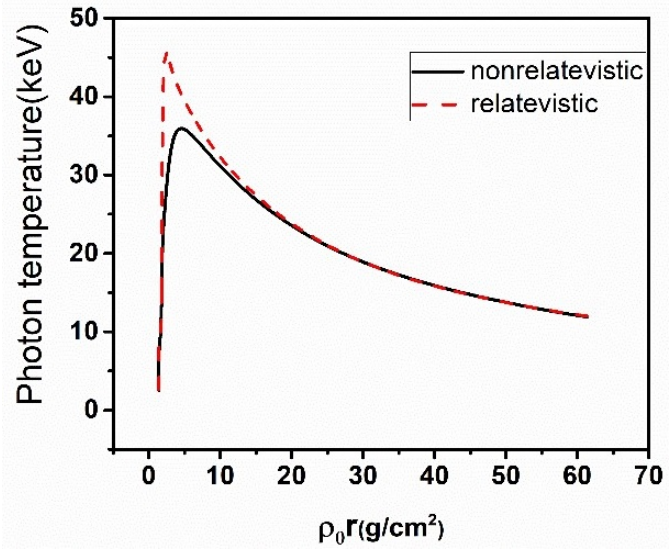

Figure 4: Photon temperature in relativistic and nonrelativistic cases. High energy photons interactions with electrons is decreased.

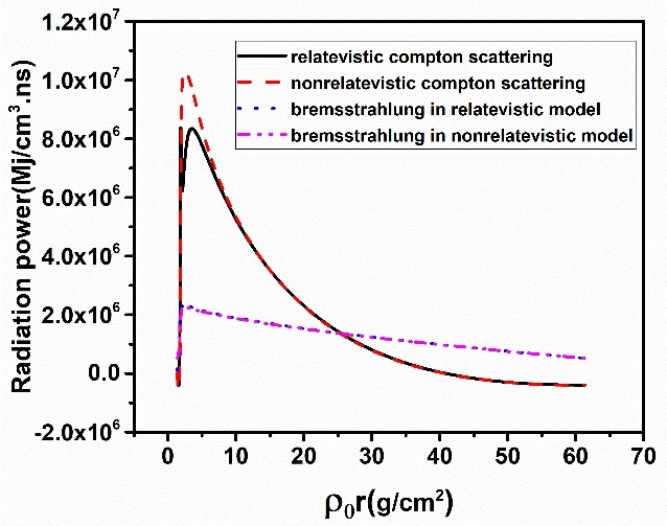

Figure 5: The Compton scattering power and bremsstrahlung radition in relativistic and nonrelativistic cases.

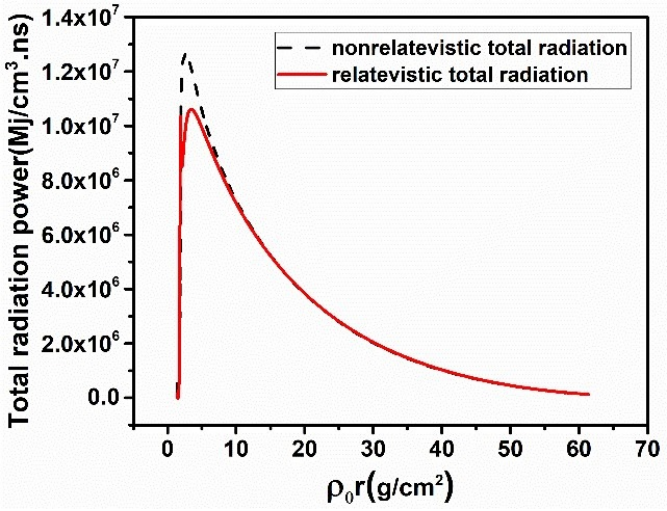

Figure 6: Total radiation power in the relativistic and nonrelativistic cases.

6 Conclusions

In this paper, by using a 4T model, the burning process of deuterium-tritium fuel and the effect of all the dominant phenomena involved in the fusion, including the alpha particle energy transferring to ions and electrons, ion-electron coupling energy, the Compton scattering energy, and the bremsstrahlung radiation in an infinite medium has been investigated.

The effect of the Compton scattering energy from a relativistic point of view is also studied. It was shown that in a diluted plasma, when photons distribution is changed from blackbody radiation to Bose-Einstein, the Compton scattering heats photons to high temperature without change the photons number. So by applying the relativistic model of the Compton scattering in the fusion burn-up calculations, fusion hot spot will stay more time in self-sustaining mode.

Conflict of Interest

The authors declare no potential conflict of interest regarding the publication of this work.

Copyright

References

Atzeni, S. and Meyer-ter Vehn, J. (2004). *The physics of inertial fusion: beam plasma interaction, hydrodynamics, hot dense matter*, volume 125. OUP Oxford.

Christopherson, A., Betti, R., Miller, S., et al. (2020). Theory of ignition and burn propagation in inertial fusion implosions. *Physics of Plasmas*, 27(5):052708.

Cooper, G. (1971). Compton Fokker-Planck equation for hot plasmas. *Physical Review D*, 3(10):2312.

Corman, E. G. (1970). Relativistic Compton energy exchange. *Physical Review D*, 1(10):2734.

Fraley, G., Linnebur, E., Mason, R., et al. (1974). Thermonuclear burn characteristics of compressed deuterium-tritium microspheres. *The Physics of Fluids*, 17(2):474–489.

Frolov, A. M., Smith Jr, V. H., and Smith, G. T. (2002). Deuterides of light elements: low-temperature thermonuclear burn-up and applications to thermonuclear fusion problems. *Canadian Journal of Physics*, 80(1):43–64.

Lawson, J. D. (1957). Some criteria for a power producing thermonuclear reactor. *Proceedings of the Physical Society. Section B*, 70(1):6.

Lindl, J. (1998). Inertial Confinement Fusion Springer-Verlag. *New York*, 11.

Molvig, K., Alme, M., Webster, R., et al. (2009). Photon coupling theory for plasmas with strong Compton scattering: Four temperature theory. *Physics of Plasmas*, 16(2):023301.

Mulser, P., Alber, G., and Murakami, M. (2014). Revision of the Coulomb logarithm in the ideal plasma. *Physics of Plasmas*, 21(4):042103.

Nazirzadeh, M., Ghasemizad, A., and Khanbabei, B. (2015). Determination of deuterium–tritium critical burn-up parameter by four temperature theory. *Physics of Plasmas*, 22(12):122709.

Nazirzadeh, M., Khanbabaei, B., and Ghasemizad, A. (2017). The investigation of inertial fusion burning requirements of deuterium-helium3 in degenerate plasma. *Physics of Plasmas*, 24(8):082708.

Nishina, Y. (1929). Polarisation of Compton scattering according to Dirac's new relativistic dynamics. *Nature*, 123(3097):349–349.

Pathria, R. K. (2016). *Statistical mechanics*. Elsevier.

Rose, S. (1996). Compton scattering in inertial confinement fusion plasmas. *Journal of Quantitative Spectroscopy and Radiative Transfer*, 55(6):707–713.

Rose, S. (2013). Electron–positron pair creation in burning thermonuclear plasmas. *High Energy Density Physics*, 9(3):480–483.

Spitzer, L. (2006). *Physics of fully ionized gases*. Courier Corporation.

ZelDovich, Y. B. and Levich, E. (1969). Bose condensation and shock waves in photon spectra. *Sov. Phys. JETP*, 28(11):1287.

Zhou, C. and Betti, R. (2008). A measurable Lawson criterion and hydro-equivalent curves for inertial confinement fusion. *Physics of Plasmas*, 15(10):102707.

RPE | Radiation Physics & Engineering
An International Peer-Reviewed Journal
Published by K.N. Toosi University of Technology
http://rpe.kntu.ac.ir
Research Article

Radiation Physics and Engineering 2023; 4(2):45–51

Calculation of the role of Wigner energy in decontamination of Cs-137 from irradiated Graphite pores

Mohammad Nikoosefat[a,*], Ardeshir Bagheri[a], Hamidreza Shakur[a], Zahra Shahbazi Rad[b], Nabi Javadi[c]

[a] *Nuclear Physics Group, Faculty of Basic Science, Comprehensive University of Imam Hossein, Tehran, Iran*
[b] *Faculty of Nuclear Engineering, University of Shahid Beheshti, Tehran, Iran*
[c] *Chemistry Group, Faculty of Basic Science, Comprehensive University of Imam Hossein, Tehran, Iran*

HIGHLIGHTS

- The decontamination of Cs-137 from irradiated graphite is investigated using the plasma-sputtering method.
- The results show that the decrease in radiation pollution depends on the release of Wigner energy.
- This study demonstrates the benefits of using noble gases as a plasma feed gas in the plasma decontamination process.
- The results can be used to decontamination of various types of irradiated porous materials used in nuclear systems.
- Researchers of radiation safety, nuclear waste management and nuclear decommissioning will be interested in the results.

ABSTRACT

During the operation of Graphite -fuel HTGR (High-Temperature Gas-cooled Reactor) nuclear reactors, Graphite used as a neutron moderator, is irradiated and has a variety of contaminants (such as Cs-137, Co-60, and Sr-90) and due to industrial and environmental considerations, decontamination of irradiated Graphite is very important. In this study, the decontamination of Cs-137 trapped in Graphite pores of Graphite -fuel (HTGR) nuclear reactors has been analyzed. The proposed method for decontamination of irradiated Graphite surfaces is the thermal plasma-sputtering method with noble feed gases, which are used to reduce the risk of radioactive Graphite waste and in this regard, a mathematical model was developed to describe the process of decontamination of irradiated Graphite, which is prone to release Wigner energy due to defects and torsion caused by radiation. The results show that the decrease in radiation pollution of irradiated Graphite waste and various parameters of its decontamination process depend on the release of Wigner energy. The results obtained are in good agreement with the other researchers results.

KEYWORDS

Decontamination
HTGR Reactor
Irradiated Graphite waste
Radionuclides
Wigner Energy
Mathematical model

HISTORY

Received: 2 May 2022
Revised: 2 August 2022
Accepted: 15 August 2022
Published: Spring 2023

1 Introduction

The decommissioning and dismantling of old and worn-out nuclear equipment are as important as the commissioning of nuclear power plants and new nuclear sites (Laraia, 2012; IAEA, 2001). In 2008, the International Atomic Energy Agency published a report in which the high impact of using dry plasma decontamination method in the process of decommissioning of the nuclear equipment is mentioned (IAEA, 2008).

1.1 The role of Graphite in the high-temperature gas-cooled reactor (HTGR)

The HTGR nuclear reactor is a generation IV nuclear reactor that uses Graphite as a neutron moderator, the Uranium fuel cycle, and Helium as coolant. During the operation of HTGR (High Temperature Gas Reactors) nuclear reactor, Graphite is irradiated and after a while, Graphite loses its original properties and needs to be decontaminated or replaced. In addition, after the useful life of the HTGR reactor and during its decommissioning process, in order to comply with radiation and environmental protocols, irradiated Graphite must first be decontaminated and then scrapped (Kuijper et al., 2006; Sato and Yan, 2019). In 2020, Chinese researchers published a report on the decontamination of Graphite surfaces using plasma method in which, factors related to plasma ability to decontaminate radioactive agents from Graphite surfaces were investigated and it acknowledges that the

*Corresponding author: m.nikoosefat@ihu.ac.ir

https://doi.org/10.22034/rpe.2022.340253.1084
https://dorl.net/dor/20.1001.1.26456397.2023.4.2.8.4

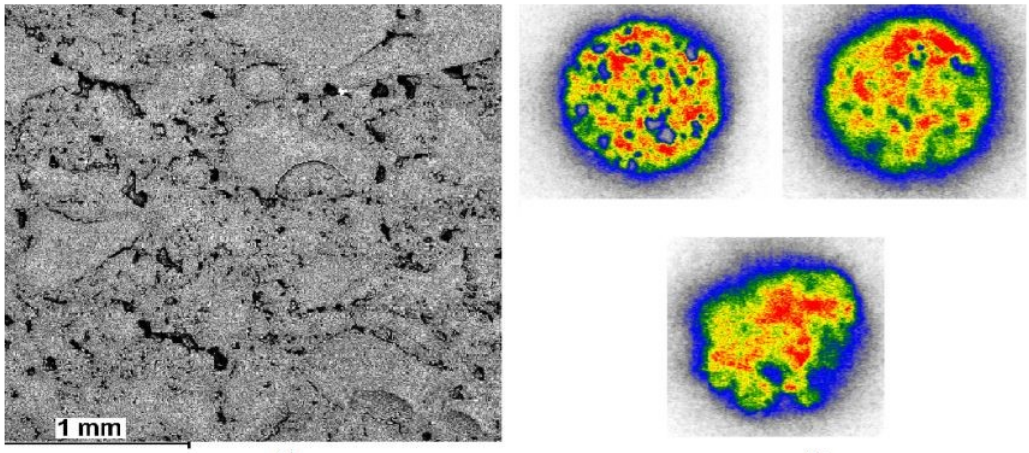

Figure 1: a) SEM images of polished irradiated Graphite; b) Autoradiographic images of irradiated Graphite in which, red, blue, and white represent high, medium, and low activity, respectively (Bespala et al., 2019).

plasma method is very effective, inexpensive and promising. Bushuev et al. (Bushuev et al., 2003) presented the results of a study of bushing contamination in Graphite -uranium reactors. These radioactive contaminants are including the radioisotopes of H-3, C-14, Fe-55, Co-60, and etc; and fission fragments such as Ru-106, Sb-125, Ba-133, Cs-137, Eu-154, Eu-155, and the transuranic elements such as Am-241, Am-243, Cm-244, etc. In the meanwhile, the most active radioisotopes are Cs-137, Co-60, Sr-90, Cl-36, and H-3 (Bespala et al., 2018; Pavliuk et al., 2018b). In 2016, the international project of the GRAPA (Irradiated Graphite Processing Approaches) was implemented by the IAEA (International Atomic Energy Agency) with the participation of various countries in which, its content is about the upcoming and new approaches to irradiated Graphite processing (Wickham et al., 2017). Modern knowledge offers a variety of methods for the treatment of Graphite radioactive waste (GRW) and in the meanwhile, the plasma sputtering method using noble feed gas is very effective in decontamination of Cs-137 from irradiated Graphite surfaces (Theodosiou et al., 2018; Vulpius et al., 2013; Fachinger et al., 2008; Dunzik-Gougar and Smith, 2014).

Also it has been shown that Cesium, cobalt, and strontium radionuclides are to be metallic during reactor operation and they have no fixed molecular bond with each other or with Graphite molecules and they are trapped in the Graphite pores and this lack of molecular binding is a good motivation and physical basis for researchers to study the process of decontamination using plasma-sputtering method; Because contamination molecules do not chemically bond with Graphite substrate molecules and thus, we don't need to use plasma-chemical methods for decontamination (Pavliuk et al., 2018a; Theodosiou et al., 2018). Plasma processing is one of the promising methods for decontamination of irradiated Graphite in the nuclear industry and therefore, the simulation and the mathematical study of this process cause that, in addition to detailed analysis of decontamination operations, we minimize the potential effect of the radiation hazards during the actual experimental operation process (Bespala et al., 2016).

1.2 Plasma-sputtering method in decontamination of surfaces

One of the important advantages of plasma in the surface-processing is its major role in minimizing the adverse effects of industrial activities on the environment. Many physical and chemical phenomena are often involved in plasma etching. One of the mechanisms of plasma etching is the etching by sputtering method. In the sputtering method, the positive ions are present throughout the plasma sheath and due to their inherent escape, they accelerate to the boundaries of the plasma and they strike the contamination of substrates with high kinetic energy and some of their energies are transferred to the atoms of the surface contamination, which will lead to the evaporation (or sublimation) of the contamination. This process is different from other mechanisms because its mechanism is mechanical (not chemical), i.e. their escape conditions are provided only by applying force and transferring mass and energy to surface molecules (Auciello et al., 2012). In the present study, the decontamination of Cs-137 from irradiated Graphite is investigated and analyzed using the plasma-sputtering method in which, Thermodynamic processes of heat and mass transfer during the interaction and effect of plasma on the surfaces of irradiated Graphite are analyzed.

2 Methods

2.1 Selection of reference irradiated Graphite sample

In reference (Bespala et al., 2019), a Graphite sample (sampling from Graphite stack) of Seversk Uranium-Graphite reactor in the Tomsk region of Russia is experimentally analyzed. This Graphite sample, which has been irradiated in the reactor core for 9 years and was experimentally studied by Russian researchers in 2019, is used

as a reference sample for thermodynamic analysis in this study.

Figure 1-a shows the SEM image of the irradiated Graphite in which, gray, black, and white indicate the irradiated Graphite, pores, and non-carbon solid impurities respectively. The white dots indicate the presence of fission products and neutron activation products at the Graphite surface. However, radioactive contaminants can be located inside the Graphite pores and not appear in the SEM image (Bespala et al., 2019; Bushuev et al., 2015). Radionuclides are impurities that can penetrate into the Graphite substrate and disperse into its pores and we also know that one of the challenges of technology is to remove contaminations from porous materials. The decontamination process requires almost complete removal of contaminants from the Graphite pores and for this purpose, arc discharge plasma and non-thermal atmospheric pressure plasma (NTP) can be used to process irradiated Graphite. In order to reduce the specific activity of irradiated Graphite and also reduce its potential hazards, it is recommended that its heat treatment be performed in an inert gas environment. When a plasma gas stream comes in contact with the Graphite substrate, the Graphite will heat up and when the surface reaches the boiling point of radioactive contaminants, evaporation or sublimation of radionuclides is possible under certain thermodynamic conditions. In most of the experimental findings of other researchers, the results of analysis of the SEM images show that Graphite has an integrated porous structure and most of the non-carbon pollutants are inside its pores.

2.2 Thermodynamic analysis

In this study, in order to thermodynamic analysis of the Graphite decontamination process, we consider the geometry in such a way that a thin layer of the Cs-137 radionuclides are located in the one of the Graphite pores. We also assume that in during the mathematical modeling process, Cs-137, Co-60, and Sr-90 radiation pollutants dont mix with each other. Thus, in addition to simplifying the form of differential equations, we get closer to the real physical conditions (Bespala et al., 2018, 2019). In references (Bespala et al., 2019; Kane et al., 2013; Barbin et al., 2015; Bespala et al., 2017, 2016; Pavliuk et al., 2018b) efforts for mathematical modeling of thermal processing of the irradiated Graphite are presented and in some of them, the release of Wigner energy is also considered. In our proposed geometry for the analysis in this study, it is assumed that an atmospheric pressure plasma jet with argon as feed gas moves along the Graphite specimen that has a porous surface (Fig. 2).

3 Results and discussion

3.1 Thermodynamic analysis

The plasma decontamination process of irradiated Graphite confirms the effectiveness of the plasma flow on the Graphite surface, which leads to the sublimation of the radioactive contaminants that are trapped in the Graphite pores. When irradiated Graphite is exposed to argon plasma flow, we can get a fairly good estimate of the chemical composition produced (Bespala et al., 2018, 2019). For this purpose, in this study, TERRA software package was used for modeling and thermodynamic analysis of reactions, in which the capabilities of the main version of this software package are mentioned in references (Aref'yev et al., 1974; Young, 1975).

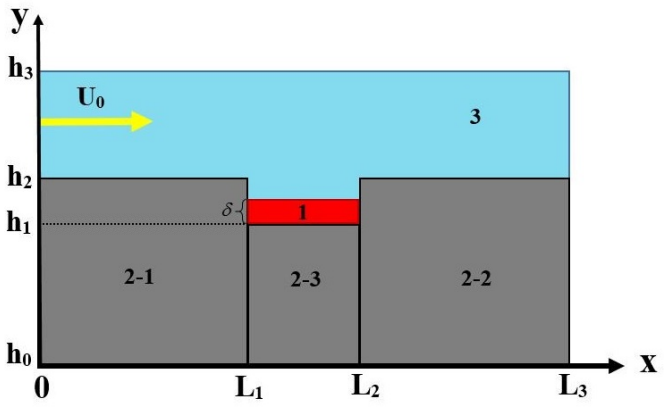

Figure 2: Our proposed scheme for analyzing in this study; 1- Layer of Cs-137 (as the radioactive contamination), 2- Graphite (divided into three parts), and 3- Plasma region.

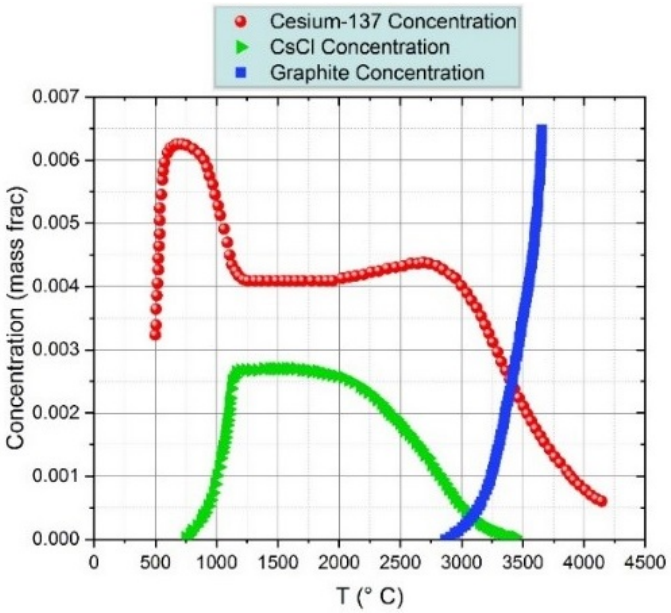

Figure 3: Variation of Cs-137, CsCl, and Graphite concentrations during interaction of unit cell with argon atmospheric pressure plasma.

The results show that, in the temperature range of 500 to 2000 °C, the Cs-137 structures are in the form of chloride ($SrCl_2$, SrCl, and CsCl). Figure 3 shows that selective sublimation of radionuclides due to the interaction of plasma flow with irradiated Graphite can be managed by changing the temperature of plasma average mass and this factor reduces GRW activity. The diagrams shown

in Fig. 3 also illustrates that in the plasma decontamination process of irradiated Graphite and over a wide range of temperatures, the Cs-137 radionuclides have high mass concentrations and therefore it is very important and this is another reason that why, of all the radionuclides, we will do the calculation for the Cs-137 radionuclides in this study. Another important conclusion to be drawn from Fig. 3 is the evaporation of irradiated Graphite starts at approximately 3000 °C; Therefore, to avoid damaging the Graphite structure, the temperature of the plasma jet should not be exceeded 3000 °C. In Fig. 3, the mass fraction means the evaporated mass divided by the initial mass (the amount of evaporated material divided by the amount of the initial material).

3.2 *Thermodynamic modeling of the plasma decontamination process of the irradiated Graphite*

According to Fig. 2, in the intended geometry for computational analysis, the plasma flow velocity at the input of the desired computational range (has height of $|h_3 - h_2|$ on the Graphite surface) is equal to u_0. It is also assumed that the transverse and longitudinal dimensions of entire computational cell are much larger than the thickness of the Cs-137 contamination. The Graphite surface heats up due to contact with the plasma particles and heat transfer. For simulation of the heat and mass transfer processes of Cs-137 in irradiated Graphite pores, their differential heat transfer equations were solved in Cartesian coordinates by Maple 2020 software. The positive direction of the X-axis is assumed along the velocity vector u_0 (plasma flow velocity):

$$c_1\rho_1\frac{\partial T_1}{\partial t} = \lambda_1\Big(\frac{\partial^2 T_1}{\partial x^2} + \frac{\partial^2 T_1}{\partial y^2}\Big) \tag{1}$$

in which $h_1 < y < h_1 + \delta$ and $L_1 < x < L_2$.

$$c_2\rho_2\frac{\partial T_2}{\partial t} = \lambda_2\Big(\frac{\partial^2 T_2}{\partial x^2} + \frac{\partial^2 T_2}{\partial y^2}\Big) + Q_{Wig} \tag{2}$$

in which $0 < x < L_1$, $h_0 < y < h_2$; $L_1 < x < L_2$, $h_0 < y < h_1$; $L_2 < x < L_3$, $h_0 < y < h_2$.

$$c_3\rho_3\frac{\partial T_3}{\partial t} = \lambda_3\Big(\frac{\partial^2 T_3}{\partial x^2} + \frac{\partial^2 T_3}{\partial y^2}\Big) - c_3\rho_3 u\Big(\frac{\partial T_3}{\partial x} + \frac{\partial T_3}{\partial y}\Big) \tag{3}$$

in which $L_1 < x < L_2$, $h_1 + \delta < y < h_2$; $0 < x < L_3$, $h_2 < y < h_3$.

$$u = u_0\Big(\frac{T_3}{298}\Big) \tag{4}$$

In these equations, c_1, ρ_1, and λ_1 are heat capacity, density, and thermal conductivity of Cs-137 contamination, respectively. c_2, ρ_2, and λ_2 are heat capacity, density, and thermal conductivity of irradiated Graphite, respectively. Q_{Wig} is the power density of heat released due to temperature changes of defective graphitic structures (the release of Wigner energy). c_3, ρ_3, and λ_3 are heat capacity, density, and thermal conductivity of plasma flow, respectively. h_0 is the initial height of inactive Graphite layer (equal to zero), h_1 is the height of the Graphite pore from the origin, h_2 is the height of the upper surface of the inactive Graphite layer from the origin, h_3 is the height of the plasma boundary, L_1 and L_2 are the longitudinal coordinates of the beginning and end of the Cs-137 contamination layer, and L_3 is the length of the Graphite sample. Also, T_1, T_2, and T_3 are the temperatures of Cs-137 contamination, the temperature of irradiated Graphite, and the temperature of plasma particles (at the time t), respectively. The right side of Eq. (2) contains Q_{Wig}, which represents the release of stored energy (Wigner energy) and during the plasma processing of irradiated Graphite, this parameter affects the thermal balance of the whole system. Additional information on the release of Wigner energy from irradiated Graphite is also given in the reference (Bespala et al., 2018). Calculations show that as a result of the release of Wigner energy, the temperature of irradiated Graphite under the adiabatic heating can be increased up to $\Delta T = 600 - 650$ °C (Bespala et al., 2019).

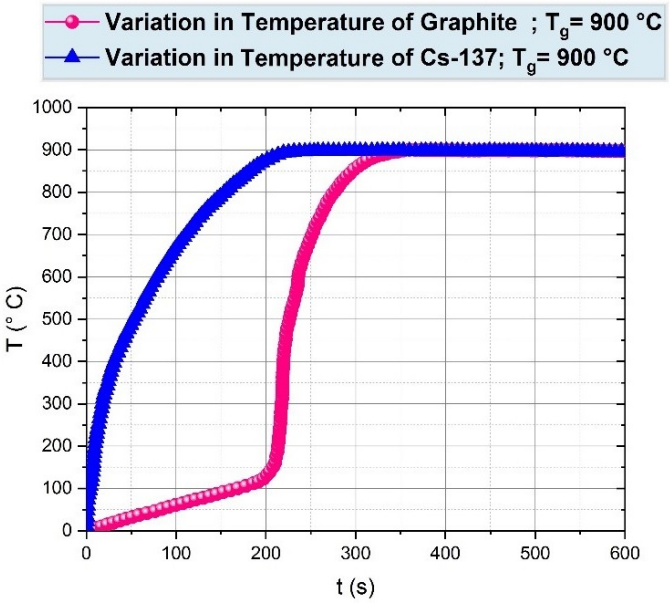

Figure 4: Temperature changes over time in Graphite and Cs-137. The sharp variation occurs at $t = 200$ s for Graphite which is due to the release of Wigner energy.

The mass transfer process depends on thermodynamic conditions and diffusion coefficients in which, their values are given in (Bespala et al., 2018, 2019). Also, the thermodynamic parameters of the Cs-137 contamination are mentioned in reference (Bespala et al., 2017). Since the sublimation of Cs-137 leads to its diffusion in the plasma stream, solving the above equations requires the determination of specific parameters of this process and since in this case, it is difficult to accurately calculate the diffusion parameters, the values of the Cs-137 diffusion parameters in Argon gas obtained from the reference (Aref'yev et al., 1974). We assume that at the initial time, for the whole system that it has not yet been irradiated with plasma, the temperature is uniform and equal to T_0 ($T_g > T_0$). Equations (1) to (4) were solved using Maple 2020 software under certain boundary conditions. Graphite tem-

perature changes was investigated at T_g = 900 °C; The results show that in the first 200 seconds, the graphite temperature changes linearly and in the next 100 seconds, the Graphite temperature changes rapidly and exponentially; The cause of this phenomenon is that in the first 200 seconds, most of the heat given to the Graphite leads to the compensation of lattice defects and as a result of the heated defects, the release of Wigner energy occurs, which is shown as a sharp variation in the Fig. 4. Finally, due to the fact that the heat of the irradiated Graphite is transferred to radioactive contaminants, 300 seconds after starting of the process, the Graphite temperature changes to saturation level. In this case, a sudden rise in temperature has a greater effect on the rate of heating of radioactive contaminants. Among all radioactive contaminants, Cs-137 radionuclide is more affected by the sudden rise in temperature than other contaminants due to its high thermal conductivity (Bespala et al., 2017).

The most meaningful parameter that indicates the efficiency of the irradiated Graphite surface processing is the rate of entry of the mass of radioactive contaminant (M_i) into the gas phase (Pavliuk et al., 2018a).

Therefore, after 200 seconds the interaction of argon gas flow with the Cs-137 surface, the Cs-137 temperature will be on the verge of saturation and due to the increase of sublimation capability of radioactive contaminants, plasma processing of irradiated Graphite is suggested at higher temperatures (up to a maximum of 3000 °C). According to Fig. 4, the Wigner energy emission simultaneously affects both the heating of the Graphite and Cs-137, but since the heat capacity of carbon is equal to 8.51 J.mol^{-1}.K^{-1} and it is almost four times lower than the heat capacity of Cs-137 (32.210 J.mol^{-1}.K^{-1}), Carbon is more sensitive to Wigner energy than Cs-137 and thus, its temperature chart has a steeper slope than the temperature chart of Cs-137 and this is an example of the physical interpretation that under the same thermodynamic conditions, the materials with lower heat capacity will have a steeper slope of temperature changes than the materials with higher heat capacity; But in the case of Cs-137, although Wigner heat affects the Cs-137 temperature increase, but due to the high heat capacity of Cs-137, the amount of Wigner heat is not effective enough to show its effects on the Cs-137 temperature diagram and finally, the entire system reaches thermodynamic equilibrium within 300 seconds after the start of the heat treatment operation. Figure 5 shows the T and M_i change for the Cs-137 radionuclide during the temperature range up to 2700 °C. When the plasma flow interacting with surface of the irradiated Graphite pore, the rate of Cs-137 evaporation will soon be changed due to the temperature changes in the surface. Calculations show that the mass transfer rate varies in the range of $(2.5 - 60) \times 10^{-6}$ kg.m^{-2}.s^{-1} under the boundary conditions that we have chosen for Graphite processing. As an important result, in the plasma processing of irradiated Graphite surfaces, the radionuclide compounds which have the lowest heat capacity evaporate more quickly, and then the surfaces are clean of them.

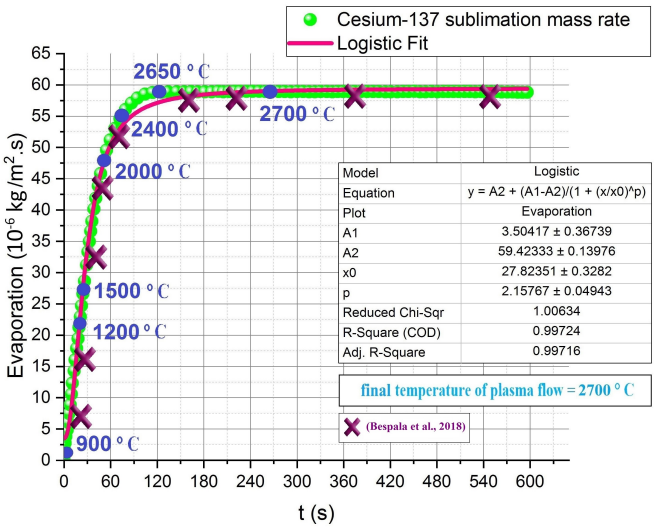

ANOVA

		DF	Sum of Squares	Mean Square	F Value	Prob>F
Evaporation	Regression	4	266502.59072	66625.64768	66205.58579	0
	Residual	98	98.62179	1.00634		
	Uncorrected Total	102	266601.21251			
	Corrected Total	101	35765.15713			

Figure 5: Temperature changes and rate of mass changes of Cs-137 sublimation in noble-gas plasma jet (with Argon as feed gas) over time and in the circumstances that plasma temperature rises from 900 to 2700 °C in a total of 270 s.

In Fig. 5, the vertical axis dimension (rate of mass changes of Cs-137 sublimation) is expressed in 10^{-6} g.mm^{-2}.s^{-1}, which in order to better express the physical concept, is shown in terms of its equivalent, which is 10^{-6} kg.m^{-2}.s^{-1}. In general, we use the sputtering decontamination technique when, from an engineering point of view, the sublimation temperature of the desired radioactive contamination is available. For example, the Co-60 radionuclide has a sublimation temperature of 2870 °C and its sublimation is possible using the plasma technique, but it requires more energy. Also in the case of the possibility of selective decontamination, this is possible for contaminants that have a very long half-life; because it may take a long time to reach the maximum rate of pollutant sublimation. For example, Co-60 radionuclide has a half-life of 5.27 years and can be selectively removed by modifying plasma parameters. It is important to note that in the plasma decontamination technique, the time to reach the highest rate of pollution sublimation should be less than the half-life of the desired pollutant and this issue should be paid special attention (Bespala et al., 2017).

4 Conclusions

Plasma processing is one of the promising methods for decontamination of irradiated Graphite in the nuclear industry and therefore, the simulation and the mathematical study of this process cause that, in addition to detailed analysis of decontamination operations, we minimize the potential effect of the radiation hazards during the actual experimental operation process. In this study, the decontamination of Cs-137 from irradiated Graphite

is investigated and analyzed using the plasma-sputtering method in which, Thermodynamic processes of heat and mass transfer during the interaction and effect of plasma on the surfaces of irradiated Graphite are analyzed. In order to reduce the specific activity of irradiated Graphite and also reduce its potential hazards, it is recommended that its heat treatment be performed in an inert gas environment (this action reduces GRW activity). This study demonstrates the benefits of using Argon as a plasma feed gas in the plasma decontamination process.

In the plasma decontamination process of irradiated Graphite and over a wide range of temperatures, the Cs-137 radionuclides have high mass concentrations and therefore it is very important and this is another reason why, of all the radionuclides, we will do the calculation for the Cs-137 radionuclides in this study. Another important conclusion is the evaporation of irradiated Graphite starts at approximately 3000 °C; Therefore, to avoid damaging the Graphite structure, the temperature of the plasma jet should not be exceeded 3000 °C. Results show that selective sublimation of radionuclides due to the interaction of plasma flow with irradiated Graphite can be managed by changing the temperature of plasma average mass and this factor reduces GRW activity.

During the process of decontamination of Cs-137 from irradiated graphite surfaces, using the plasma-sputtering method with noble argon feed gas, most of the heat given to the Graphite leads to the compensation of lattice defects and as a result of the heated defects, the release of Wigner energy occurs. The release of Wigner energy, simultaneously, affects the heating of graphite and Cs-137. Heat released due to temperature changes of defective graphitic structures (the release of Wigner energy) affects the thermal balance of the whole system. But because of the heat capacity of carbon which is about four times lower than that of Cs-137, carbon is more sensitive to Wigner energy and therefore, its temperature behavior will have a steeper slope than Cs-137 temperature. In the case of Cs-137, Wigner's heat has an effect on its temperature rise, but due to the high heat capacity of Cs-137, Wigner heat is not that much which its effects can be seen in the temperature rise diagram of Cs-137 and finally, the entire system reaches to the thermodynamic equilibrium within 300 seconds after the starting at heat treatment operation. the release of Wigner energy was also shown to affect the removal rate and clearance of Cs-137. The results obtained are in good agreement with the other researchers results (Bespala et al., 2018).

The results of this study can be used to decontamination of various types of irradiated porous materials used in other nuclear systems. According to the obtained results on the characteristics of plasma required for decontamination of Cs-137 from irradiated graphite, based on these characteristics, it is possible to design and manufacture useful plasma actuators in this field.

Conflict of Interest

The authors declare no potential conflict of interest regarding the publication of this work.

Copyright

References

Aref'yev, K., Vorontsova, L., Zablotskaya, T., et al. (1974). Diffusion coefficients of alkali metal vapors in inert gases.

Auciello, O., Gras-Martí, A., Valles-Abarca, J. A., et al. (2012). *Plasma-surface interactions and processing of materials*, volume 176. Springer Science & Business Media.

Barbin, N., Shavaleev, M., Terentyev, D., et al. (2015). Computer simulation of thermodynamic processes with involvement of actinoids heating radioactive graphite in the nitrogen atmosphere. *Applied Physics*, 6:42–7.

Bespala, E., Myshkin, V., Pavlyuk, A., et al. (2017). Heat and mass transfer in cesium evaporation from graphite surface in argon. *Atomic Energy*, 122(6):400–405.

Bespala, E., Novoselov, I., and Ushakov, I. (2016). Heat transfer during evaporation of cesium from graphite surface in an argon environment. In *MATEC Web of Conferences*, volume 72, page 01011. EDP Sciences.

Bespala, E., Novoselov, I. Y., Pavlyuk, A., et al. (2018). Study of evaporating the irradiated graphite in equilibrium low-temperature plasma. *Thermophysics and Aeromechanics*, 25(1):109–117.

Bespala, E., Pavliuk, A., Kotlyarevskiy, S., et al. (2019). Modeling of processing of irradiated graphite contained fission and neutron-activation products by noble gas flow. In *AIP Conference Proceedings*, volume 2101, page 020004. AIP Publishing LLC.

Bushuev, A., Aleeva, T., Petrova, E., et al. (2003). Possibility of salvaging spent graphite sleeves from the reactors of the siberian chemical combine by incineration. *Atomic Energy*, 94(2):91–98.

Bushuev, A., Kozhin, A., Zubarev, V., et al. (2015). Radioactive contamination of spent reactor graphite. *Atomic Energy*, 117(3):196–200.

Dunzik-Gougar, M. L. and Smith, T. E. (2014). Removal of carbon-14 from irradiated graphite. *Journal of Nuclear Materials*, 451(1-3):328–335.

Fachinger, J., von Lensa, W., and Podruhzina, T. (2008). Decontamination of nuclear graphite. *Nuclear Engineering and Design*, 238(11):3086–3091.

IAEA (2001). Methods for the minimization of radioactive waste from decontamination and decommissioning of nuclear facilities. Technical report, Vienna, Austria.

IAEA (2008). Innovative and adaptive technologies in decommissioning of nuclear facilities: Final report of a coordinated research project 2004-2008. Technical report, Vienna, Austria.

Kane, J. J., Karthik, C., Ubic, R., et al. (2013). An oxygen transfer model for high purity graphite oxidation. *Carbon*, 59:49–64.

Kuijper, J., Raepsaet, X., De Haas, J., et al. (2006). HTGR reactor physics and fuel cycle studies. *Nuclear Engineering and Design*, 236(5-6):615–634.

Laraia, M. (2012). Nuclear decommissioning. *Planning, Execution and International*.

Pavliuk, A., Zagumennov, V., Kotlyarevskiy, S., et al. (2018a). Thermodynamic simulation of equilibrium composition of reaction products at dehydration of a technological channel in a uranium-graphite reactor. *Thermal Engineering*, 65(1):51–56.

Pavliuk, A. O., Kotlyarevskiy, S. G., Bespala, E. V., et al. (2018b). Experience of on-site disposal of production uranium-graphite nuclear reactor. *Journal of Environmental Radioactivity*, 184:22–31.

Sato, H. and Yan, X. L. (2019). Study of an HTGR and renewable energy hybrid system for grid stability. *Nuclear Engineering and Design*, 343:178–186.

Theodosiou, A., Jones, A., Burton, D., et al. (2018). The complete oxidation of nuclear graphite waste via thermal treatment: An alternative to geological disposal. *Journal of Nuclear Materials*, 507:208–217.

Vulpius, D., Baginski, K., Kraus, B., et al. (2013). Thermal treatment of neutron-irradiated nuclear graphite. *Nuclear Engineering and Design*, 265:294–309.

Wickham, A., Steinmetz, H.-J., O'Sullivan, P., et al. (2017). Updating irradiated graphite disposal: Project 'GRAPA' and the international decommissioning network. *Journal of Environmental Radioactivity*, 171:34–40.

Young, D. A. (1975). Phase diagrams of the elements. Technical report, California Univ.

RPE | Radiation Physics & Engineering
An International Peer-Reviewed Journal
Published by K.N. Toosi University of Technology
http://rpe.kntu.ac.ir
Research Article

Radiation Physics and Engineering 2023; 4(2):53–60

Assignment of a radiological map of the city of Borujerd in Iran

Reza Pourimani*, Mobin Bajelan, Monire Mohebian

Department of Physics, Faculty of Science, Arak University, Arak, Iran

HIGHLIGHTS

- Measurement of natural radionuclides in soil samples of Borujerd city.
- Calculation of radiometric parameters for these samples.
- Comparison of them contains with other reported work from other countries.
- Provided discussion about of radiological indices.
- Drown radiological map of Borujerd city.

ABSTRACT

The specific activity of radionuclides in the soil of the Borujerd region using high purity Germanium detector (HPGe) was measured and the associated radiological hazards were calculated. The mean specific activity of radionuclides of Ra-226, Th-232, K-40, and Cs-137 in soil was obtained at 10.99 ± 5.11, 35.36 ± 4.44, 324.20 ± 10.24, and 2.93 ± 0.60 Bq.kg^{-1}. These values were below the global average. Also, the value of basic radiological risk parameters, such as Ra_{eq}, AED_{out}, AED_{int}, H_{ex}, H_{in}, and I_{γ}, ranged from 52.02 to 139.54 in Bq.kg^{-1}, from 24.98 to 68.27 and from 42.90 to 117.22 in mSv.y^{-1}, 122.57 to 334.93, 0.14 to 0.37, 0.16 to 0.40, and 0.27 to 1.04, respectively. The range of excess lifetime cancer risk (ELCR) value for the surrounding soil samples varied from 0.15×10^{-3} to 0.41×10^{-3}, in which samples S4, S14, S24, S27, S28, S29, and S30 exceeded the global average of 0.29×10^{-3}. A radiological map of the city of Borujerd was prepared using the GIS program. The study showed that the level of radioactivity in the Borujerd area did not exceed the critical value and is in line with the global results.

KEYWORDS

Radionuclide
Radiological map
Radiological indices
HPGe

HISTORY

Received: 13 November 2022
Revised: 7 December 2022
Accepted: 22 December 2022
Published: Spring 2023

1 Introduction

Humans are always affected by nuclear radiation from naturally occurring radioactive nuclei such as elements in the U-238 and Th-232 chains and some radioactive nuclei such as radionuclide K-40. The high level of potassium in the soil is due to the fact that it makes up an average of 2.8% of soil weight. On average, the amount of uranium and thorium in soil was estimated as 2.7 and 9.6 mg.kg^{-1} (Mohebian and Pourimani, 2019). In addition to natural radiation, our environment also has radiation induced by special artificial radioactive nuclei, such as Cs-137 and Sr-90 (UNSCEAR, 2000). Cs-137 is one of the fission products created and released into the environment due to nuclear accidents such as the explosion of the Chernobyl reactor in Ukraine (1986) (UNSCEAR, 2000).

Due to the harmful nature of nuclear radiation to human health, it is necessary to conduct soil monitoring in areas where people live and are exposed to natural and artificial nuclear radiation. This is important for determining the distribution and radiological mapping of radionuclides in residential and food-producing regions. In the field of measuring the amount of radioactivity in soil samples, countless types of research have been conducted in the countries of Iraq, Turkey, Saudi Arabia, Pakistan, India, Congo, China, Egypt, Malaysia, and also in Iran (Agbalagba and Onoja, 2011; Hussain and Alzhraa, 2017; Adewoyin et al., 2022; Hasan and Majeed, 2013; Dizman et al., 2016; Alshahri and El-Taher, 2019; Khan et al., 2020; Suresh et al., 2020; Diahou et al., 2022; Ziqiang et al., 1988; El-Araby et al., 2021; Alzubaidi et al., 2016; Pourimani et al., 2017; Mohebian and Pourimani, 2020). This study specifies the distribution of radionuclides and a radiological map of the city of Borujerd in the central region of Iran.

*Corresponding author: r-pourimani@araku.ac.ir

https://doi.org/10.22034/rpe.2022.370078.1108
https://dorl.net/dor/20.1001.1.26456397.2023.4.2.7.3

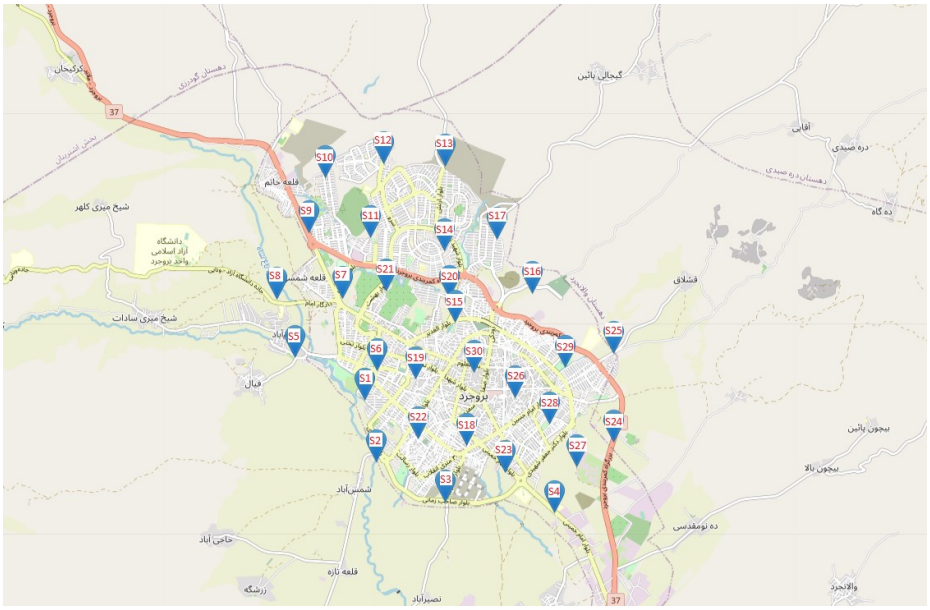

Figure 1: Sampling points area of Borujerd city in Iran.

2 Materials and Methods

2.1 Area and sampling method

In the present study, 30 soil samples were taken from surface soils (less than 10 cm depth) in the Borujerd areas of Iran, and the longitude and latitude of the sampling site were recorded with the Global Positioning System (GPS). Figure 1 shows the sampling area that covered the entire city area.

2.2 Preparation of samples

500 g of soil were collected from the sampling points and transported in a plastic bag with a region label. In accordance with the International Atomic Energy Organization's environmental sample preparation and packaging instructions, 300 g of powder after grinding and passing the samples through 20 and 50 mesh was packed, sealed, and encoded in cylindrical containers of 300 g (Barnett et al., 2009). Coding was done according to the geographical location of each sample. Soil samples were sealed with silicon glue. The seal of the container prevents the release of radon gas in the uranium chain. To measure the amount of Ra-226, it is necessary to establish a secular equilibrium between radium and radon so that the sample containers are tightly closed for at least 50 days before the measurement (Jibiri and Esen, 2011). In the event of the release of radon gas, the activity of the radium nucleus cannot be obtained from the activity of the radon daughter nuclei (Ranjbar and Yousefi, 2019).

2.3 Radionuclide analysis of samples

To determine the specific activities of radionuclides in the samples, it is necessary to calibrate the energy and efficiency of the detector-sample system. Energy and efficiency calibration was done using a standard RGU-1 and Cs-137 sources of known activity (Pourimani and Davood Maghami, 2020). RGU-1 is a known reference material in the form of a fine powder with known activity that can be used in any configuration, including a sample container. The relationship between energy and channel is shown in Eq. (1):

$$Energy = 7.52 + (0.33 \times Channel) \tag{1}$$

High purity germanium detector system was used in this research. The GCD30195BSI model detector operated at voltage of 3000 V, an energy resolution of 1.95 keV and a relative efficiency of 30%. The gamma ray spectrum of each sample was registered using LSRMBSI software. The spectra were analyzed using Gamma Vision Master II Ortec EG software. The efficiency value of gamma lines was determined using Eq. (2) (Hossain et al., 2010):

$$\epsilon(\%) = \frac{Net\ Area}{A \times BR(\%) \times T} \times 100 \tag{2}$$

where NetArea is the net count under the full energy peak corresponding to the energy E_i, A is the specific activity of the radionuclide, BR (%) is the probability of E_i photon emission, and T specifies the counting time. The graph of efficiency as a function of gamma-ray energy plotted using the Matlab program is shown in Fig. 2. The gamma ray spectrum of each sample was recorded for 86,400 s. Background radiation was measured with an empty container under the same conditions and subtracted from each spectrum (Pourimani and Mohebian, 2021).

2.3.1 Measuring the specific activity of radioactive nuclei

Using the net count under full peak energy ($NetArea$), detector-sample efficiency (ϵ), sample weight (m), and gamma emission probability (BR), the specific activities of Ra-226, Th-232, K-40, and Cs-137 in the samples were

calculated using Eq. (3) (Kabir et al., 2009):

$$A = \frac{Net\ Area}{\epsilon(\%) \times BR(\%) \times T \times m} \times 100 \quad (3)$$

So that A is the specific activity of the radionuclide in the sample in Bq.kg^{-1}, T is the counting time in seconds. The global average value of the specific activity of radium, thorium and potassium nuclei is 30, 35, and 412 Bq.kg^{-1} (Annex et al., 2000). The activity of Ra-226 was calculated from the gamma emission of Pb-214 (351.93 keV) and Bi-214 (609.31 keV). Th-232 activity was determined using gamma energies of Pb-212 (238.6 keV), Ac-228 (911.21 and 968.97 keV), and Tl-208 (583.2 keV). The K-40 activity was assessed directly with its gamma radiation (1460.75 keV) and Cs-137 activity was determined using its gamma line as 661.66 keV.

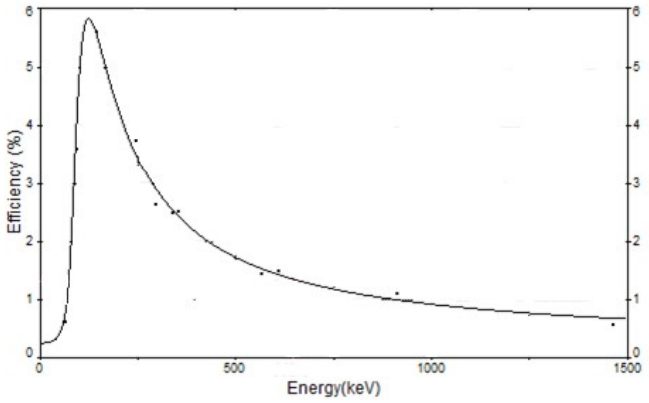

Figure 2: Efficiency diagram of the detector-sample configuration as a function of gamma-ray energy.

2.3.2 Radium equivalent activity

Ra equivalent activity is a single quantity that is used to determine the radiation level of natural radionuclides in terms of Ra-226 radioactivity and is one of the most common indicators of radiation level. This indicator is based on the evaluation that 370 Bq.kg^{-1} of Ra-226, 259 Bq.kg^{-1} of Th-232, and 4180 Bq.kg^{-1} of K-40 give the same gamma dose rate. It can be calculated using Eq. (4) (UNSCEAR, 2000):

$$Ra_{eq} = A_{\mathrm{Ra}} + 1.43A_{\mathrm{Th}} + 0.077A_{\mathrm{K}} \quad (4)$$

2.3.3 The absorbed dose rate in the air

At a height of 1 m above the ground, for radionuclides uniformly distributed in soil and rock, the absorbed gamma radiation dose (D) in the air can be calculated using Eq. (5) (UNSCEAR, 2000):

$$D\ (\mathrm{nGy.h^{-1}}) = 0.427\,A_{\mathrm{Ra}} + 0.662\,A_{\mathrm{Th}} + 0.0432\,A_{\mathrm{K}} \quad (5)$$

2.3.4 Internal and external annual effective dose

The annual effective dose in open air (AED) in terms of μSv.y^{-1} is related to the dose absorbed in the air (D) at a height of 1 m from the soil surface in terms of nGy.h^{-1} (Eqs. (6) and (7)). Since soil sampling is possible in materials, if a building is used, the annual effective dose inside the building has also been calculated (Pourimani and Mohebian, 2021).

$$AED_{outdoor}\ (\mu\mathrm{Sv.y^{-1}}) = Dose\ rate\ (\mathrm{nGy.h^{-1}}) \times 8760\ (\mathrm{h.y^{-1}}) \times 0.20 \times 0.7\ (\mathrm{Sv.Gy^{-1}}) \times 10^{-3} \quad (6)$$

$$AED_{indoor}\ (\mu\mathrm{Sv.y^{-1}}) = Dose\ rate\ (\mathrm{nGy.h^{-1}}) \times 8760\ (\mathrm{h.y^{-1}}) \times 0.8 \times 0.7\ (\mathrm{Sv.Gy^{-1}}) \times 10^{-3} \quad (7)$$

The internal and external occupancy factors are 0.80 and 0.20 respectively, and also a factor of 0.7 was used for the Gy to Sv conversion (Pourimani and Mohebian, 2021).

2.3.5 Calculation of internal and external risk indicators

The external risk index shows the amount of gamma radiation in the environment and the presence of radioactive nuclei in soils and rocks that may pose a threat to humans. The internal risk index is caused by inhalation of radon gas or ingestion of radionuclides. These parameters are calculated using Eqs. (8) and (9) (Kabir et al., 2009). For a safe environment, the maximum values of external and internal radiation risk indicators should be less than 1 (UNSCEAR, 2000).

$$H_{ex} = \frac{A_{\mathrm{Ra}}}{370} + \frac{A_{\mathrm{Th}}}{259} + \frac{A_{\mathrm{K}}}{4810} \leq 1 \quad (8)$$

$$H_{in} = \frac{A_{\mathrm{Ra}}}{185} + \frac{A_{\mathrm{Th}}}{259} + \frac{A_{\mathrm{K}}}{4810} \leq 1 \quad (9)$$

2.3.6 Calculation of gamma index (I_γ)

The gamma index is used to estimate the level of exposure to gamma radiation associated with naturally occurring radionuclides in soil and rocks. Equation (10) is used to calculate this index (Annex et al., 2000):

$$I_\gamma = \frac{A_{\mathrm{Ra}}}{150} + \frac{A_{\mathrm{Th}}}{100} + \frac{A_{\mathrm{K}}}{1500} \quad (10)$$

In Eqs. (4) to (10), A_{Ra}, A_{Th}, and A_{K} are the specific activities of Ra-226, Th-232, and K-40 in Bq.kg^{-1}, respectively.

2.3.7 Excess Lifetime Cancer Risk

The Excess Lifetime Cancer Risk ($ELCR$) is proportional to the absorbed annual effective dose (AED), life expectancy (LE), and risk factor (RF). Equation (11) using for the calculation of this important index. The Excess Lifetime Cancer Risk during the lifetime causes by environmental gamma radiation (UNSCEAR, 2000).

According to the World Health Organization report for Iranians, LE was 73.15 years (ÇINAR and Altundaş,

Table 1: The specific activities of natural radionuclides, Cs-137, radium equivalent, and absorbed dose rate in the air. MDA shows th Minimum Detectable Activity.

Sample code	Specific activity (Bq.kg^{-1})				Radiological Index	
	Ra-226	Th-232	K-40	Cs-137	Ra_{eq} (Bq.kg^{-1})	D (nG.h^{-1})
S1	17.63 ± 0.78	23.00 ± 3.78	363.85 ± 9.84	0.36 < MDA	78.53	38.47
S2	10.40 ± 0.89	67.10 ± 5.57	376.24 ± 10.48	1.11 < MDA	135.32	65.11
S3	6.16 ± 0.84	33.90 ± 4.53	513.85 ± 12.12	0.93 < MDA	94.20	47.27
S4	7.11 ± 0.85	40.80 ± 4.83	516.98 ± 12.34	1.04 < MDA	105.26	52.37
S5	2.56 ± 0.76	27.41 ± 4.13	380.56 ± 9.71	0.96 < MDA	71.05	35.67
S6	3.73 ± 0.77	45.77 ± 4.65	407.13 ± 10.07	0.94 < MDA	100.53	49.48
S7	29.85 ± 2.14	25.41 ± 3.77	293.26 ± 8.21	3.49 ± 0.32	87.76	42.23
S8	9.72 ± 0.69	31.40 ± 4.16	315.56 ± 9.02	0.90 < MDA	78.92	38.56
S9	2.39 ± 0.75	31.58 ± 4.04	353.58 ± 9.35	0.94 < MDA	75.31	37.20
S10	MDA > 2.61	41.74 ± 4.51	265.20 ± 7.58	0.89 < MDA	80.10	39.08
S11	2.58 ± 0.72	22.46 ± 3.80	306.69 ± 8.51	0.85 < MDA	58.31	29.21
S12	MDA > 2.56	41.41 ± 4.76	490.91 ± 12.05	0.96 < MDA	97.01	48.62
S13	26.74 ± 2.02	17.06 ± 3.59	228.46 ± 7.22	0.84 < MDA	68.72	32.58
S14	8.96 ± 0.83	42.57 ± 4.80	487.42 ± 12.68	0.99 < MDA	107.36	53.06
S15	5.25 ± 0.78	33.20 ± 4.53	252.02 ± 8.88	0.93 < MDA	72.13	35.10
S16	29.66 ± 2.19	17.88 ± 3.99	159.01 ± 6.72	1.25+0.30	67.47	31.37
S17	8.13 ± 0.73	32.55 ± 3.88	280.51 ± 9.11	0.93 < MDA	76.27	37.13
S18	7.01 ± 0.81	35.24 ± 4.53	252.98 ± 9.36	0.97 < MDA	76.88	37.25
S19	5.70 ± 0.80	36.04 ± 4.42	261.48 ± 9.36	0.99 < MDA	77.37	37.58
S20	12.33 ± 0.68	23.25 ± 5.02	226.23 ± 8.02	0.92 < MDA	65.71	30.42
S21	11.48 ± 0.69	18.99 ± 3.84	173.92 ± 8.03	0.94 < MDA	52.02	24.98
S22	14.48 ± 0.74	20.11 ± 4.57	191.35 ± 8.79	0.97 < MDA	57.97	27.76
S23	23.50 ± 0.84	27.61 ± 4.83	351.50 ± 10.29	1.01 < MDA	90.04	43.49
S24	13.48 ± 0.67	40.54 ± 6.05	458.51 ± 11.75	4.45 ± 0.40	106.75	52.40
S25	6.10 ± 0.70	34.78 ± 4.04	413.57 ± 9.90	3.33+0.30	87.68	43.49
S26	7.84 ± 0.71	40.77 ± 4.33	427.40 ± 10.15	2.15 ± 0.28	99.05	48.20
S27	6.42 ± 0.74	47.09 ± 4.27	539.22 ± 12.21	0.94 < MDA	115.27	57.20
S28	10.19 ± 0.79	53.15 ± 4.77	505.13+11.8	0.97 < MDA	125.08	61.35
S29	9.74+0.78	62.10 ± 4.94	532.55 ± 12.29	0.97 < MDA	139.54	68.27
S30	8.57 ± 0.74	45.87 ± 4.43	488.46 ± 11.45	0.92 < MDA	111.77	55.12
MIN	MDA > 2.56	17.06 ± 3.59	159.01 ± 6.72	0.36 < MDA	52.02	24.98
MAX	29.845 ± 2.14	67.10 ± 5.57	539.22 ± 12.21	4.45 ± 0.40	139.54	68.27
MEAN	10.99 ± 5.11	35.36 ± 4.44	324.20 ± 10.24	0.60 ± 2.93	88.64	43.33

2015) and the International Committee on Radiation Protection established the risk conversion factor to be 0.05 Sv^{-1}. The global average is 0.29×10^{-3} and the maximum acceptable limit is 10^{-3} (UNSCEAR, 2000).

$$ELCR = AED_{outdoor} \times LE \times RF \qquad (11)$$

3 Results

The specific activities of Ra-226, Th-232, K-40 and Cs-137 radioactive nuclei was measured in 30 soil samples. The data results are listed in Table 1. Based on the data from Table 1, the highest value of the specific activity of Ra-226 was obtained in sample S7, and the lowest in sample S10. The highest and lowest value of specific activity of Th-232 radioactive nucleus is in samples S2 and S13, respectively. The highest value of the specific activity of the K-40 nucleus was obtained in sample S27 and the lowest amount of activity was obtained in sample S16. The Cs-137 with a maximum value of 4.45 Bq.kg^{-1} was measured in Samples S1, S16, S24, S25, S26, and S27, and for the rest of the samples was lower than the MDA level of the detector system. The calculated radiological parameters are presented in Table 2. The values of radiological risk parameters such as Ra_{eq}, AED_{out}, AED_{int}, D, H_{ex}, H_{in}, and I_{γ} varied in the range of 52.02 to 139.54) Bq.kg^{-1}, 24.98 to 68.27 and 122.57 to 334.93 in μSv.y^{-1}, 42.90 to 117.22 nGy.h^{-1}, 0.14 to 0.37, 0.16 to 0.40, 0.27 to 1.04, respectively. Figure 3 shows the comparison of the equivalent activity value of radium in this study with other countries. According to this figure, Pakistan shows a higher equivalent activity value compared to other countries. On the other hand, all values are lower than the global average value.

Figure 4 compares the gamma index value in this study with other countries where Turkey and Pakistan show the highest and the lowest gamma index values, respectively, compared to other countries. For all mentioned countries except Turkey, the gamma index values were lower than the global average. The range of ELCR values for soil samples ranged from 0.15×10^{-3} to 0.41×10^{-3}, which for samples s4, s14, s24, s27, s28, s29, and s30 was greater than the global average of 0.29×10^{-3}. Maps of Ra-226 distribution and airborne dose rate by GIS software are shown in Figs. 5 and 6. Ra-226 was higher at several locations near the central part of the city, and the absorbed

Table 2: Radiological parameters of samples.

Sample code	Radiological Index					
	AED_{out} (μSv.y^{-1})	AED_{in} (μSv.y^{-1})	H_{ex}	H_{in}	I_γ	$ELCR$ ($\times 10^{-3}$)
S1	66.05	188.48	0.21	0.25	0.59	0.23
S2	111.79	319.42	0.36	0.39	0.98	0.39
S3	81.16	231.88	0.25	0.27	0.72	0.28
S4	89.93	256.95	0.28	0.30	0.80	0.31
S5	61.25	175.02	0.19	0.32	0.54	0.21
S6	84.95	242.73	0.27	0.27	0.75	0.29
S7	72.51	207.18	0.23	0.32	0.64	0.25
S8	66.22	189.20	0.21	0.23	0.58	0.23
S9	63.87	182.49	0.20	0.20	0.56	0.23
S10	67.11	191.75	0.21	0.21	0.59	0.23
S11	50.16	143.33	0.15	0.16	0.44	0.17
S12	83.47	238.51	0.26	0.26	0.74	0.29
S13	55.94	159.83	0.18	0.25	0.50	0.19
S14	91.10	260.300	0.28	0.31	0.81	0.31
S15	60.27	172.22	0.19	0.20	0.53	0.21
S16	53.86	153.89	0.18	0.26	0.63	0.18
S17	63.76	182.18	0.20	0.22	0.39	0.22
S18	63.95	182.73	0.20	0.22	0.56	0.22
S19	64.53	184.39	0.20	0.22	0.57	0.22
S20	52.24	149.27	0.17	0.20	0.46	0.18
S21	42.90	122.57	0.14	0.17	0.38	0.15
S22	47.66	136.18	0.15	0.19	0.42	0.16
S23	74.68	213.37	0.24	0.30	0.66	0.26
S24	89.97	257.05	0.14	0.32	0.80	0.31
S25	74.67	213.37	0.23	0.25	0.66	0.26
S26	82.76	236.62	0.26	0.28	0.74	0.28
S27	98.22	280.64	0.31	0.32	0.27	0.34
S28	105.34	300.99	0.33	0.36	0.93	0.36
S29	117.22	334.93	0.37	0.40	1.04	0.41
S30	94.65	270.43	0.30	0.32	0.84	0.33
MIN	42.90	122.57	0.14	0.16	0.27	0.15
MAX	117.22	334.93	0.37	0.40	1.04	0.41
MEAN	74.40	212.59	0.22	0.26	0.63	0.25

Table 3: Comparison of specific activity and risk indicators with other countries of the world.

Country	Specific Activity			Radiological Index			Reference
	Ra-226	Th-232	K-40	Ra_{eq}	I_γ	H_{ex}	
Nigeria	18.00	22.00	210.00	65.63	0.21	0.18	(Agbalagba and Onoja, 2011)
Najaf	5.50	9.05	332.92	44.08	0.13	0.09	(Hussain and Alzhraa, 2017)
Nigeria(Ogun)	25.49	64.89	181.38	134.97	0.07	0.36	(Adewoyin et al., 2022)
Iraq	58.80	42.38	1025.35	198.37	0.73	0.53	(Hasan and Majeed, 2013)
Turkey	85.75	51.08	771.57	85.75	1.60	0.59	(Dizman et al., 2016)
Saudi	23.2	7.73	278.00	23.19	0.45	0.15	(Alshahri and El-Taher, 2019)
Pakistan	69.50	123.68	453.60	281.27	0.14	0.75	(Khan et al., 2020)
India	36.12	50.45	315.35	130.33	0.48	0.36	(Suresh et al., 2020)
Congo	25.14	18.16	46.15	64.70	0.44	0.17	(Diahou et al., 2022)
China	38.00	57.60	838.00	184.89	0.62	0.50	(Ziqiang et al., 1988)
Egypt	12.88	12.33	445.33	66.36	0.24	0.04	(El-Araby et al., 2021)
Malaysia	37.00	53.00	293.00	135.35	0.43	0.37	(Alzubaidi et al., 2016)
Iran (Sareband)	37.27	43.18	604.05	148.91	0.49	0.39	(Pourimani et al., 2017)
Iran (Shazand)	23.99	31.74	461.09	108.08	0.73	0.29	(Mohebian and Pourimani, 2020)
Iran	10.99	35.36	324.20	88.64	0.63	0.22	Present study

dose rate was higher in the southeastern part of the city. The Borujerd is a mountain city where the kind stones are igneous and sedimentary that causing in some regions the radioactivity to increase or decrease. This study showed that, in general, the amount of radiation and the doses absorbed was lower than the global average and do not pose a threat to human health.

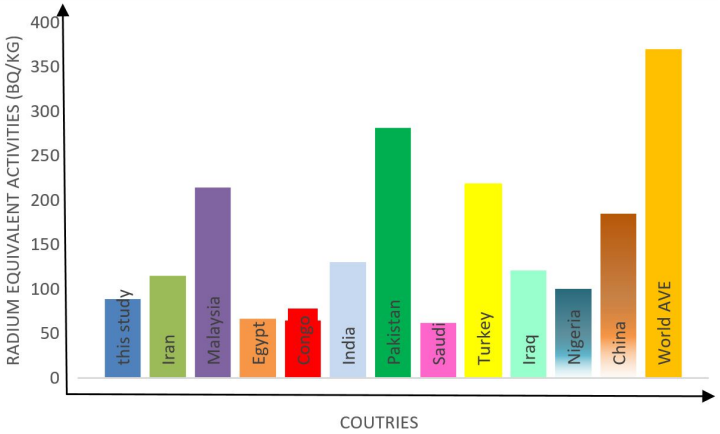

Figure 3: Comparison of the radium equivalent activity value of this study with other countries.

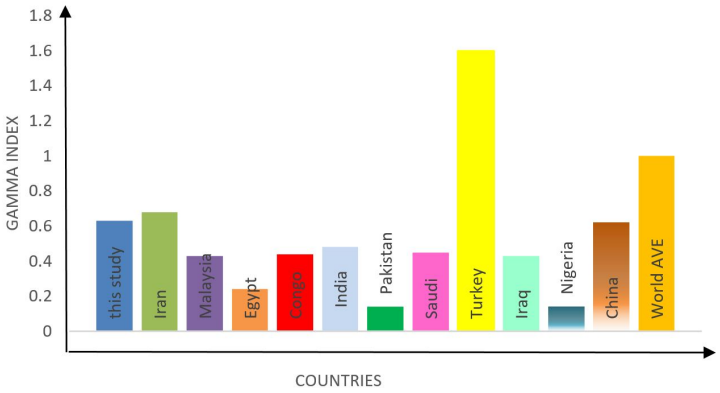

Figure 4: Comparing the gamma index of this study with other countries.

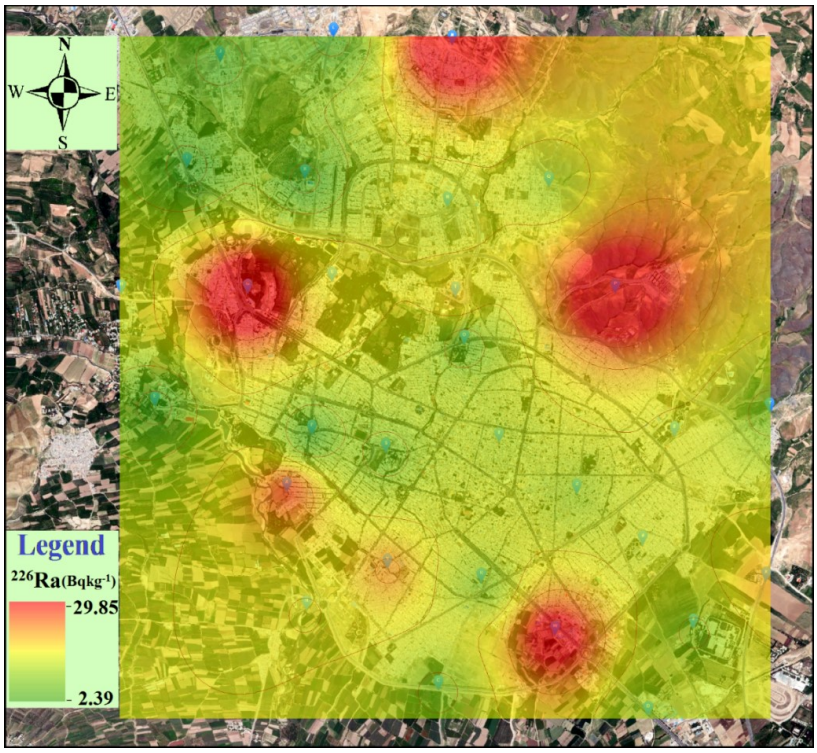

Figure 5: Radium distribution in Borujerd city in Iran.

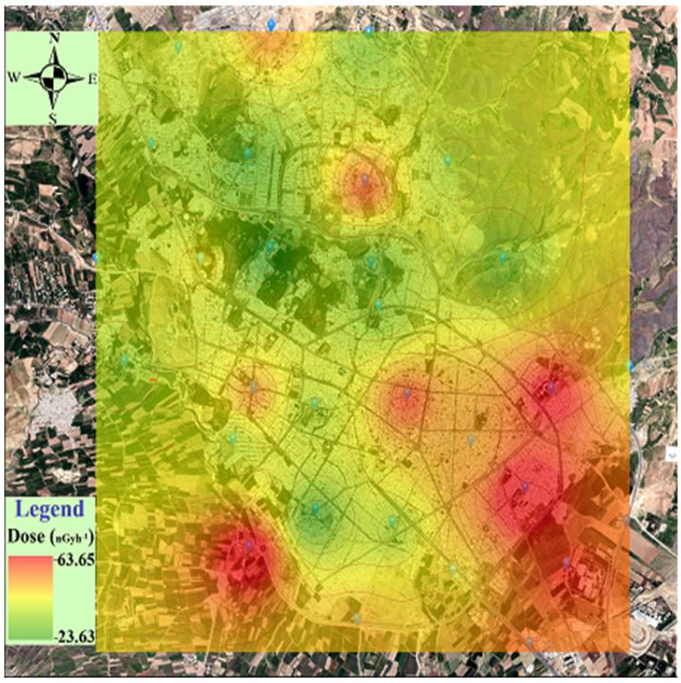

Figure 6: Dose map assignment of Borujerd City in Iran.

4 Conclusions

The study examined the radioactivity of soil samples in the city of Borujerd. The amount of natural radioactive elements was below the global average, and cesium was not detectable in most samples. Radiological parameters of soil samples were calculated and maps of radium distribution and absorbed dose in the air were drawn with the use of GPS software. The quantities of radiological parameters were lower than the global values, and in this sense, the existing nuclear radiation does not pose a threat to the city's inhabitants.

Acknowledgment

This work was funded by the Research Council of Arak University, so the authors of this article are grateful.

Conflict of Interest

The authors declare no potential conflict of interest regarding the publication of this work.

Copyright

References

Adewoyin, O., Maxwell, O., Akinwumi, S., et al. (2022). Estimation of activity concentrations of radionuclides and their hazard indices in coastal plain sand region of Ogun state. *Scientific Reports*, 12(1):1–8.

Agbalagba, E. and Onoja, R. (2011). Evaluation of natural radioactivity in soil, sediment and water samples of Niger Delta (Biseni) flood plain lakes, Nigeria. *Journal of Environmental Radioactivity*, 102(7):667–671.

Alshahri, F. and El-Taher, A. (2019). Investigation of Natural Radioactivity Levels and Evaluation of Radiation Hazards in Residential-Area Soil Near a Ras Tanura efinery, Saudi Arbia. *Polish Journal of Environmental Studies*, 28(1).

Alzubaidi, G., Hamid, F., and Abdul Rahman, I. (2016). Assessment of natural radioactivity levels and radiation hazards in agricultural and virgin soil in the state of Kedah, North of Malaysia. *The Scientific World Journal*, 2016.

Annex, D., on the Effects of Atomic Radiation, U. N. S. C., et al. (2000). Sources and effects of ionizing radiation. *Investigation of I*, 125.

Barnett, C., Belli, M., Beresford, N., et al. (2009). *Quantification of Radionuclide Transfer in Terrestrial and Freshwater Environments for Radiological Assessments. IAEA-TECDOC-1616*. IAEA.

ÇINAR, H. and Altundaş, S. (2015). A Preliminary Indoor Gamma-ray Measurements in Some of the Buildings at Karadeniz Technical University (Trabzon, Turkey) Campus area. *Eastern Anatolian Journal of Science*, 1(1):10–19.

Diahou, R. R. C. M., Bounouira, H., Dallou, G. B., et al. (2022). Environmental radioactivity measurement in soils of an abandoned potash deposit at Holle, Republic of Congo. In *E3S Web of Conferences*, volume 336, page 00030. EDP Sciences.

Dizman, S., Görür, F. K., and Keser, R. (2016). Determination of radioactivity levels of soil samples and the excess of lifetime cancer risk in Rize province, Turkey. *International Journal of Radiation Research*, 14(3):237.

El-Araby, E., Shabaan, D., and Yousef, Z. (2021). Evaluation of radon concentration and natural radioactivity exposure from the soil of Wadi Hodein region, Egypt. *International Journal of Radiation Research*, 19(3):719–727.

Hasan, A. K. and Majeed, H. N. (2013). Natural radioactivity measurement in soil samples from the new Kufa University location, Iraq. *Journal: Journal of Advances in Physics*, 3(2).

Hossain, M. K., Hossain, S. M., Azim, R., et al. (2010). Assessment of radiological contamination of soils due to ship-breaking using HPGe digital gamma-ray spectrometry system. *Journal of Environmental Protection*, 1(1):10.

Hussain, H. H. and Alzhraa, W. S. A. (2017). Natural radioactivity levels of agricultural and virgin clay soil samples at al Najaf governorate. *American Journal of Research*, pages 3–15.

Jibiri, N. and Esen, N. (2011). Radionuclide contents and radiological risk to the population due to raw minerals and soil samples from the mining sites of quality ceramic and pottery industries in Akwa Ibom, Nigeria. *Radioprotection*, 46(1):75–87.

Kabir, K., Islam, S., and Rahman, M. (2009). Distribution of radionuclides in surface soil and bottom sediment in the district of Jessore, Bangladesh and evaluation of radiation hazard. *Journal of Bangladesh Academy of Sciences*, 33(1):117–130.

Khan, I., Qin, Z., Xie, T., et al. (2020). Evaluation of health hazards from radionuclides in soil and rocks of North Waziristan, Pakistan. *International Journal of Radiation Research*, 18(2):243–253.

Mohebian, M. and Pourimani, R. (2019). Measurement of radioactivity levels and health risks in the surrounding soil of shazand refinery complex in Arak, Iran, using gamma-ray spectrometry method. *Iranian Journal of Medical Physics*, 16(3):210–216.

Mohebian, M. and Pourimani, R. (2020). Radiometric properties of virgin and cultivated soil around the Shazand Refinery Complex in Iran. *International Journal of Radiation Research*, 18(4):723–732.

Pourimani, R. and Davood Maghami, T. (2020). Measurement of Radioactivity of Surface Soil in the East of Shazand Power Plant. *Journal of Environmental Science and Technology*, 22(4):109–119.

Pourimani, R. and Mohebian, M. (2021). Study of Background Correction of Gamma-Ray Spectrometry Using Reference Materials. *Iranian Journal of Science and Technology, Transactions A: Science*, 45(2):733–736.

Pourimani, R., Yousefi, F., et al. (2017). Investigation of natural radioactivity of agricultural and virgin soils in Arak and Saraband cities in Markazi province, Iran. *Journal of Water and Soil*, 31(5).

Ranjbar, H. and Yousefi, A. (2019). Identification and determination sources of uncertainty in measurement of activity in soil matrix. *Journal Modern Research Physics*, 4(1):19–28.

Suresh, S., Rangaswamy, D., Srinivasa, E., et al. (2020). Measurement of radon concentration in drinking water and natural radioactivity in soil and their radiological hazards. *Journal of Radiation Research and Applied Sciences*, 13(1):12–26.

UNSCEAR, U. (2000). Sources and effects of ionizing radiation. *United Nations Scientific Committee on the Effects of Atomic Radiation*.

Ziqiang, P., Yin, Y., and Mingqiang, G. (1988). Natural radiation and radioactivity in China. *Radiation Protection Dosimetry*, 24(1-4):29–38.